Multiferroics In Perovskite and Aurivillius Structured Materials

Jun Cao

A thesis submitted for the degree of Doctor of Philosophy

School of Engineering and Materials Science,

Queen Mary, University of London,

London, UK

January 2019

Declaration

The candidate confirms that the research included within this thesis is my own work or that where it has been carried out in collaboration with, or supported by others. The work of other people is duly acknowledged below and my contribution indicated. This thesis fully complies with the regulations set by the Queen Mary, University of London.

Abstract

Multiferroics (MF) are types of novel materials that possess two- or three- of the so called 'ferroic' properties, including ferroelectricity, ferromagnetism and ferroelasticity, which have recently simulated vast number of research activities. Specifically, the couplings between ferroelectricity and ferromagnetism provide the possibilities to create new generation multifunctional devices such as "electric-write, magnetic-read" high density memory media, electric field tunable targeting therapy, micro-magnetic field detection gyro-sensors, etc. There are two main types of materials to realize the multiferroicity, including multiferroics composites and multiferroics single phase compounds. The multiferroics composites, composed by ferromagnetic and ferroelectric phase, are famous for yielding large magnetoelectric (ME) coupling effects above room temperature. However, the multiferroics composites are restricted for applications because their ME coupling effects are commonly achieved by the interaction between piezoelectricity and magnetostriction. The macroscopical couplings are only effective at low frequency range of electric and magnetic fields (below GHz level) and insensitive for low external magnetic fields, which restricts their applications. For the single phase room temperature multiferroics materials, they possibly possess intrinsic ME coupling effects that the magnetic and electric interact mutually through the changes of electron spin. That means the single phase multiferroics are possible to build intrinsic multiferroics for the high speed read/write memory media and low magnetic field detector devices. This study l mainly focus on the preparation, characterization and study on the Aurivillius and perovskite structure based single phase ferroelectric and multiferroics ceramics. The materials in this work were built based on the recent interesting ferroelectric systems including $Ba_2Bi_4Ti_5O_{18}$, $Na_{0.5}Bi_{0.5}TiO_3$ and $x(0.94Bi_{0.5}Na_{0.5}TiO_3\text{-}0.06BaTiO_3)\text{-}(1\text{-}x)BiFeO_3$.

Characterizations on crystal structures, ferroelectric domain structures, dielectric and ferroelectric properties and magnetic properties are intensively investigated and discussed for each composition.

For textured $Ba_2Bi_4Ti_5O_{18}$ ceramics, their dielectric relaxation behaviour has been proved by the diffusion behaviour of dielectric permittivity peaks around T_m (dielectric maxima). Additionally, the other fascinating finding is the electric field induced phase transition behaviour between strong polar-nano-regions (PNRs) to weak PNRs , which is manifested by the current-electric field loops with four peaks on the in-plane and out-of-plane measurement directions.

For $Na_{0.5}Bi_{0.5}Ti_{0.8}Mn_{0.2}O_3$ with Nb additive ceramics, its single phase ceramic has been successfully prepared. In terms of it magnetic nature, the low temperature (< 30 K) remnant magnetization of the *M-H* loops, the zero-field cooling and field cooling (ZFC-FC) results indicate that the ceramic of $Na_{0.5}Bi_{0.5}Ti_{0.8}Mn_{0.2}O_3$ with Nb additive possesses the low temperature ferromagnetic nature. The suggested T_c for ferromagnetic-paramagnetic phase transition is around 50 K. The research of room-temperature multiferrocity on this single phase ceramic reveals that the BNT based multiferroic is a valuable research direction for the new generation of magnetic-electric coupling devices.

For $0.5(0.94Bi_{0.5}Na_{0.5}TiO_3\text{-}0.06BaTiO_3)\text{-}0.5BiFe_{0.8}Mn_{0.2}O_3$ ceramics, the single phase ceramic was successfully prepared. The visible magnetic field tuneable ferroelectric domain switching behaviour under PFM observation present its room temperature magneto-electric coupling effect, which is rarely presented among multiferroics researches. Moreover, the room-temperature ferromagnetism was also strongly confirmed by the apparent remnant magnetization in *M-H* loops, along with the ZFC-FC results, which indicates that $0.5(0.94Bi_{0.5}Na_{0.5}TiO_3\text{-}0.06BaTiO_3)\text{-}0.5BiFe_{0.8}Mn_{0.2}O_3$ possesses the structure with the transition from low temperature ferrimagnetic to room temperature ferromagnetic nature. These encouraged magnetic properties make this composition worthy to be further investigated on its magnetoelectric (ME) coupling effect mechanism or even its high frequencies (THz) ME coupling effect.

Acknowledgement

First of all, please allow me to thank my respected supervisor Dr. Haixue Yan for his profound knowledge and patient guidance during my PhD career. During this period, no matter what problems happened on me, he always supported me to do the choice I tended. And I think I have quitted my PhD project already what if without his continuous help. Also, I would like to thank to Prof. Mike John Reece who is my secondary supervisor. He provides the professional and harmonious experimental environment for all staffs in Nanoforce.

I would also like to thank Dr. Zheng Li, Dr. Vladimir Koval and Dr. Amit Mahajan for their discussions and help with my experiments and papers.

I am appreciating Dr. Isaac Abrahams, Dr. Rory Wilson and Dr. Hangfeng Zhang for their help with the XRD experiments and XRD Rietveld refinement.

I would like to thank Prof. Chenglong Jia for the guidance of the magnetic properties characterization and guidance.

I would like to thank Mr. Maurizio Leo for his help on professional management on the lab to provide us a systematic and clean lab.

I am also very grateful to the help provided by members of our ceramics group: Dr. Chuying Yu, Dr. Kan Chen, Jiyue Wu, Man Zhang.

Lastly, I would like to thank my parents and my girlfriend Yunyin Lin for their supporting and encourages during my PhD career.

Notation

α_{ij}	Magnetoelectric coupling coefficient
d_{33}	Vertical piezoelectric constant
e	Electron charge
E	Electric field
H	Magnetic field
H	Hamiltonian
H_{DM}	Hamiltonian of Dzyaloshinskii–Moriya
I	Current
J	Total angular momentum
J_d	Direction exchange integral
k	Boltzmann`s constant
l	Orbital magnetic quantum
M	Magnetization
M_r	Remnant magnetization
P	Polarization
P_l	Orbital angular momentum

P_r	Remnant polarization
P_s	Spontaneous polarization
S	Spin angular momentum
t	Tolerance factor
T_c	Curie point
T_f	Freezing temperature
T_N	Neel temperature
T_0	Equivalent temperature of activation energy
μ_B	Bohr magneton
μ_{ij}	Relative permeability
μ_l	Orbital magnetic moment
μ_s	Spin angular momentum
μ_0	Vacuum permeability
V	Volume of the unit cell
ω_0	Attempt angular frequency of the dipoles
χ_m	Magnetic susceptibility
γ	Gyromagnetic ratio of angular momentum

Δx_i	Atomic displacement
δ_s	Spin angular moment
δ_s	Spin angular moment
ħ	Planck constant
Φ	Magnetic flux
ε_{ij}	Relative permittivity

Abbreviations

AC	Alternating current
AFM	Antiferromagnetic
B2BT	$Ba_2Bi_4Ti_5O_{18}$
$BF_{(1-x)}M_xO$	$BiFe_{(1-x)}Mn_xO3$
BFO	$BiFeO_3$
BLSFs	Bismuth layered structure ferroelectric
BNT	$Na_{0.5}Bi_{0.5}TiO_3$
BNT8M2	$Na_{0.5}Bi_{0.5}Ti_{0.8}Mn_{0.2}O_3$
BTO	$BaTiO_3$
CFO	$CoFeO_2O_4$
DC	Direct current
EMN	Equivalent magntic noise
FE	Ferroelectric
FeRAM	Ferroelectric random access memory
FM	Ferromagnetic
GMR	Giant magnetoresistive

HOMEC	Healthy ovarian cell
ME	Magnetoelectric
MENs	Magnetoelectric nanoparticles
M-H loops	Magnetic field dependence magnetization
MRAM	Magnetic random access memory
NBTB	$(1\text{-}x)Na_{0.5}Bi_{0.5}TiO_3$ - $xBaTiO_3$
PFM	Piezo force microscope
P-I-E	Polarization-current-electric field
PMNT	$Pb(Mg_{1/3}Nb_{2/3})O3\text{-}PbTiO_3$
PNRs	Polar nano-regions
Ps	Spontaneouse polarization
PVDF	Polyvinylidene fluoride
SEM	Scanning electron microscope
SKOV-3	Human ovarian carcinoma cells
SPS	Spark plasma sintering
SQUID	Superconducting quantum interference device
Terfenol-D	$Tb_{0.27\text{-}0.3}Dy_{0.73\text{-}0.7}Fe_{1.9\text{-}1.95}$

XRD	X-ray diffraction
ZFC-FC	Zero-field cooling and field cooling

Table of Contents

List of Figures

List of Tables

Chapter I Introduction

The ferroelectric by using two spontaneous polarisation “up” and “down” to record the binary code “0” and “1” was firstly proposed by J.R. Anderson who worked in Bell labs at 1952.[1] The ferroelectric random access memory (FeRAM) with fast-read and non-volatile characters is designated based on this principle. Recently, FeRAM has achieved fast access speed (5 ns) and high density (64 MB/unit), but it is limited by the inevitably destructive drawbacks during read and reset operation.[2] By comparison, magnetic random access memory (MRAM) has been lagging far behind. Although Freescale Corporation reported the commercial production of a smaller MRAM for testing in 2006, it is restricted as a read only medium due to the high energy consumption during data writing. A novel medium called “multiferroic” was reported in recent years. These novel materials that simultaneously possess ferroelectricity and ferromagnetism can combine the advantages of FeRAM and MRAM. The memory media that produced by multiferroics possess the advantages of electrical write operation with low-energy consumption, and magnetic read operation without destructive the original data, theoretically.[3] It is thought to be one of the best candidates for the next generation high density and high-speed memory media that require high efficiency read and write for high resolution and high frame frequencies videos, such as Virtual Reality (VR). And it is promising to provide four logic state by tuning polarization (P) and magnetization (M) (four logic state: +P/+M, +P/-M, -P/-M, -P/+M), that has potential to exponentially increase the storage capability, see Figure 1.1. What’s more, it is regarded as a new generation of high sensitive magnetic sensors that has high cost/performance values and more compact size. It means that the explorations on magnetism properties will become more commomly touching for most of research groups.[4]

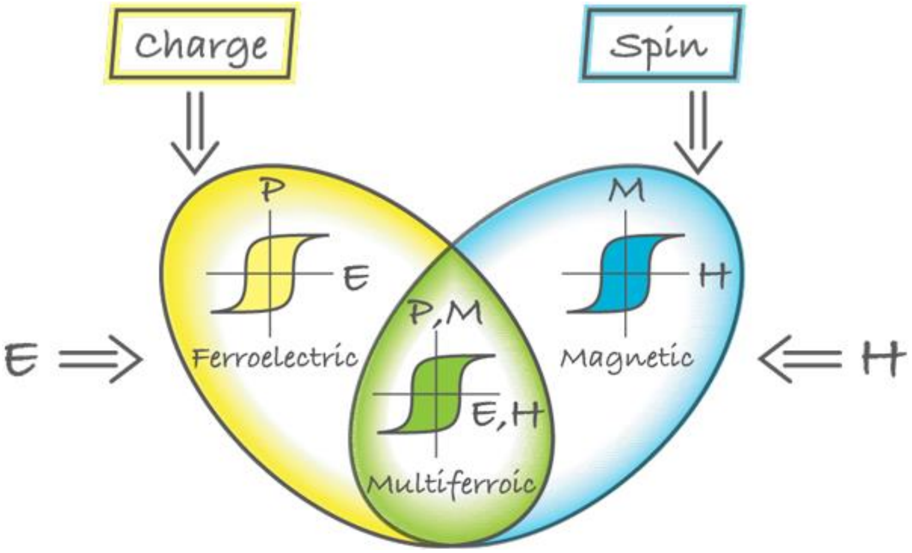

Figure 1.1 Four state logic for multiferroics order. The coupling between electric polarization P and magnetization M realized multiferroicity. (https://physics.aps.org/articles/v2/20)

However, the reality is that there are few room-temperature single phase multiferroics in the nature. Three main reasons result in it, they are (1) the origins exclusion between magnetic and electric (2) high synthesis difficulties (3) remnant magnetization appears at ultra-low temperature (low T_N or T_C). The most vital reason is the exclusion between magnetic and electric origins. For regular ferromagnetic atoms such as Fe, Ni and Co, in order to achieve the net magnetic flux, the transition metal ions commonly require partially electron filled *d* or *f* orbital with unpaired electrons. On the contrary, the ferroelectric ions need d^0 or s^2 state to hybridize with O 2p ions to produce ferroelectricity.[5,6] Therefore, the different requirements between ferroelectricity and ferri/ferromagnetism result in rare multiferroics materials in the nature. Secondly, the single phase multiferroics are very difficult to be synthesised. The impurities that contain magnetic element are extremely tend to form during calcination and sintering procedure. The magnetic impurities would result to the non-intrinsic magneto-electric (ME) coupling, what researchers' appeal is to produce the ME coupling within lattice scale instead of among different phases. What's more, for the existed single phase multiferroics that found till now, most of them present extremely low Curie (T_C) or Neel (T_N) transfer temperature from paramagnetic (PM) to ferro/antiferro-magnetic (FM/AFM), which lead to the remnant magnetization is negligible under room temperature, e.g. $Pb(Fe_{0.5}Nb_{0.5})O_3$ (T_N = 150 K (AFM-PM))[7], $BiMnO_3$ (T_C = 105 K (FM-PM))[8], $YMnO_3$ (T_N = 47 K (AFM-PM))[9]. In our studies, we attempted to produce three different types of ferroelectric based multiferroics, they are:

(1) $Ba_2Bi_4Ti_5O_{18}/Ba_2Bi_4Ti_{(5-x)}Mn_xO_{18}$,

(2)$Na_{0.5}Bi_{0.5}Ti_{(1-x)}Mn_xO_3$

(3)$x(0.94Bi_{0.5}Na_{0.5}TiO_3\text{-}0.06BaTiO_3)\text{-}(1-x)BiFe_{(1-y)}Mn_yO_3$.

The initial inspiration is by doping the Aurivillius structure with magnetic element. Haixue etal., reported three layers Aurivillius structure with La, Nb, Co and Fe element doping, the achieved composition is $Bi_{3.25}La_{0.75}Ti_{2.5}Nb_{0.25}(Fe_{0.5}Co_{0.5})_{0.25}O_{12}$ (BFCT). BFCT presents very rare visible room temperature ME coupling effect under piezoforce microscope (PFM) inspection. This could be ascribed to the tilt of TiO_6 octahedral contributes to the ferroelectricty. Therefore, the magnetic element substitution on Ti site would theoretically generate the interaction between ferroelectric and magnetic state.[10] On this basis, we selected the five layered Aurivillius structure of $Ba_2Bi_4Ti_5O_{18}$ which theoretically occupies the better ferroelectric properties as the component for further doping. We eventually built the pure $Ba_2Bi_4Ti_5O_{18}$ (B2BT) but fail on substitute the Ti with Mn element. Therefore the detailed characterizations were carried on its structure, ferroelectricity and dielectricity. We found a very interesting electric-field induced phase transition behaviour on B2BT, see Chapter 4.

Moreover, due to the outstanding ferroelectric properties of $Bi_{0.5}Na_{0.5}TiO_3$ (BNT), BNT was selected as the basic component for synthesis the other type of novel multiferroics. We successfully substituted Ti with Mn element, and the achieved single phase compostion with maximum doping ratio is $Bi_{0.5}Na_{0.5}Ti_{0.8}Mn_{0.2}O_3$ (BNMT). The impurities appear when Mn doping ratio beyond this critical point. The very detailed characterizations and analysis including structure, ferroelectric, dielectric and magnetic properties were all carried on BNMT. The most valuable result is that it has the low-temperature ferromagnetic nature, which is never reported before.

Among the known multiferroics, $BiFeO_3$ (BFO) is the most famous room-temperature multiferroics without doping found since now that simultaneously possesses critical transfer temperature from paraelelctric to ferroelectric (T_C) at 1100 K and paramagnetic to antiferromagnetic (T_N) = 645 K. In our studies, BFO is the very important component in producing multiferroics. We have successfully prepared a novel composition of $0.5(0.94Bi_{0.5}Na_{0.5}TiO_3\text{-}0.06BaTiO_3)\text{-}0.5BiFe_{0.8}Mn_{0.2}O_3$ (NBTB-BF8M2O) which has never been reported before. It has a very rare magnetic nature that combine with both low-temperature (<50 K) ferromagneticity and room-temperature ferrimagneticity.

Chapter II Literature Review

2.1 Background of Ferroelectrics

Ferroelectric ceramics were initially born in the early 1940s with the ferroelectricity as the high dielectric constant materials in ceramic barium titanate capacitors. Since then, they act as the main role from manufacturing high-dielectric-constant capacitors and transducers.[11] The research of ferroelectricity mainly focus on its spontaneous polarization (P_S). P_S is a vector that commonly originates from the central anion and cation displacement in polar structures. Only 10-point groups exhibit polar nature within all 32 crystal point groups. This non-symmetry nature is the basic requirements for generating ferroelectricity and piezoelectricity.

Since ferroelectrics gathered numerous of attention, its family enlarged rapidly recent years. The main families are: oxygen octahedral contained ferroelectrics ($BaTiO_3$), $LiNbO_3$ related ferroelectrics, hydrogen bond contained ferroelectrics (KH_2PO_4) and Aurivillius phase layer structure group ($Ba_2Bi_4Ti_5O_{18}$) or some other high-dielectric but lead contained ferroelectrics, a typical example is $PbTi_xZr_{1-x}O_3$.[12,13]

In terms of most of ferroelectric and dielectric materials, researches mainly focus on its relative permittivity (ε_r), electrical capacitance (C) and ferroelectric polarization density (P).

The relative permittivity (ε_r) of a dielectric material is often described as the ratio of one capacitor's capacitance that filled with this dielectric material to vacuum. It is a dimensionless quantity. And it could also be expressed as:

$$\varepsilon_r = \frac{\varepsilon}{\varepsilon_0} \tag{2.1}$$

where ε is the absolute permittivity, ε_0 is the vacuum permittivity ≈ 8.854×10^{-12} F/m.

Capacitance (*C*) is the ability of a dielectric material to accumulate charge. It is only related to the permittivity of dielectric materials, the area of the polar plates and the distance between them. The capacitance could be defined as below:

$$C = \frac{\varepsilon_r \varepsilon_0 S}{d} \tag{2.2}$$

where C is the electrical capacitance, ε_r is the relative permittivity, ε_0 is the vacuum permittivity ≈ 8.854×10^{-12} F/m, S is the plate area and d is the distance between the plates. For the common tests for dielectric properties, relative permittivity (ε_r) is generally calculated by substituting the measured capacitance (*C*) value into equation (2.2).

The ferroelectric polarization density (*P*) describes the density of the induced electrical dipole moments for a dielectric medium. In a linear, homogeneous and isotropic dielectric material, the *P* could be expressed as below:

$$P = \varepsilon_0 \chi E \tag{2.3}$$

where ε_0 is the vacuum permittivity, χ is the electrical susceptibility and E is the electrical field.

2.1.1 Ferroelectric domain

Spontaneous polarizations in ferroelectric crystal are not uniformly aligned throughout the whole crystal. The crystal contains many small zones within the spontaneous polarization point to the same direction. These small zones are so called “ferroelectric domains”. The region between two domains called domain wall (see Figure 2.1). The widths of ferroelectric domain walls are usually 1-10nm which are thinner than domain walls in ferromagnetic materials.[14] The walls which separate domains with antiparallel polarization are called 180° walls and the walls that separate regions with mutually perpendicular polarization called 90° walls (see Figure 2.1).

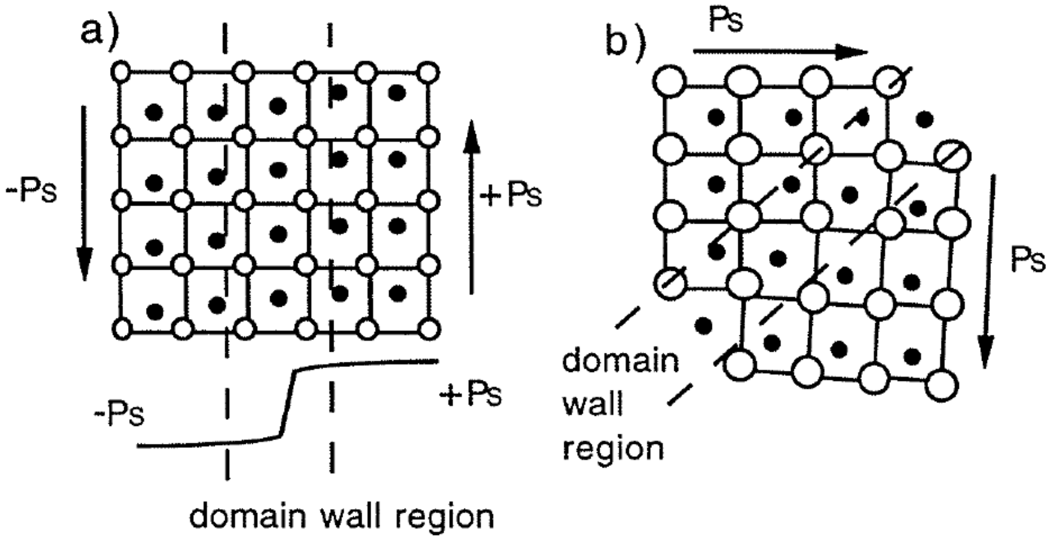

Figure 2.1 Illustration of (a) 180° and (b) 90° ferroelectric domains and domain-wall regions in a tetragonal perovskite ferroelectric.[14]

The ferroelectric domain switching occurs through a process of inhomogeneous nucleation and anisotropic growth of favourably oriented domains.[15] And the domain and domain walls can be clearly observed under piezo force microscopy (PFM), transmission electron microscopy (TEM) or even traditional optical microscopy. The typical ferroelectric domains in $BaTiO_3$ have been studied by Walter J. Merz *et al.* in 1954.[15] They successfully characterized the 90°, 180° and 90°/190° mixture domain walls. The domains walls are distinguished into three types. The first one is the region between one domain in which all the dipoles are aligned normally to the crystal plate (*c* domain) and another domain in which all the dipoles are aligned in the direction parallel to the crystal plate surface (*a* domain), see Figure 2.2. In the first case, the 90° walls between *a* and two *c* domains, the cross section of the domains are shown by Figure 2.2 (a) bottom schematic, the 90° domain wall cross the crystal with an 45° angle to the crystal plate. In the second case, the domain walls are still 90°, but the dipoles are all aligned parallel to the crystal surface, which forms the *a* domains. Other than the first case, these walls all cross the crystal with 90° to the major surface, see Figure 2.2 (b). The third case is the 180° walls, the boundaries between adjacent domains that consists of the antiparallel polarization, see Figure 2.2 (c). Figure 2.2 (d) illustrates the condition of the 90° and 180° domain wall mixture. The boundaries that align 45° on the surface is the same with the 90° walls shown by Figure 2.2 (b). In addition, the strain applied on the crystal results in the domain splits up into many domains with antiparallel polarization. They align themselves in a way that no surface charges are built up on the 90° walls with head-to-tail arrangement.[15]

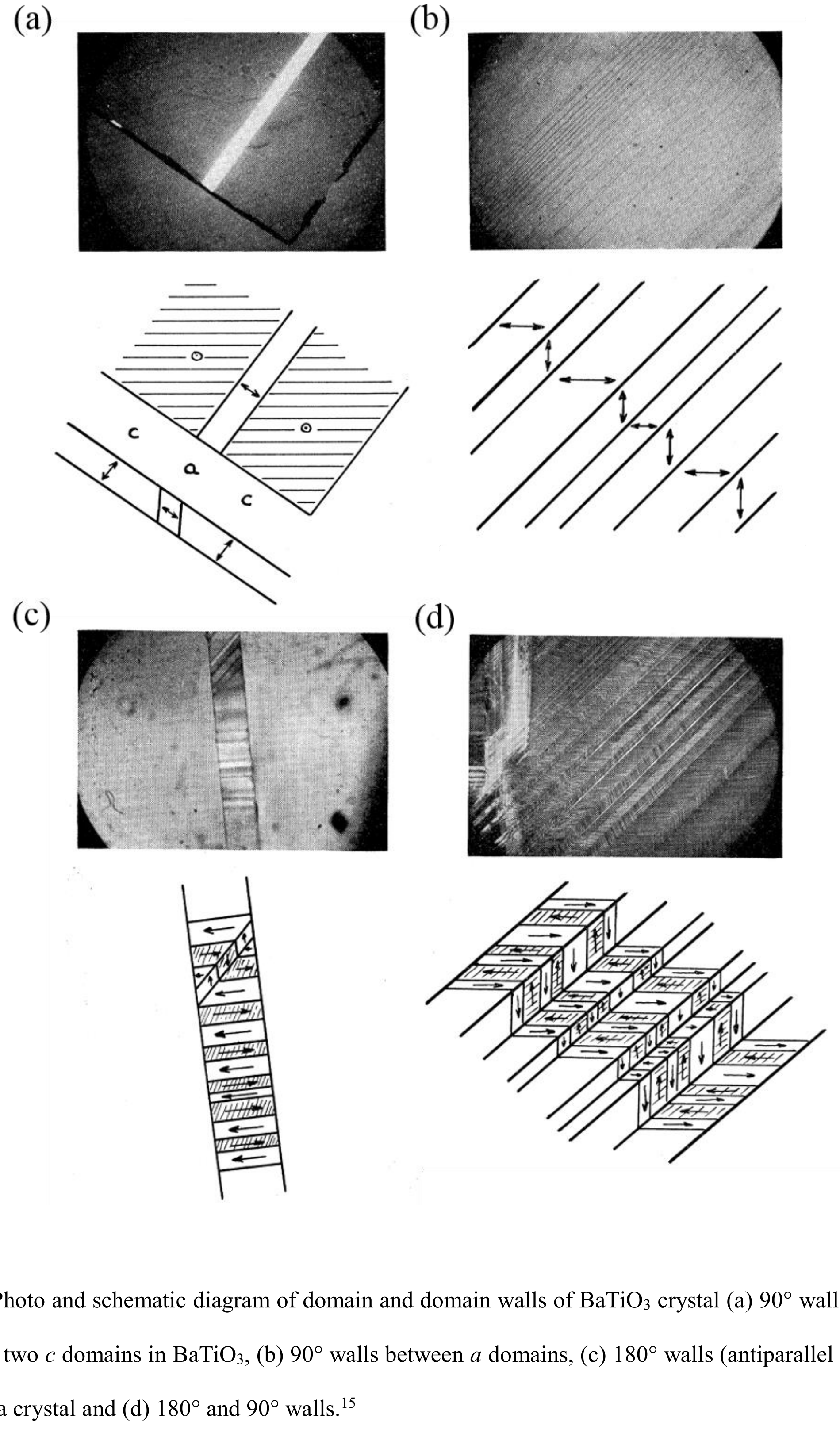

Figure 2.2 Photo and schematic diagram of domain and domain walls of $BaTiO_3$ crystal (a) 90° walls between *a* domain and two *c* domains in $BaTiO_3$, (b) 90° walls between *a* domains, (c) 180° walls (antiparallel domains) at the edge of a crystal and (d) 180° and 90° walls.[15]

In ferroelectrics, the domain wall energy is dominated by the extremely strong coupling between polarization and the strain, and polarization switching thus happens on a much shorter scale of a few unit cells.[16] Figure 2.3 (a)(b)(c)(d) show four different 180° ferroic domain walls structure, which are Ising-, Bloch-, Néel- and the mixture of Ising-Néel type, respectively. The recent reports reveal that the 180° domain wall structure to be predominated by Ising-type but also possess the components of Bloch- and Néel-like character.[17]

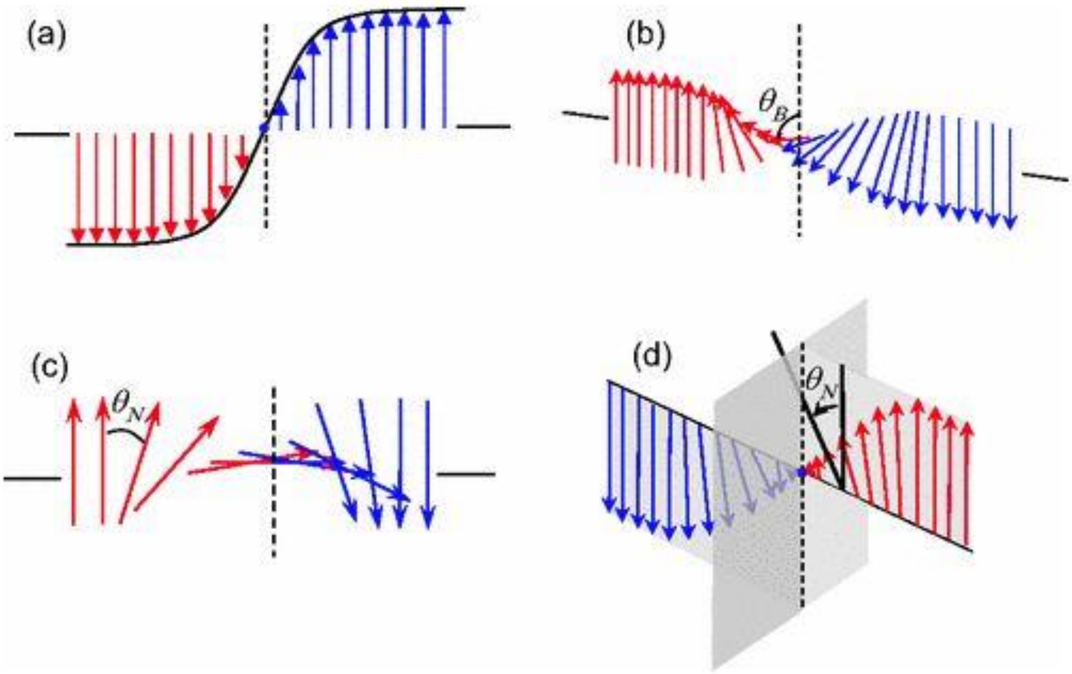

Figure 2.3 Four different models of ferroelectric domain walls. (a) Ising type, presenting an order parameter magnitude variation only condition, which are the predominantly as the structure as the 180° domain wall; (b) Bloch type, showing an out-of-plane polarization rotation without magnitude variation; (c) Néel type, showing order parameter rotate along in-plane direction with magnitude unchanged simultaneously; (d) Mixed Ising- Néel type, showing the in-plane angle rotation with magnitude decrease.[17]

2.1.2 Ferroelectric hysteresis loops and domain switching

The ferroelectricity polarization intensity (*P*) changes with eternal electric field (*E*), see Figure 2.4. In this figure, *E* is relatively small and *P* is dependent on *E* linearly (from A to B). With E getting higher after point B, the linear relationship is destroyed. New domain nucleation and the movement of domain walls become irreversible, and the polarization increase ratio is faster than point A to B. When *E* reaches on the value that relates to point C, most domains align toward the same direction, and polarization becomes saturated. P_s, which is called spontaneous polarization, can be defined as the intercept between the extending of D-C line and *y* axis. When *E* decreases to zero, some domains switch back but the net *P* is still beyond zero and the *P* at $E = 0$ is defined as the remnant polarization P_r.

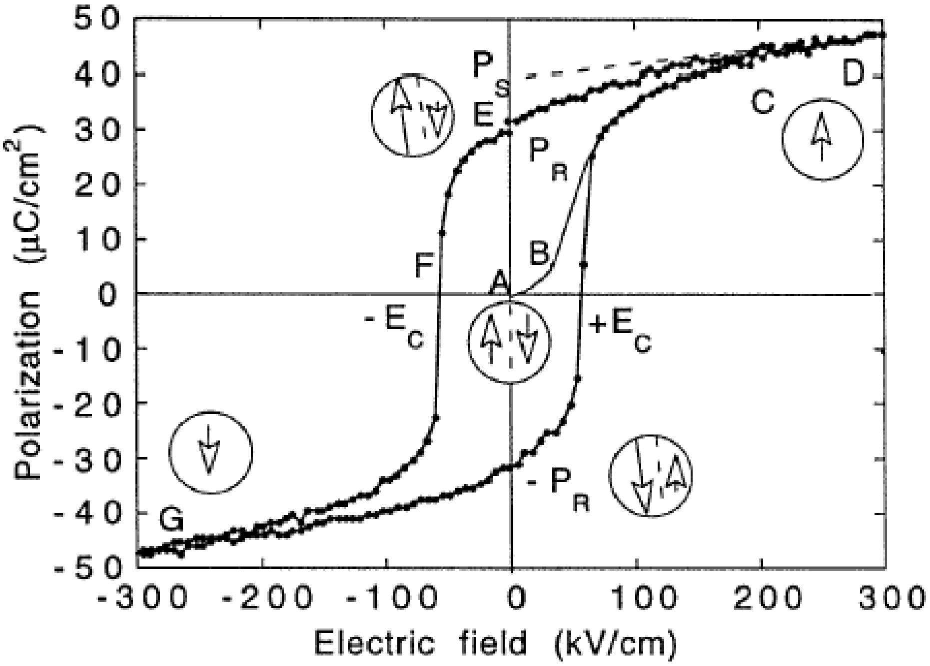

Figure 2.4 Ferroelectric hysteresis loops. Circles with arrows represent the polarization state of the material at the indicated fields.[14]

Then electric field direction reverses and continuously increases. At point F, the quantity of this dual domain direction equals to each other, and *P* is zero at the same time. Point F relates to the value of *E* called coercive field (E_c).

2.1.3 Ferroelectric phase transition

The ferroelectricity in ferroelectrics commonly appears within a certain temperature range. One specific temperature point called Curie point (T_c) is the temperature above which the ferroelectricity will disappear, and the ferroelectrics change to paraelectrics simultaneously. The $BaTiO_3$ phase transition procedure is shown in Figure 2.5. When temperature is under Curie point (401 K), $BaTiO_3$ exhibits ferroelectricity, and P_s is along [001], [011] and [111] in tetragonal, orthorhombic and rhombohedral phase, respectively. When temperature is above 401 K, $BaTiO_3$ transfers to cubic structure. Only the first transition temperature from cubic paraelectric phase to tetragonal ferroelectric phase is called Curie point. At Curie point, properties such as ferroelectricity, dielectricity and ferroelasticity commonly show abnormal behaviours.[18]

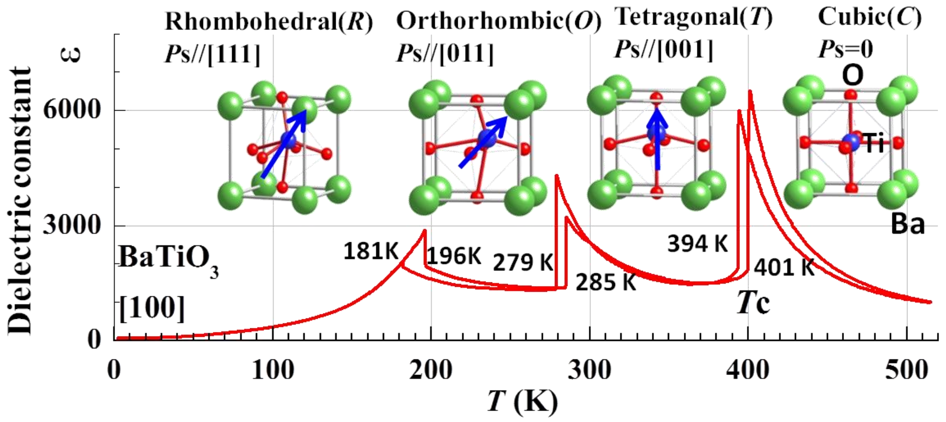

Figure 2.5 Ferroelectric phase transition of $BaTiO_3$ single crystal during heating and cooling.[19]

2.2 Background of magnetism

Regarding to the magnetism basic knowledges, there are two pairs of parameters which are essential to be known, which are magnetization (M) and magnetic susceptibility (χ).

The magnetization (M) describes the magnetized intensity of a material. It is defined as the net magnetic dipole moment per unit volume of that region. The magnetization also describes the respond of a material under outside magnetic field. Regarding to the response in different materials, the magnetic susceptibility (χ) is introduced to indicate whether a material is attracted or repelled by a magnetic field. The relationship between magnetization (M) and volume magnetic susceptibility (χ) for diamagnetic and paramagnetic materials is shown as below:

$$M = \chi H \tag{2.4}$$

where χ is called the volume magnetic susceptibility and H is the external applied magnetic field. In ferromagnetic materials, the relationship between M and H is not the linear correlation due to the magnetic hysteresis. Figure 2.6 exhibits the magnetic field dependent magnetization curve for diamagnetic, paramagnetic and ferromagnetic materials, respectively. The form of hysteresis is the results from the effect of energy losses on magnetization and demagnetization. These are mainly owing to the energetic interactions between domain walls and defects, and the energy losses during domain rotation to against the anisotropy.

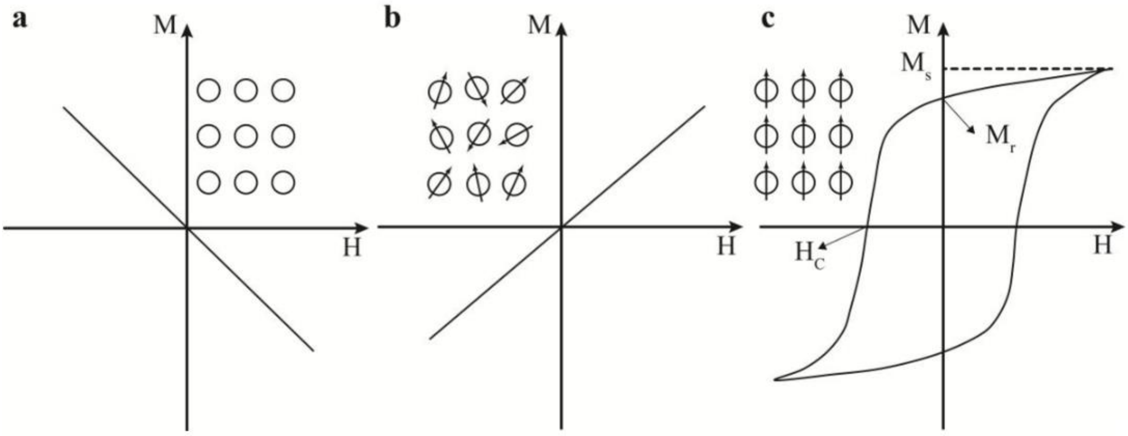

Figure 2.6 Magnetization *vs.* magnetic field hysteresis loops of (a) diamagnetic, (b) paramagnetic and (c) ferromagnetic materials. The circles and arrows represent the different magnetic domain alignment conditions.[20]

To further confirm the magnetic nature of materials, the Curie-Weiss law was introduced, which could be expressed as:[21]

$$\frac{1}{\chi} = \frac{(T-\theta)}{C} \tag{2.5}$$

where χ is the magnetic susceptibility, C is the Curie constant and θ is the paramagnetic Curie temperature. By fitting the linear parts of temperature dependent inverse susceptibility curve with Curie-Weiss law, the intercept between fitting line and x-axis can be used for confirming the magnetic nature. The temperature dependence inverse magnetic susceptibility ($1/\chi$) for paramagnetism, ferromagnetism, antiferromagnetism and ferrimagnetism were shown by Figure 2.7.

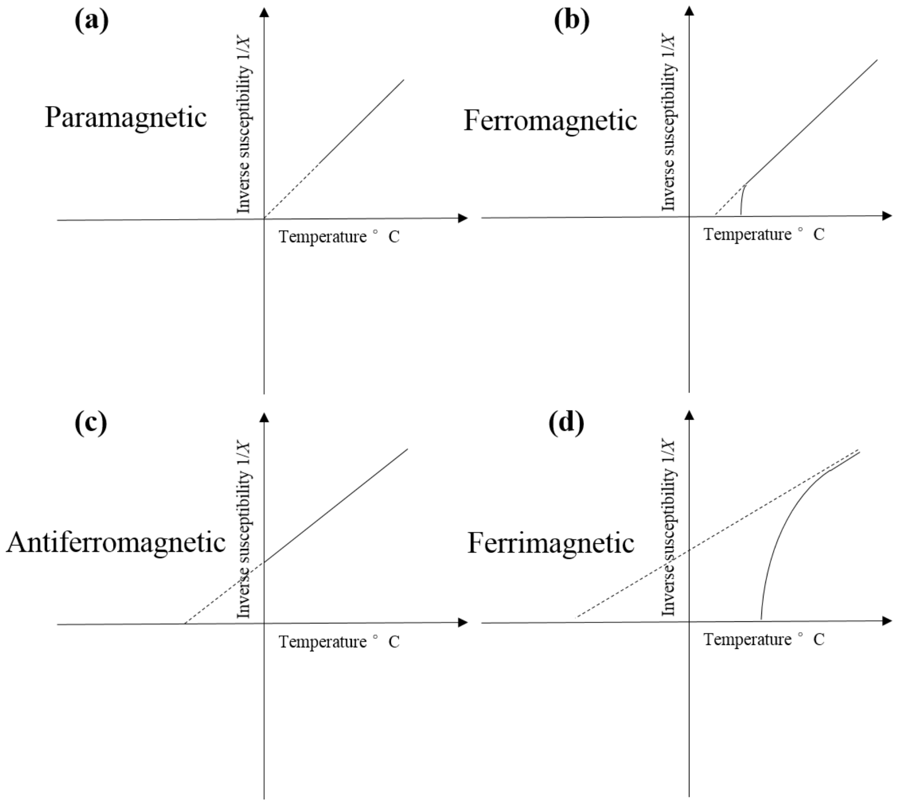

Figure 2.7 The temperature dependence inverse magnetic susceptibility ($1/\chi$) for (a) paramagnetism, (b) ferromagnetism, (c) antiferromagnetism and (d) ferrimagnetism.

For bulk magnetic materials, the magnetic behaviour mainly originates from the individual atomic magnetic moment. And there are two contributions to atomic magnetic moment: electrons spin magnetic moment and orbital moment.[22] Since the Pauli exclusion principle would result in the zero net magnetic moment for paired electrons, the strong magnetic properties always originate from big amount of unpaired electrons.

2.2.1 Electron magnetic moment

Electrons magnetic moment is mainly formed by two parts:

(1) Electrons spin magnetic moment, which is the most subdivided intrinsic magnetic moment. It can be expressed as:[22]

$$m_S = -g_S \mu_B \frac{S}{\hbar} \tag{2.6}$$

where μ_B is Bohr magneton, S is electron spin angular momentum and h is Planck constant. The spin g-factor is approximately:

$$g_S \approx 2.$$

(2) Electrons orbital moment. It is easy to imagine that electrons rotate along orbital equivalent to a circular electric current, which corresponds to orbital moment. The orbital magnetic dipole moment m_L can be described as:[22]

$$m_L = -\mu_B \frac{1}{\hbar} \tag{2.7}$$

where μ_B is the Bohr magneton and h is Planck constant.

2.2.2 Electron orbital alignment

Each full filled electron sub-orbit contains two electrons, and based on Pauli principle, each pair of electrons spins must be antiparallel, which results in zero net electron orbital magnetic moment due to the offset. Therefore, non-full filled electron shell is essential to obtain the non-zero net electron orbital magnetic moment. In terms of high spin state Fe^{3+} ions (Table 2.1), the three lost electrons (marked by red arrow in Table 2.1) in 4s and 3d electron orbits make 3d electrons orbit become the outer shell, and the electron spins in 3d orbit are all parallel to each other, and therefore large net magnetic moment in Fe^{3+} ion can be generated.

Table 2.1 The spin condition of several magnetic elements: Mn, Fe, Co and Ni atoms

Element	**Atomic numbers**	**Inner shell**	**Outer shell electron spins state**	
			3d	**4s**
Mn	25	$1s^2 2s^2 2p^6 3s^2 3p^6$	↑ ↑ ↑ ↑ ↑	↑↓
Fe	26		↑↓ ↑ ↑ ↑ ↑	↑↓
Co	27		↑↓ ↑↓ ↑ ↑ ↑	↑↓
Ni	28		↑↓ ↑↓ ↑↓ ↑ ↑	↑↓

2.2.3 Kinetic exchange interaction

Addition to the magnetic spin moment of each single electrons, kinetic exchange interaction is also the origin of magnetic properties. It usually happens between adjacent ions. Kinetic exchange interaction appears normally when electron-hopping plays the main role in the exchange mechanism. The resulting interaction is commonly antiferromagnetic with electrons spins anti-parallel to each other. There are two main interactions: direct exchange interaction and indirect exchange interaction.[16]

1) Direct exchange interaction

The model of direct exchange is shown in Figure 2.8 (a): the resulting interaction of the spins is preferable to be antiparallel, since the hopping of electrons from original place to neighbouring site suppresses the condition of parallel spins according to Pauli principle, as shown by Figure 2.8 (b).

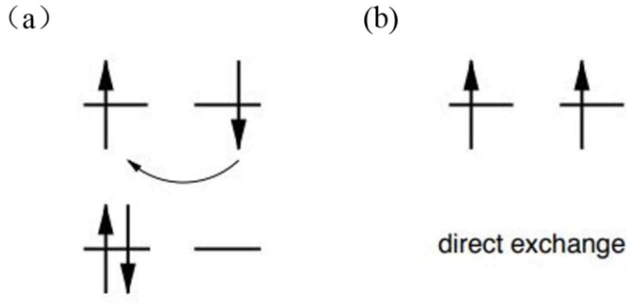

Figure 2.8 The direct exchange interaction model.[16]

2) Indirect exchange interaction

For the transition metal ion contained compounds, since most of the transition-metal are separated by adjacent anion without magnetic moment, the distances between each metal cation are relatively large, which makes the overlap area between each electron cloud very small. The direct interaction is inadequate to explain these configurations. Therefore, super-exchange and double exchange interaction model were mentioned for solving these ferromagnetic order problems.

Superexchange interaction:

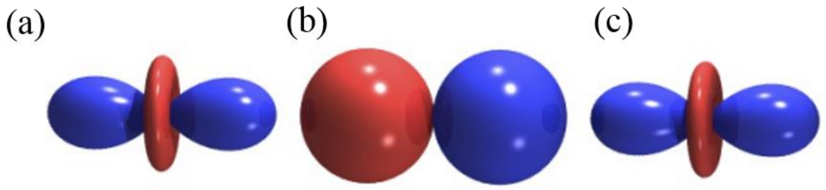

Figure 2.9 In superexchange, an oxygen p-orbital mediates the exchange interaction between two transition-metal d-orbitals. The balls in (b) represent the p-orbital in oxygen anion and the (a)(c) represent d-orbital in transition metal ions.[16]

The regular superexchange interaction normally occurs on the model that cations are separated by anions. The typical superexchange interaction system between two transition-metal cations that separated by oxygen anion bridge is shown in Figure 2.9. The balls in Figure 2.9(b) represent the p-orbital in oxygen anion and the (a)(c) represent d-orbital in transition metal ions. The electron spin exchange conditions are shown in Figure 2.10(a) and (b) For antiparallel spins on the d-orbitals, there are two possibilities for two consecutive hopping processes in this system. The Pauli principle prevents the second hopping process, which restricts the parallel electron spin state in superexchange interaction, shown by Figure 2.10(c).[16]

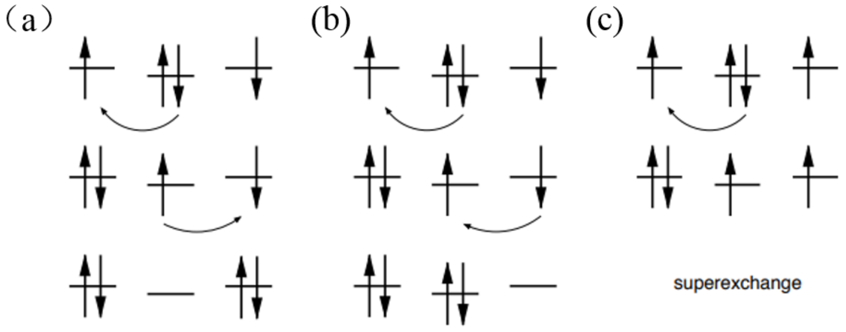

Figure 2.10 (a) and (b) describe two conditions of superexchange interaction model and (c) describes the condition which is non-existent due to Pauli incompatible principle.[16]

2.2.4 Double exchange

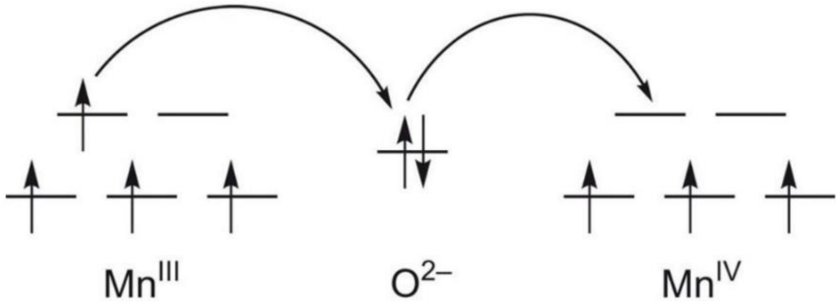

Figure 2.11 Double exchange interaction between Mn^{3+}-O^{2-}-Mn^{4+} system.[23]

The double exchange interaction between Mn^{3+}-O^{2-}-Mn^{4+} system is shown by Figure 2.11. In this system, two electrons hopping happen simultaneously, one hopping from the connecting O^{2-} anion to Mn^{4+} and the other one hopping from Mn^{3+} to O^{2-} anion. The electron from Mn^{3+} substitutes the original electron of O^{2-} anion. The Pauli incompatible principle and Hund's Rules result in parallel electron spins of these two Mn cations, which signifies the generation of ferromagnetism.[23]

2.2.5 Magnetic domain

Similar to ferroelectric domain structures, ferromagnetic domains are areas within which the magnetic dipole moment aligns toward one specific direction. The domain walls are the boundaries between adjacent domains whose the magnetic moments rotate gradually to reduce the total energy in this system. The forms of magnetic domain are mainly correlated to the magnetostatic energy.[24] When a material is only composed of a single domain, there will be a "demagnetising field" around the magnet bulk, shown by Figure 2.12(a). And this demagnetising field would further produce the magnetostatic energy. In order to minimise the magnetostatic energy, the single domain will be divided into several domains gradually, shown by Figure 2.12(b)(c). In order to further reduce the magnetostatic energy to zero, the new magnetic domains that are orthogonal to the original domains would form to produce the closure magnetization which is continuous across the boundary like a flux circuit, and thus no poles are formed in this bulk eventually, shown by Figure 2.12(d)(e),

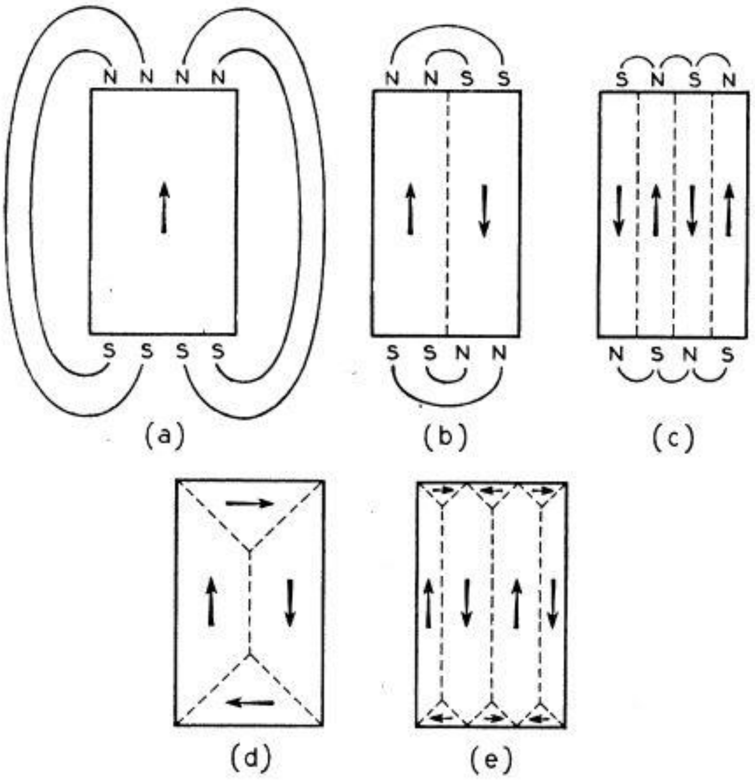

Figure 2.12 The mechanism of magnetic domains form.[24]

2.3 The mechanism and materials for multiferroics

The electric and magnetic are the two consisting parts of multiferroics. A coupling between ferroelectricity and ferromagnetism might give out a novel functionality not just presented in either state alone. The ME coupling in composites and single phase are considerably different, which will be mentioned below. Since the high difficulties of synthesis single phase multiferroics and the ME coupling normally exhibit under extremely low temperature, single phase multiferroics are still far from actual applications in room temperature. Until now, most of the multiferroics devices that close to application are mainly composed by multiferroics composites. However, the ME coupling in multiferroics composites is non-intrinsic, which results in the coupling durability and efficiency far below the theoretical intrinsic coupling. These inevitable drawbacks of multiferroics composites make single phase multiferroics still a worthy research direction. In this section, the mechanism of both single phase and multiferroics composites would be objectively introduced.[25]

2.3.1 The mechanism of single phase multiferroics

1) Displacive ferroelectric based multiferroic. In terms of displacive ferroelectrics, especially for most perovskites structure ferroelectrics, the situation that the ferroelectricity and ferromagnetism simultaneously originating from the same centre atom has been proved to be non-existent. The reason is that ferroelectricity requires body centre transition atoms with d^0 shell, and the d^0 shell orbit could easily hybridize with oxygen atoms 2p orbit at the corners of octahedron. This orbit will further form the ferroelectric polarization long order when ferroelectric centre atoms diverge from centre position. However, the requirement of generating magnetism is half-filled *3d* outer-shell, since the energy of electron ordered spin arises from the exchange effect between adjacent *d* orbit electrons. These two excluded electron orbit states result in the rare multiferroics in nature. This harsh realization triggered the researches for the materials in which the ferroelectric is driven by non-displacive mechanism.

2) Non-displacive ferroelectric based multiferroic. Four main different mechanisms of non-displacive induced ferroelectric are shown in Figure 2.13. For the first three configurations (lone-pair, geometric ferroelectricity and charge ordering), ferromagnetism and ferroelectricity are independent, while in spin-driven mechanism, they emerge jointly.[25,26] Since the atom magnetic moment is normally induced by electron spin, the spin-driven mechanism is mostly possible to generate intrinsic multiferroic.

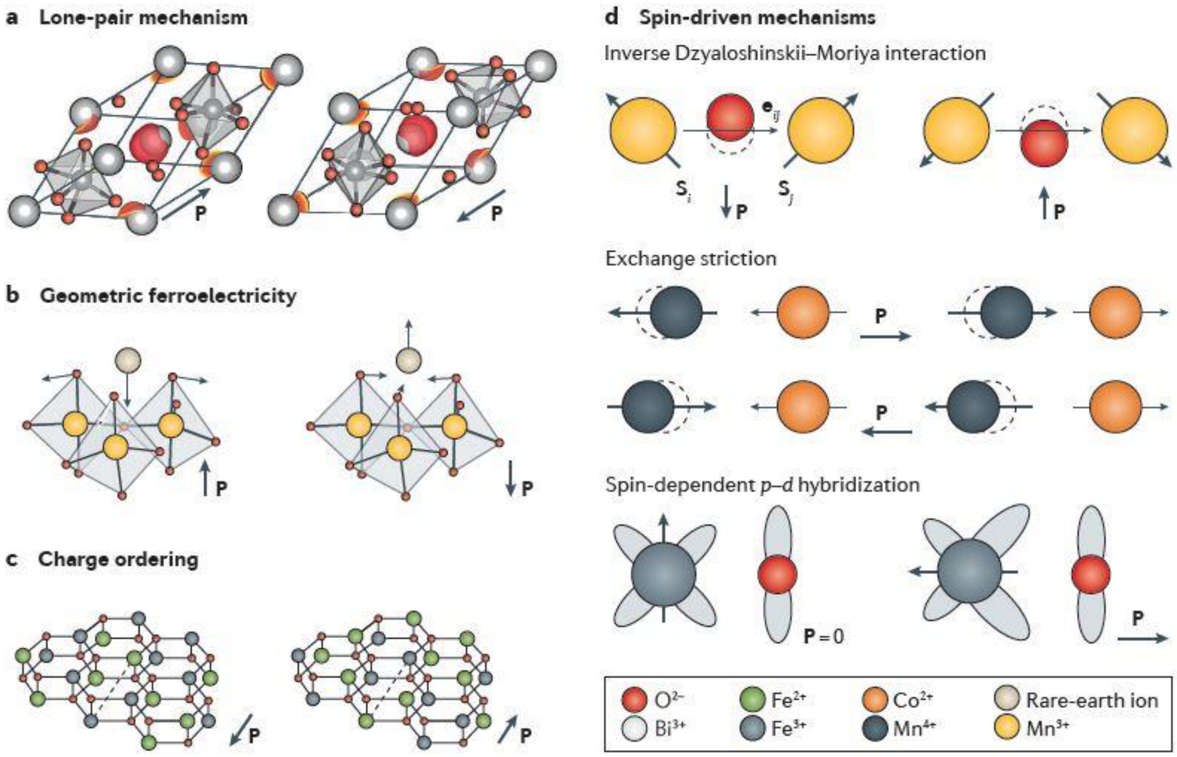

Figure 2.13 Mechanism of three different types of ferroelectricity origins. **a** The lone-pair electron mechanism in $BiFeO_3$, one pair of 6s electrons of Bi^{3+} moving away from Bi^{3+} toward FeO octahedral along [111] direction leads to ferroelectric. **b** Ferroelectricity emerges from the geometrically tilt and deformation of MnO_5 bipyramids in hexagonal (h-)$RMnO_3$ (R = Sc, Y, In or Dy–Lu), which moves the rare-earth ions marked by the arrows and results in a spontaneous polarization along [001] axis. **c** Charge ordering in $LuFe_2O_4$, the spontaneous polarization originates from the two layers, and the polarization parallels to the arrow. **d** Mechanism of spin-induced ferroelectric. On the top panel, for (o)$RMnO_3$ (R = Sc, Y, In or Dy–Lu), the polarization vector is induced by antisymmetric spin exchange interactions. The symmetric spin exchange in Ca_2CoMnO_6 is shown in the middle panel. The bottom panel shows a model of two TM magnetic ions with a ligand (L) oxygen in between with generic electronic configurations.[25,26]

Lone-pair electrons mechanism: The typical lone-pair electrons model that induced multiferroicity is $BiFeO_3$ and $PbVO_3$. In terms of these two compounds, Bi^{3+} and Pb^{2+} play the major role in obtaining the ferroelectricity. For this mechanism, a pair of valence electrons in the 6s orbit that do not participate in the hybridization with p orbit of O^{2-} builds a local dipole to form the spontaneous polarization, and the magnetic moment arise from the B site (Fe^{3+}) perpendicular to the polarization direction.[27]

Geometric ferroelectricity: A typical example is $YMnO_3$. The ferroelectric arises from the buckling of the MnO_5 polyhedra, and there is no re-hybridization chemical bonding changing in phase transition from paraelectric to ferroelectric phases.[28]

Charge ordering: This ferroelectricity arises from the electron correlation, such as $LuFe_2O_4$, and the correlation comes from the Fe^{2+} and Fe^{3+} ions.[29]

Spin-driven mechanisms:

(1) Dzyaloshinskii-Moriya (DM). DM interaction arises from spin-orbit scattering of electrons in an inversion asymmetric crystal field.[30] For the typical DM interaction system of (o)$RMnO_3$ (R = Sc, Y, In or Dy–Lu), the non-centrosymmetric displacement of charges is generated by an acentric spin structure.

(2) Heisenburg-like exchange striction. The Heisenberg-like exchange striction describes an acentric displacement of charges derived from the optimization of the symmetric spin product $S_i \cdot S_j$. For the typical structure of o-$TbMnO_3$, the cycloidal order $S_i \times S_j$ transforms into $S_i \cdot S_j$ when pressure was applied and results an order-of-magnitude increased polarization.[30]

(3) Metal-ligand hybridization. The chemical bond between metal magnetic 3d orbits and anions' 2p orbits generates a spontaneous polarization along the bond direction.[31]

2.3.2 The single phase multiferroics

As mentioned in chapter 2.3, the room temperature single phase multiferroics with good magnetoelectric (ME) coupling are essential candidates for high frequency applications, but there are still few types of materials having attained these requirements. Table 2.2, Table 2.3 and Table 2.4 illustrate parts of the single phase multiferroics that have been reported until now. It is notable that most single phase multiferroics exhibit extremely low magnetism effective temperature and low ME coupling coefficient. The only compound that shows room-temperature multiferroicity is $BiFeO_3$ (BFO). The following section would mainly discuss the properties of BFO and $Bi_{3.25}La_{0.75}Ti_{2.5}Nb_{0.25}(Fe_{0.5}Co_{0.5})_{0.25}O_{12}$ as the example among single phase multiferroics.

Table 2.2 Some typical single phase perovskite oxides multiferroics ceramics

Classification	**Representative Composition**	**Characteristic Temperature**	**Max ME coefficient α** (mV·cm^{-1}·Oe^{-1})
Perovskite oxides	$Pb(Fe_{0.5}Nb_{0.5})O_3$	T_C = 383 K(FE-PE)[32] T_N = 150 K (AFM-PM)[7]	400 (Indirect measurement value, 300K)[33]
	$Pb(Fe_{2/3}W_{1/3})O_3$	T_C = 150 K-200 K(FE-PE) T_{N1} = 20 K (FM-AFM) T_{N2} = 350 K (AFM-PM)[34]	/
	$BiMnO_3$	T_C = 450 K (FE-PE) T_C = 105 K (FM-PM)[8]	/
	$BiFeO_3$	T_C = 1100 K (FE-PE)[35] T_N = 645 K (AFM-PM)[27]	7 (AC H field with 120 Oe DC bias field, 300 K)[36]
	$ErMnO_3$	T_C = 588 K (FE-PE) T_N = 77 K (AFM-PM)[37]	/
	$YbMnO_3$	T_C = 1000 K (FE-PE) T_N = 80 K (AFM-PM)[38]	/
	$YMnO_3$	T_C = 920 K (FE-PE)[39] T_N = 47 K (AFM-PM)[9]	/
	$TbMnO_3$	T_C = 27 K (FE-PE) T_N^{Mn} = 40 K (AFM-PM) T_N^{Tb} = 7 K (AFM-PM)[40]	/
	$LuMnO_3$	T_C = 930 K (FE-PE) T_N = 100 K (AFM-PM)[41]	/
	$(1-x)Pb(Fe_{2/3}W_{1/3})O_3$-$xPbTiO_3$	T_C = 180 K-320 K for x = 0-0.3 (FE-PE) T_{N1} = 360 K, 274 K, 161 K, 134 K for x = 0, 0.1, 0.2, 0.3 (AFM-PM) T_{N2} = 10 K-17 K for x = 0-0.3 (AFM-PM)[42]	/
	$xPbFe_{0.5}Ta_{0.5}O_3$-$(1-x)Pb(Zr_{0.53}Ti_{0.47})O_3$	T_C = 660 K, 530 K, 470 K, 240 K for x = 0, 0.3, 0.4, 1 (FE-PE)	/

Table 2.3 The single phase Non-oxides multiferroics ceramics

Classification	**Representative Composition**	**Characteristic Temperature**	**Max ME coefficient α** ($mV\cdot cm^{-1}\cdot Oe^{-1}$)
Non-Oxides	$LiNiPO_4$	T_N = 20.8 K-21.8 K (AFM-PM)[43]	/
	$Ni_3B_7O_{13}I$	T_C = 60 K (FE-PE) T_N = 61 K (AFM-PM)[44]	/
	$Co_3B_7O_{13}Cl$	Tc = 623 K (PE-FE)[45] T_C = 20 K (FM-PM)[46]	/
	$BaMnF_4$	T_N = 26 K (AFM-PM)[47]	/
	$BaNiF_4$	T_N = 68.4 K (AFM-PM)[48]	/
	$BaFeF_4$	T_N = 54.2 K (AFM-PM)[49]	/
	$ZnCr_2Se_4$	T_N=21 K (AFM-PM) [50]	/
	$CdCr_2S_4$	T_C = 85 K (FM-PM)[51]	/
	$CuFeO_2$	T_{N1} = 14 K, T_{N2} = 11 K (AFM-PM)[52]	/
	$CuCrO_2$	T_N = 24.2 K (AFM-PM)[53]	/

Table 2.4 The single phase Aurivillius multiferroic

Classification	Representative Composition	Characteristic Temperature	Max ME coefficient α (mV·cm^{-1}·Oe^{-1})
Aurivillius Structure	$Bi_{3.25}La_{0.75}Ti_{2.5}Nb_{0.25}(Fe_{0.5}Co_{0.5})_{0.25}O_{12}$	$T_C = 556.5$ K (FE-PE)[10]	0.57 (300 K)[10]
	$Bi_5Ti_3FeO_{15}$	$T_C = 1100$ K (FE-PE)[54] $T_N = 80$ K (FM-PM)[55]	/
	$Bi_6Fe_2Ti_3O_{18}$	$T_C = 960$ K (FE-PE) $T_C = 526$ K (FM-PM)[56]	/

Note: FM = ferromagnetism, AFM = antiferromagnetism, PM = paramagnetism, FE = ferroelectricity, PE = paraferroelectricity.

(1) $BiFeO_3$

$BiFeO_3$ (BFO) is one of the very first found multiferroic, and it is one of the very rare room temperature multiferroics as well. BFO possesses a rhombohedrally distorted perovskite structure. It has high ferroelectric-paraelectric transition temperature T_C at 1103 K,[57] and high antiferromagnetic-paramagnetic transition temperature T_N at 643 K.[58] BFO also has large spontaneous polarization up to 60 μC/cm^2.[59] These outstanding properties make BFO attracted many researches since it has been found.

Crystal structure

The room-temperature phase of BFO is classified as rhombohedral with $R3c$ space group.[60] The lattice parameter is $a_{rh} = 5.6343$ Å and the angel in rhombohedral of about $\alpha_{rh} = 59.348°$ at room temperature with the ferroelectric spontaneous polarization is along

$[111]_{rhombohedral}$.[61,62] The unit cell of BFO can also be presented in a hexagonal with the c-axis of hexagonal parallel to the diagonal of rhombohedral. The lattice parameter of hexagonal are around a_{hex} = 5.58 Å and c_{hex} = 13.90 Å, and BFO can also be presented as pseudocubic unit cell. The structures of $BiFeO_3$ in three presentation are shown in Figure 2.14.[63,64]

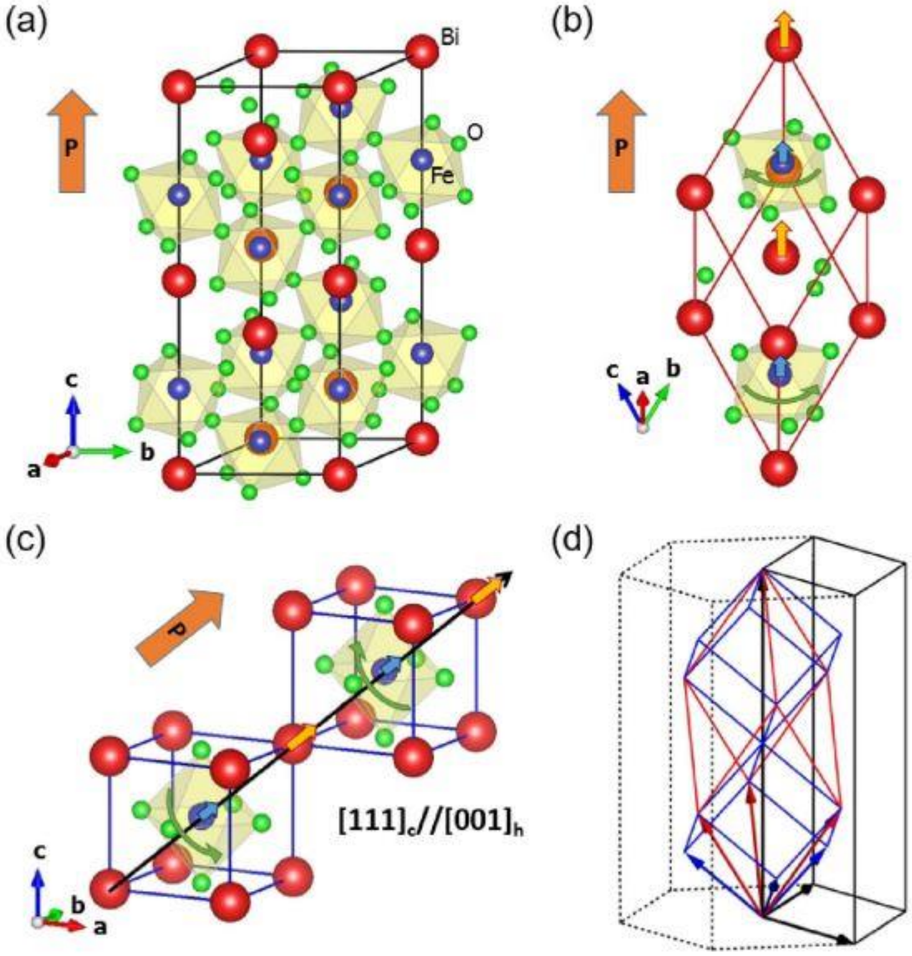

Figure 2.14 $BiFeO_3$ structure under three different representations, red ball: Bi atom, blue ball: Fe atom, green ball: O atom. (a) Schematic view under hexagonal presentation including six formula unit. (b) Schematic view under rhombohedral presentation including two formula units. (c) Schematic view under pseudocubic including one formula unit. The spontaneous polarization along the direction of $[001]_{hexagonal}$ which is identical to $[111]_{rhombohedral}$ and $[111]_{pseudocubic}$. (d) The unit vectors are indicated as black (hexagonal), red (rhombohedral) and blue (pseudocubic) arrows.[64]

The oxygen octahedron in BFO distorts with minimum and maximum O-O distance of 2.710(7) and 3.015(9) Å, respectively, and the octahedron rotates around the $[111]_{\text{rhombohedral}}$ for about $\pm\alpha = 13.8(3)^\circ$.[65] The ferroelectricity of $BiFeO_3$ is induced by the stereochemical activity of Bi^{3+} $6s^2$ lone pair. This $6s^2$ lone-pair electrons is believed to form by the hybridization of 6s and 6p atomic orbitals with 6s electrons filling one of the sp hybridize orbital in Bi atoms, and result in an asymmetric wave function, which will lead to the bonds between Bi and O becoming asymmetric and finally generating electrostatic repulsion resulting in Fe ions displacement.[66] Because of this effect, different Bi-Fe bond lengths along $[111]_{\text{rhombohedral}}$ direction were formed. The lengths are 3.0617(11) Å and 3.8726(11) Å, which are marked as label k and l, respectively (see Figure 2.15). Other Bi-Fe distances are 3.3071(3) Å (label m) and 3.5793(5) Å (label n).[65] The Fe-O-Fe angle is about 154.1°, which is quiet important for determining the magnetic superexchange and the orbital overlap area between Fe and O, and it also relates to the magnetic ordering temperature and the conductivity.[65,67,68]

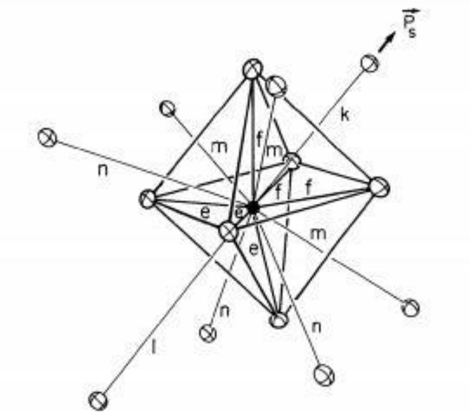

Figure 2.15 One perovskite unit cell in $BiFeO_3$. The thin open circles represent Bi and thick open circles represent O. The filled circle represents Fe, the straight lines all correspond to the chemical bonds between different ions, and the spontaneouse polarization direction is shown as $\overrightarrow{Ps}$.[65]

Ferroelectric and dielectric properties of $BiFeO_3$ bulk

The ferroelectric polarization of bulk $BiFeO_3$ is along the threefold axis of the rhombohedral presentation ($[111]_{\mathrm{rhombohedral}}/[001]_{\mathrm{hexagonal}}$). The P_s measured in early days is about 6 μC/cm^2 in BFO single crystal by Teague *et al.* in 1970s.[69] This value was obtained under a limited saturation condition, and the predictable P_s value would be about 90 μC/cm^2 by ab initio calculations.[70,71] Subsequently, with the crystal grown methods developed, high qualities of $BiFeO_3$ single crystals and films were achieved eventually, with measured P_s at about 60 μC/cm^2. High P_s was also found in $BiFeO_3$ ceramic at about 40 μC/cm^2.[72,59,73-75] The polarization hysteresis loops are shown by Figure 2.16(a)-(c) for the single crystal, thin film and bulk, respectively.

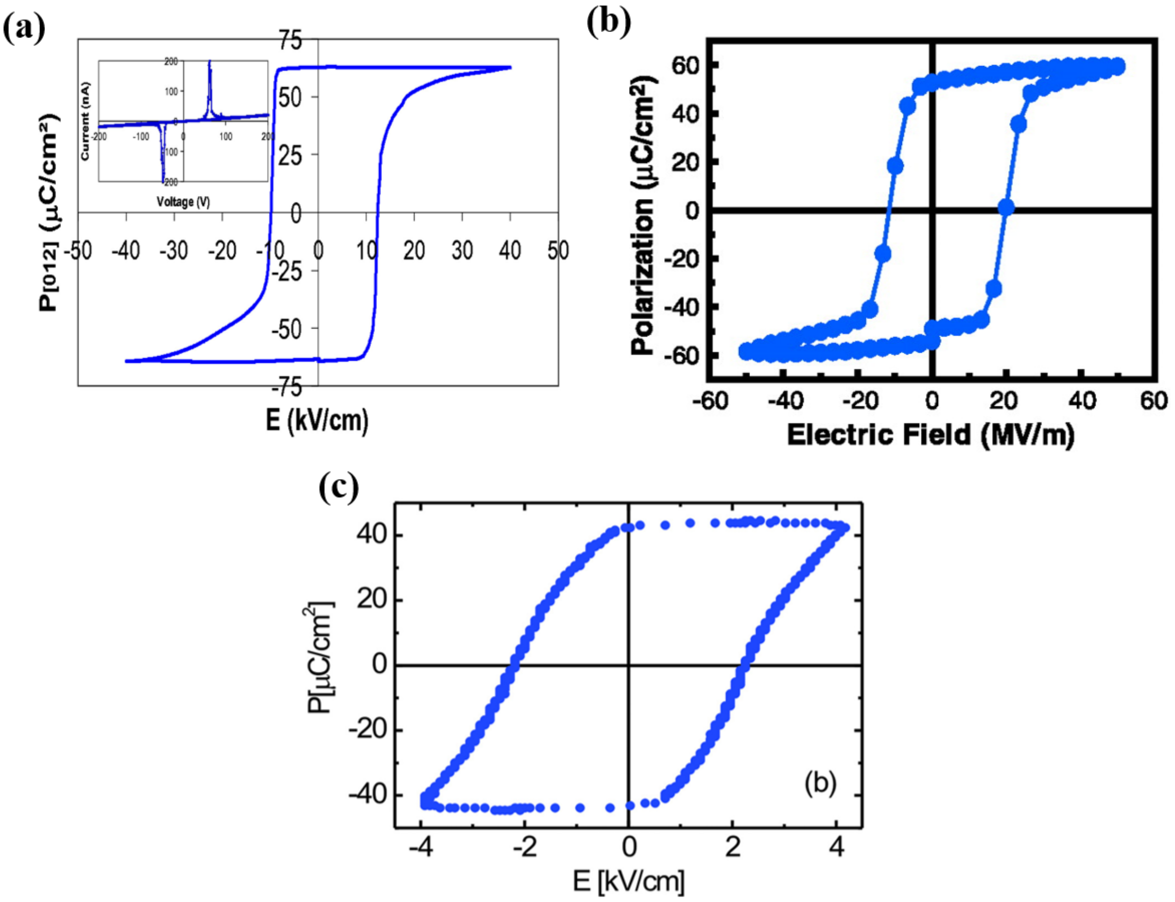

Figure 2.16 The $BiFeO_3$ polarization hysteresis loops *P-E* at room temperature for (a) single crystal, (b) thin film and (c) bulk ceramic.[72,75,76]

The dielectric properties of BFO have been studied for more than fourty years. The temperature and frequency dependent of dielectric tendency on single crystal, thin film and ceramic all have systematic understandings by now. The dielectric properties of BFO can just be normally measured by regular frequency response analyzer under low temperature below to 160 K - 240 K correpsonding to the testing frequencies. This is because the high conductivity and leakage increase dramatically with increasing temperature under this contact mode measurement.

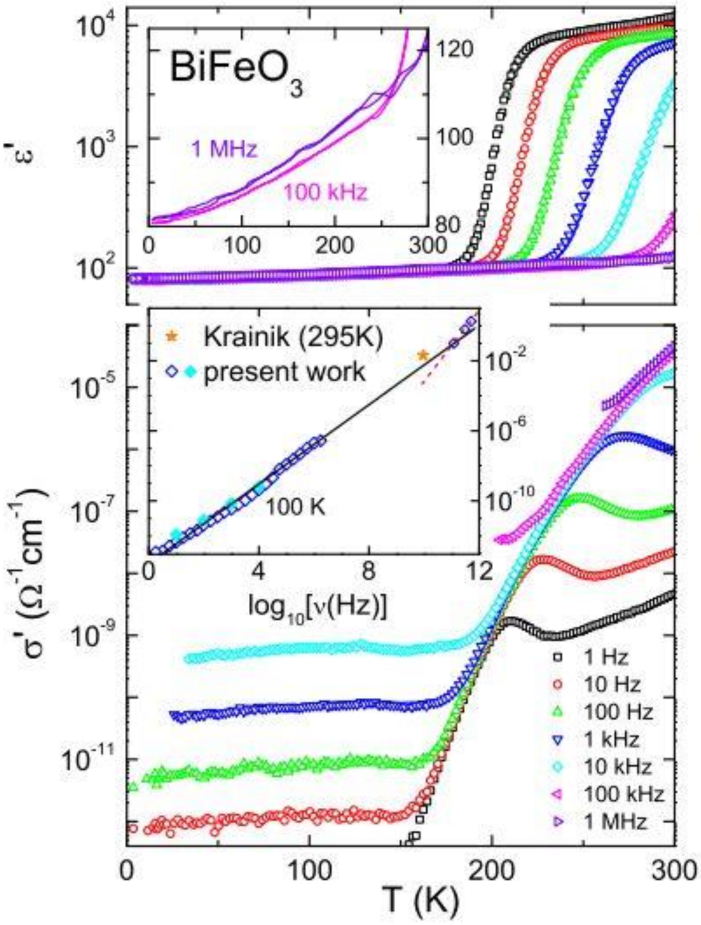

Figure 2.17 $BiFeO_3$ large single crystal dielectric permittivity (upper frame) and conductivity (lower frame) as measured between 1 Hz and 1 MHz for temperatures between 1.5 K and 300 K. The inset in the upper frame indicates the temperature dependence of dielectric permittivity measured at 100 kHz and 1 MHz. The inset in the lower frame indicates the frequency dependence of the ac conductivity at 100 K. Yellow stars represent results under microwave from Krainik[77] and solid and hollow diamonds represent present work.[78]

The dielectric permitivity, AC and DC condictivity of $BiFeO_3$ large single crystal measured by frequency response analyzer are shown in Figure 2.17. It is found that the real part goes up dramatically to 10^4 magnitude when temperature reaches 240 K under 10 kHz testing frequency, which could be explained by the conductivity σ' changing tendency in lower frame in Figure 2.17. The temperature-independent conductivities toward low temperatures mainly correspond to the contribution of ac conductivity due to charge carriers hopping. This behavior can also be further proved by the the frequency dependence of conductivity under low temperature (100K) shown in the inset of lower frame in Figure 2.17. With temperature going higher, the conductivities in lower frame transfer into a frequency-independent tendency, which reveals the intrinsic DC conductivity. These non-intrinsic or intrinsic conductivities contribute to the high values of the measured permitivitty. Furthermore, the millimeter wave spectroscopy was also employed on $BiFeO_3$ dielectric measurement in Ref 83. This non-contact measuring method gives out an intrinsic dielectric permittivity of $BiFeO_3$ at about 53 under 300 K at 120 GHz (4 cm^{-1}), shown in Figure 2.18.

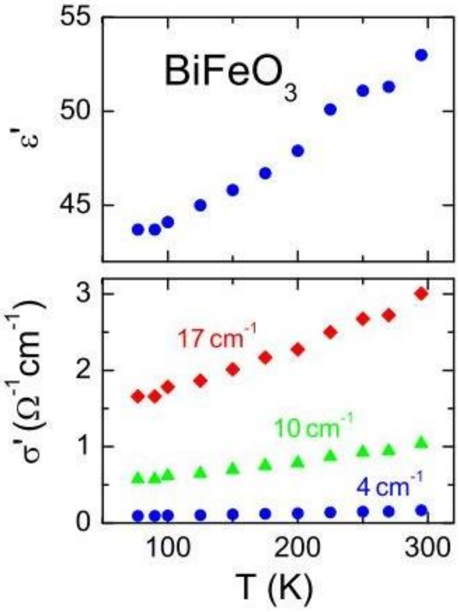

Figure 2.18 The temperature dependence of dielectric permittivity (upper frame) and conductivities on large $BiFeO_3$ single crystal, tested by millemeter-wave spectroscopy.[78,79]

Magnetic properties of $BiFeO_3$ bulk

It is well known that BFO is a very rare room temperature multiferroics with T_N = 370 ºC. The local short-range magnetic ordering of $BiFeO_3$ is G-type antiferromagnetic. In this spin structure, each Fe^{3+} spin is surrounded by six antifparllel spins on the most adjacent Fe ions.[68] The imperfect antiparellel alignment of each pair of spins which is represented by the blue and green lable in Figure 2.19(a), is not completely cancelled mutually and gives out a very weak net magnetic moment. In long-range magnetic ordering, the magnetic spin presented as vector cycloidal propagation pointing to three symmetry-equivalent wave vectors of τ_1 = [1, 0, -1], τ_2 = [1, -1, 0] and τ_3 = [0, -1, 1] with repetition cilcle length at around 640 Å.[80,81] Eventually, the weak net spin moment is completely cancelled by the average out effect of this cycloid and result in the very weak magneticity, shown by Figure 2.19(a). However, magnetic element doping or epitaxial film strain may change the angle within each pair of antiferromagnetic moment or suppress the propagation length to improve the magnetic properties. The BFO has a magnetic easy plane in which the magnetic spin rotates, as represented by the blue and green planes with electron spins in Figure 2.19(b), and the plane is determined by the spin propagation vector and the polarization vector, as shown in Figure 2.19(b).[82,83]

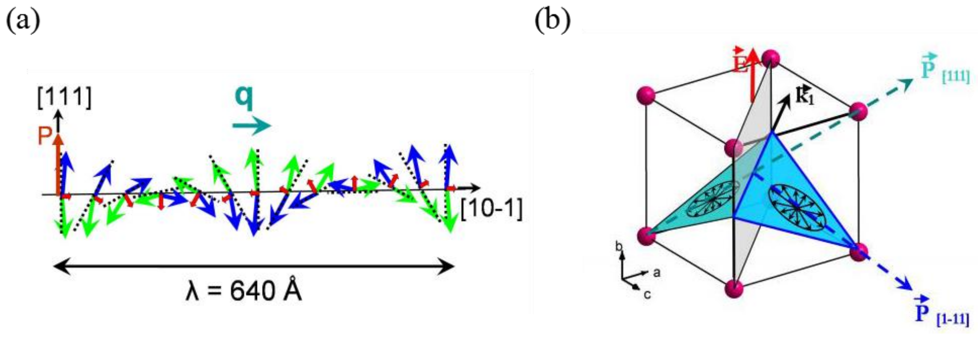

Figure 2.19 (a) The spontaneous polarization direction [111] and magnetic spin propagation direction τ in cubic unit. (b) The spin propagation vector marked by $\overrightarrow{K_1}$ and polarization vector determines the easy magnetic plane (green and blue planes).[82,84]

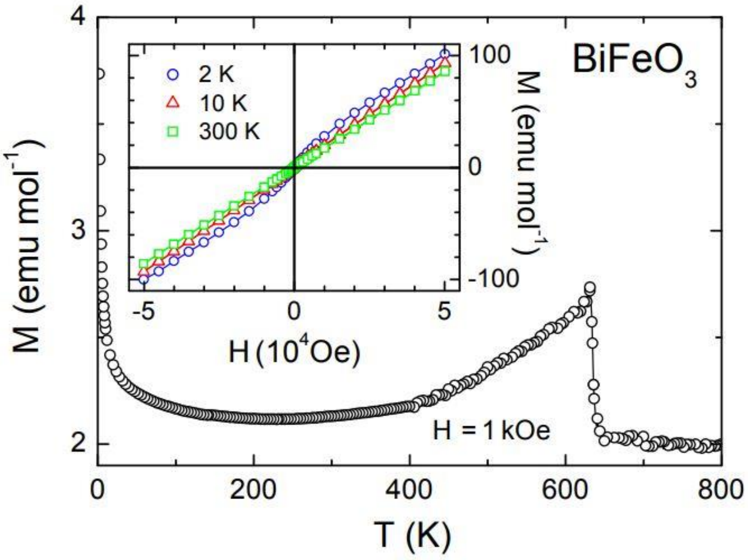

Figure 2.20 Temperature dependence of magnetization of BiFeO$_3$ (large single crystal) measured in external field of 1 kOe between 1.5 K and 800 K. The T_N is estimated close to the anomalies around 635 K. The inset shows magnetization versus external field under 2 K, 10 K and 300 K.[79]

Figure 2.20 shows the typical temperature dependence magnetization of BFO large single crystal from 1.5 K to 800 K. An apparent anomaly appears at around 640 K, which could be attributed to the T_N for BFO. The inset shows the linear correlation between magnetic field and magnetization at 2 K, 10 K and 300 K, respectively. It indicates that the BiFeO$_3$ is the antiferromagnetic order.

Magnetoelectric coupling effect in BiFeO$_3$

The magnetoelectric (ME) coupling effect for multiferroics is a hot topic in realizing the intrinsic mechanism of magnetic and electric structures. The ME coupling described as the spontaneous magnetization and polarization can interact mutually through linear, quadratic or even higher order effect. In terms of BiFeO$_3$ (BFO), the observed magnetic spiral propagation structure would result in the cancellation of the linear effect. However, the spiral propagation structure doesn’t exclude the quadratic ME effect. Tabares-Munoz *et al.*

observed the quadratic ME effect at temperature of 4 K.[85] Kadomtseva *et al.* observed the linear ME coupling effect by applying a strong magnetic field of ~ 20 T. That's because the field-induced phase transition suppresses the spin cycloid structure. This leads to the homogeneous ordered spin state to give out the giant ME effect.[86] Apart from the strong magnetic field induced linear ME effect, the spin cycloid structure can also be possibly destroyed by B-site magnetic element substitution,[87,88] film epitaxial growth methods etc.,[76] which could possibly generate the linear ME coupling effect.

(2) Aurivillus structure multiferroic of textured $Bi_{3.25}La_{0.75}Ti_{2.5}Nb_{0.25}(Fe_{0.5}Co_{0.5})_{0.25}O_{12}$ ceramic

Aurivillius bismuth layer-structured ferroelectrics (BLSFs) composed by the structure of regular stacking of $[Bi_2O_2]^{2+}$ layers and pseudo-perovskite $(A_{m-1}B_mO_{3m+1})^{2-}$ slabs, could be described as the general formula $(Bi_2O_2)^{2+}(A_{m-1}B_mO_{3m+1})^{2-}$, where m is the number of sheets of corner-sharing BO_6 octahedra. The origin of ferroelectricity in BLSFs is from the A- and/or B-site cations displacement in the perovskite blocks couples with the tilting of the BO_6 octahedra.[89,90] The offset of polarization between each BO_6 layer on *c*-axis only permits non-zero net polarization to appear along *c*-axis when the number of BO_6 layer is odd in BLSF, which makes the vast majority of ferroelectricity of BLSF almost appear only on *a-(b-)* axis.[90,91] Due to the excellent ferroelectric properties of BLSFs families, one of the typical BLSFs composition of $Bi_{3.25}La_{0.75}Ti_3O_{12}$ that possesses three layer structure was selected by Haixue and Zheng Li *et al.*[92] as the basic composition to build room temperature multiferroics ceramics. And I am very honoured that I am also one of the participator of this project. In our study, a range of compositions of general formulas $Bi_{3.25}La_{0.75}(Fe_{0.5}Co_{0.5})_xTi_{3-2x}Nb_xTi_3O_{12}$ were built. In the following sections, the crystal structure, ferroelectric, magnetic and magnetoelectric (ME) coupling properties of textured

$Bi_{3.25}La_{0.75}Ti_{2.5}Nb_{0.25}(Fe_{0.5}Co_{0.5})_{0.25}O_{12}$ ceramic are introduced since this composition presents the most excellent properties within this composition arrangement.

Crystal structure

The crystal structure of BLSFs of the basic unit $Bi_{3.25}La_{0.75}Ti_{2.5}Nb_{0.25}(Fe_{0.5}Co_{0.5})_{0.25}O_{12}$ can be described as Figure 2.21, which is a typical layered structure identical to the typical Aurivillius structure. This structure consists of the bismuth layer with general formula of a $(Bi_2O_2)_n^{2n+}$ and substituted BO_6 octahedral layers which can be described as $(Ti/Nb/Fe/Co)O_6$. The origin of ferroelectricity in $Bi_{3.25}La_{0.75}Ti_{2.5}Nb_{0.25}(Fe_{0.5}Co_{0.5})_{0.25}O_{12}$ is attributed to the tilting of the $(Ti/Nb/Fe/Co)O_6$ octahedra.[89,90] For the general BLSFs, the offset of polarization between each BO_6 layer on *c*-axis only permits non-zero net polarization to appear along *c*-axis when the number of BO_6 layer is odd in BLSF. This signifies that the $Bi_{3.25}La_{0.75}Ti_{2.5}Nb_{0.25}(Fe_{0.5}Co_{0.5})_{0.25}O_{12}$ presents ferroelectric polarization along both *a-(b-)* axis and *c*-axis, but the polarization is mainly along *a-(b-)* axis due to the offset on *c*-axis.[90,91] And the easy growth plane for BLSFs is also the *a-b* plane, which drives the texturized sintering of BLSFs ceramics. The textured BLSFs ceramic therefore possesses the electric properties orientation characteristic.[93] Moreover, in terms of $Bi_{3.25}La_{0.75}Ti_{2.5}Nb_{0.25}(Fe_{0.5}Co_{0.5})_{0.25}O_{12}$, the introduced the magnetic atoms (Fe/Co) on B-site is to generate the magnetic moment and the magnetoelectric coupling is hopefully produced through ligand field effect between electron spins of A-site magnetic atom and BO_6 octahedral tilting.[92]

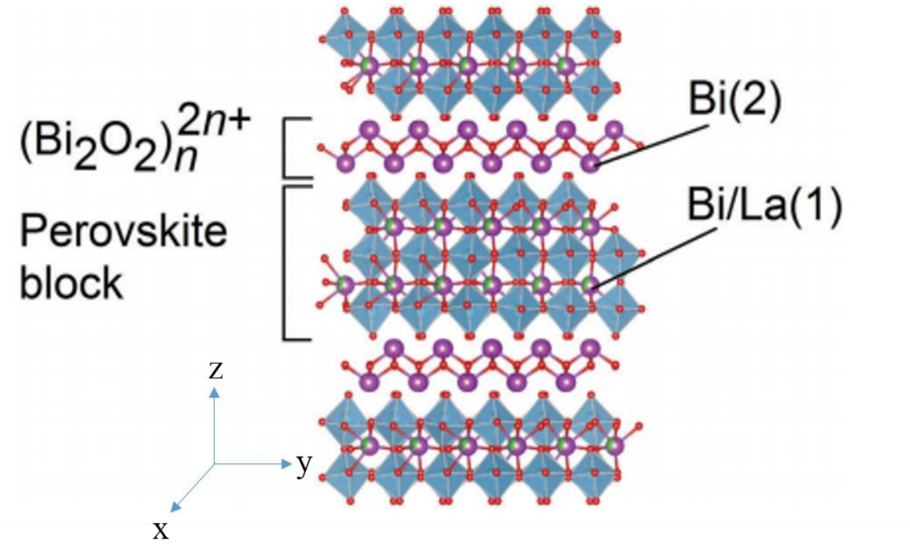

Figure 2.21 The projection of the structure $Bi_{3.25}La_{0.75}Ti_{2.5}Nb_{0.25}(Fe_{0.5}Co_{0.5})_{0.25}O_{12}$ along (110) direction. The purple and red balls represent the Bi and O atoms, respectively. And the partial substitution of Bi by La is represented by the partial green substituted balls. (Ti/Nb/Fe/Co)O_6 octahedra is shown by blue octahedral structure.[92]

Ferroelectric and dielectric properties of $Bi_{3.25}La_{0.75}Ti_{2.5}Nb_{0.25}(Fe_{0.5}Co_{0.5})_{0.25}O_{12}$

Figure 2.22(a) and (b) depict the polarization-current-electric field (*P-I-E*) hysteresis loops and the dielectric properties of textured $Bi_{3.25}La_{0.75}Ti_{2.5}Nb_{0.25}(Fe_{0.5}Co_{0.5})_{0.25}O_{12}$ ceramics measured perpendicular to the pressure applied direction under room temperature, respectively. The occurrence of two clear current peaks in *I-E* loops correspond to the ferroelectric domain switching based on the electric field reversal. The typical *P-E* hysteresis loops are clearly observed with the value of P_r up to 12.4 μC/cm^2. Figure 2.22(b) shows the temperature dependence of dielectric permittivity and tangent loss, the Curie point (FE T_c) of $Bi_{3.25}La_{0.75}Ti_{2.5}Nb_{0.25}(Fe_{0.5}Co_{0.5})_{0.25}O_{12}$ determined by the temperature point that corresponds to the dielectric maxima, which is around 556.5 K.

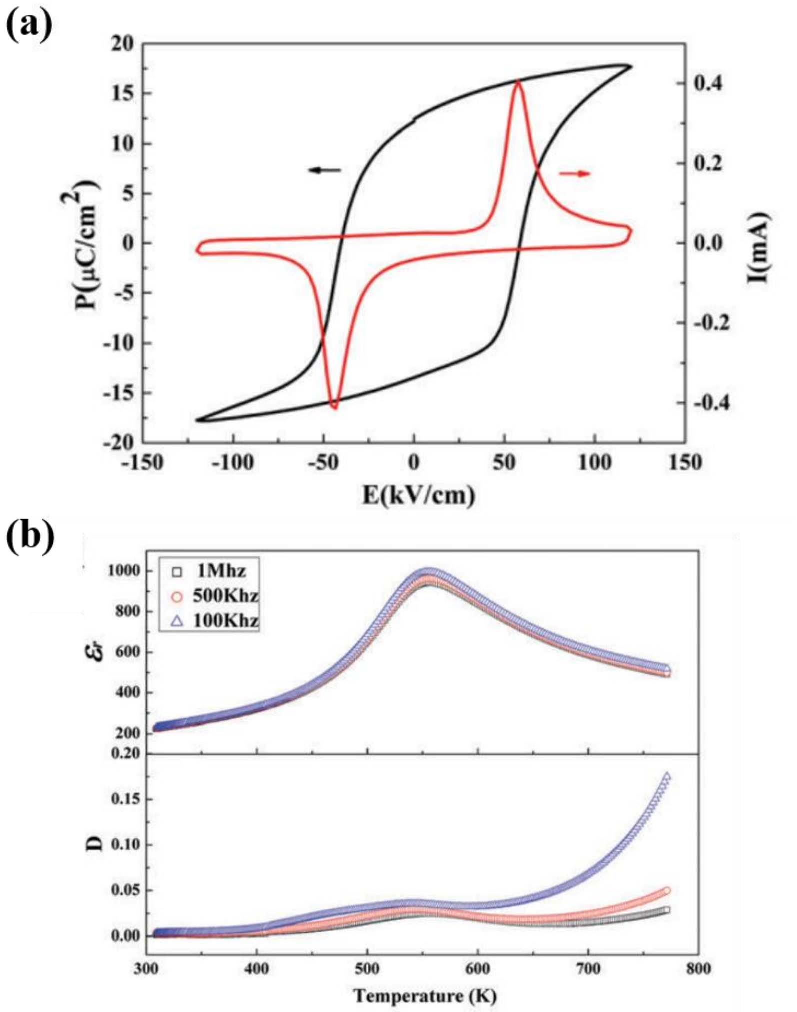

Figure 2.22 (a) The polarization-current-electric field (*P-I-E*) loops and (b) dielectric permittivity (ε_r) and dielectric loss (*D*) of the $Bi_{3.25}La_{0.75}Ti_{2.5}Nb_{0.25}(Fe_{0.5}Co_{0.5})_{0.25}O_{12}$ ceramics under room temperature.[92]

Magnetic properties of $Bi_{3.25}La_{0.75}Ti_{2.5}Nb_{0.25}(Fe_{0.5}Co_{0.5})_{0.25}O_{12}$

Figure 2.23(a) displays the magnetic field dependence of magnetization (*M-H*) loops for $Bi_{3.25}La_{0.75}Ti_{2.5}Nb_{0.25}(Fe_{0.5}Co_{0.5})_{0.25}O_{12}$ at 15 K, 50 K, 150 K and 200 K. Figure 2.23(b) shows the magnetic field dependence of magnetization (*M-H*) loops for $Bi_{3.25}La_{0.75}Ti_{2.5}Nb_{0.25}(Fe_{0.5}Co_{0.5})_{0.25}O_{12}$ at room temperature (300 K). The room-temperature (300 K) ferromagnetic nature can be strongly supported by this hysteresis loops with clear remnant magnetization (M_r).

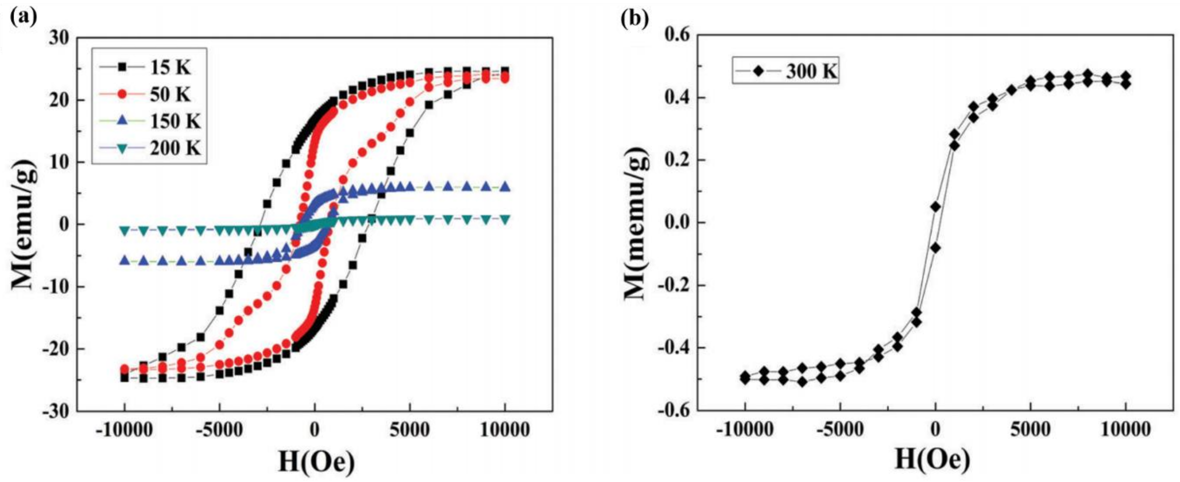

Figure 2.23 (a) The magnetic field dependence of magnetization (*M-H*) loops for $Bi_{3.25}La_{0.75}Ti_{2.5}Nb_{0.25}(Fe_{0.5}Co_{0.5})_{0.25}O_{12}$ at 15 K, 50 K, 150 K and 200 K. (b) The magnetic field dependence of magnetization (*M-H*) loops for $Bi_{3.25}La_{0.75}Ti_{2.5}Nb_{0.25}(Fe_{0.5}Co_{0.5})_{0.25}O_{12}$ at room temperature (300 K).[92]

The magnetoelectric (ME) coupling effect of $Bi_{3.25}La_{0.75}Ti_{2.5}Nb_{0.25}(Fe_{0.5}Co_{0.5})_{0.25}O_{12}$

Figure 2.24 illustrates the ferroelectric domain switching with magnetic field tuning under piezo force microscopic (PFM) observation. The areas marked by blue circles represent the region where magnetic response is tuneable by electric field. It is clearly observed that with changing magnetic field direction, the electric domain structure changes simultaneously, which visually indicates the ME coupling effect of $Bi_{3.25}La_{0.75}Ti_{2.5}Nb_{0.25}(Fe_{0.5}Co_{0.5})_{0.25}O_{12}$.

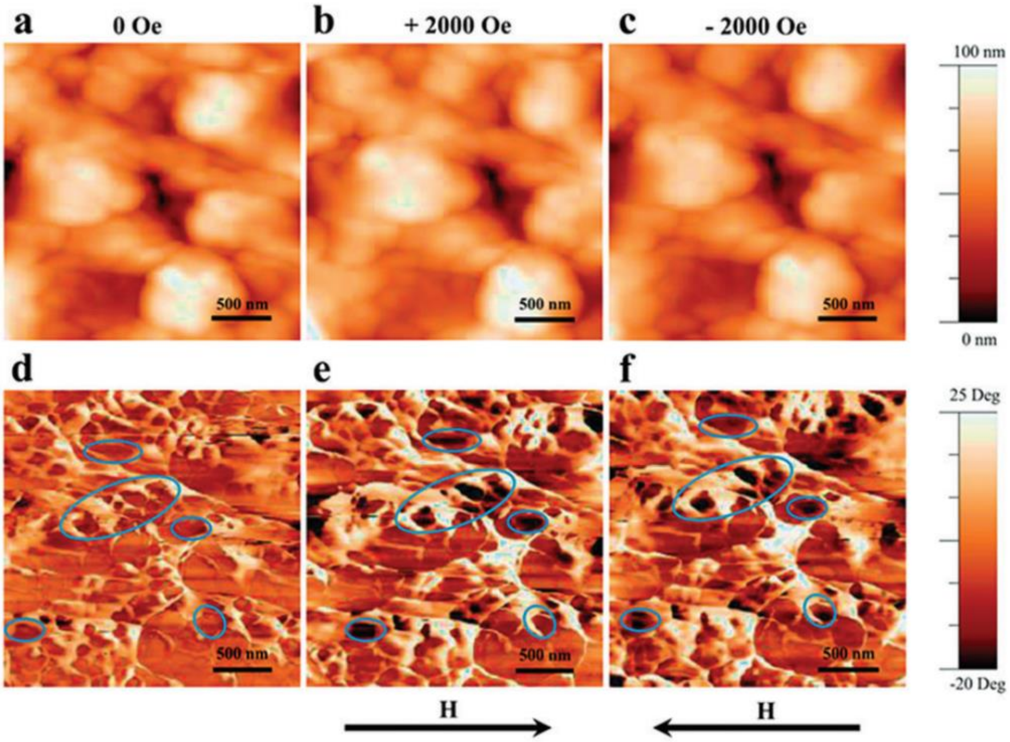

Figure 2.24 The ferroelectric domain switching with magnetic field tuning under piezo force microscopic (PFM) observation. (a) Topology and (d) vertical phase under zero magnetic field, (b) topology and (e) vertical phase under +2000 Oe, (c) topology and (f) vertical phase under -2000 Oe. The areas marked by blue circles represent the region in where magnetic response is tuneable by electric field.[92]

2.3.3 The mechanism of multiferroics composites

Due to the deficiencies of the natural multiferroics under real application conditions (e.g. room temperature, low driving electric/magnetic field), Van Suchtelen proposed the concept of a two-phase ME composite material in 1972, arising from an elastic coupling between two phases of different properties. The first work on the multiferroics composites was fabricated at the Philips laboratory. They fabricated two or more compound materials with some parts being piezomagnetic phase and others being piezoelectric phase, which was possible to build up the coupling connectivity between them.[94-97] The coupling is generally generated directly via strain among each phase, the magnetostrictive effect (magnetic/mechanical effect) in piezomagnetic phase and piezoelectric effect in the piezoelectric phase, which could be expressed as below:[4,98]

$$ME_H\ effect = \frac{magnetic}{mechnicial} \times \frac{mechnicial}{electric}$$

$$ME_E\ effect = \frac{electric}{mechnicial} \times \frac{mechnicial}{magnetic}$$

The piezomagnetic and piezoelectric effects can be formulized further as:[4]

$$\frac{\delta S}{\delta H} = e^m \text{ and } \frac{\delta E}{\delta S} = e \tag{2.8}$$

where S is the strain, H is the magnetic field, E is the electric field, e^m is the piezomagnetic coefficient and e is the piezoelectric coefficient.

Then, the ME coefficient can be characterised by:[4]

$$\frac{\delta E}{\delta H} = \alpha = k_c e^m e \tag{2.9}$$

where k_c is the coupling factor ($0 \leq k_c \leq 1$), α is the ME coefficient of the composite. The interaction coupling between magnetic phase and piezoelectric phase is via elastic interaction. For the ME_H effect, the shape of magnetostrictive phase is changed by applied magnetic field, and then the strain passes to the piezoelectric phase, generating an electric polarization/signal, and vice versa. Therefore, high piezomagnetic and piezoelectric coefficient materials with high coupling factor are expected to lead to the large ME coefficient.[99] By controlling the synthesis conditions such as constituent materials, mole ratios and sintering process, composites have already achieved up to five orders of magnitude beyond the single phase multiferroics on ME coefficient.[100]

The bulk multiferroics composites

Even though the multiferroics composites have many connective modes according to the classification of piezoelectric composites by Newnham *et al.*[98], the most common bulk multiferroics composites were classified into three types. They are named as 0-3, 1-3, 2-2 types, corresponding to the particulate, fibre/rods and laminate embedding mode, respectively, as shows in Figure 2.25. In 1994, I. Getman[4,101] modelled the linear magnetoelectric effect in two-phase composites of piezoelectric and piezomagnetic components theoretically, and found that the magnetoelectric coefficient of 2-2 multiferroics composite can reach over 1 $V\cdot cm^{-1}\cdot Oe^{-1}$, which is higher than the simulation value for 0-3 particulate ceramic composites. Moreover, because the 1-3 composites are hard to prepare experimentally, the 2-2 laminate composites are the most potential mode for fabricating multiferroics composites.

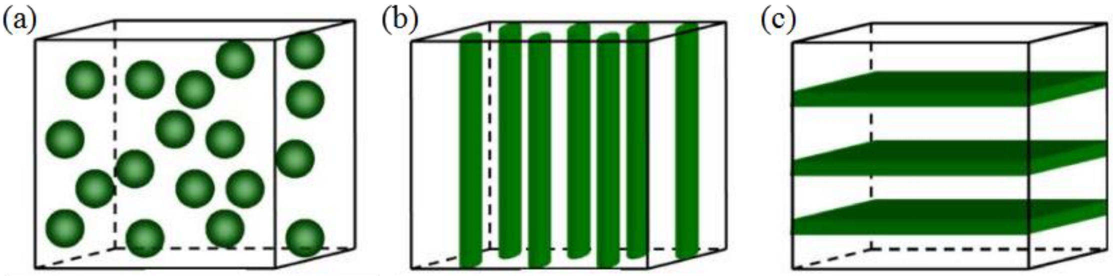

Figure 2.25 Three different types of bulk composites. (a) 0-3 particulate composites: the piezomagnetic/ piezoelectric particles are embedded into the piezoelectric/piezomagnetic matrix; (b) 1-3 fibre/rods composites: the piezomagnetic/piezoelectric fibre/rods are embedded into the piezoelectric/piezomagnetic matrix; (c) 2-2 laminate composites: the structured multiferroics composites consist of piezomagnetic/piezoelectric layers.[4]

2.3.4 The multiferroics composites

The early magnetoelectric composite was reported by the Philips laboratory in 1970s through in-situ grown eutectic and regular sinter methods.[102,103,95,104] This ME composite material was made by sintering a mixture of piezoelectric and piezomagnetic phase, which was the combination of $BaTiO_3$-Ni(Co, Mn)Fe_2O_4 (BTO/CFO). The maximum ME coefficient is about 80 $mV\cdot cm^{-1}\cdot Oe^{-1}$,[96] which is much higher than that of single phase materials. After the successful characterization on BTO/CFO, varieties of composites were fabricated to try to obtain higher ME coefficient. The choice of piezoelectric and piezomagnetic depends on their Curie temperature, high piezoelectric and piezomagnetic effects, high mechanical coupling between electric and magnetic phases and good durability. Table 2.5 lists four different multiferroics composites with relatively high ME coefficient. In this section, Terfenol-D/PVDF will be discussed particularly due to its outstanding properties and lead-free contamination.

Table 2.5 Four multiferroics composites with high ME field coefficient

Material	**Composition**	α_E ($mV\cdot cm^{-1}\cdot Oe^{-1}$)
Multiferroics Composites	$0.3CuFe_2O_4$-$0.7PbZr_{0.53}Ti_{0.47}O_3$[105]	425
	$0.3CoFe_2O_4$-$0.7BiFeO_3$[106]	285
	Terfenol-D/PVDF[107,108]	1430-7930
	$0.5Ni_{0.83}Co_{0.15}Cu_{0.02}Fe_{1.9}O_4$-0.5 $PbZr_{0.52}Ti_{0.48}O_3$[109]	3150

Terfenol-D/PVDF

Terfenol-D/PVDF consists of magnetostrictive $Tb_{0.27-0.3}Dy_{0.73-0.7}Fe_{1.90-1.95}$ (Terfenol-D) alloy and piezoelectric polyvinylidene fluoride (PVDF) layers.

$Tb_{0.27-0.3}Dy_{0.73-0.7}Fe_{1.90-1.95}$ (Terfenol-D) is a giant magnetostrictive material known in 1970s and has been commercialized since 1980s.[110] Terfenol-D is a sort of RFe_2 compound with cubic laves structure, as shown in Figure 2.26.[111] This material has excellent elongation, outstanding mechanical-magnetic energy transfer coefficient and high energy density under room temperature, exhibiting great potential applications up to 10 kHz AC magnetic field frequency.[112] The magnetostriction coupling factor K_{33} is a magnitude to characterise the transferring efficient between magnetic energy and mechanical energy, which can be formularized as:[113,114]

$$k_{33} = \left(\frac{{d_{33}}^2}{s_{33}^H \mu_{33}^T}\right)^{1/2} \tag{2.10}$$

where d_{33} is the piezomagnetic constant, μ_{33}^T is the permeability, s_{33}^H is the elastic compliance coefficient. k_{33} is highly affected by two main characteristics which are "jump effect" and magnetostrictive anisotropy. The k_{33} in Terfenol-D could reach 0.72 under axial compressive pressure along the easy magnetization axes of <111> direction, which is an extremely outstanding value.[113,115,116]

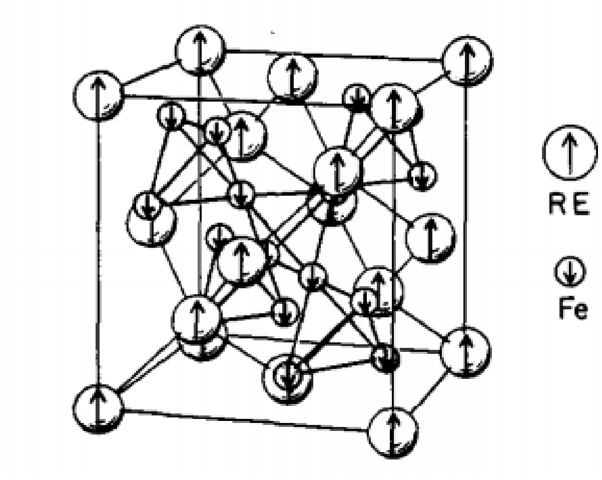

Figure 2.26 Crystal structure of the cubic Laves phase compounds.[111]

Polyvinylidene fluoride (PVDF) is a semi-crystalline polymer with repeated unit of $-(CH_2CF_2)_n-$ with outstanding piezoelectricity at around d_{33} = 20 pC/N and good ferroelectricity with spontaneous polarization around 8 μC/cm^2.[117] PVDF film is commonly manufactured by solidifying the film from molten liquid phase, and followed by a stretch along particular direction and then poled. In terms of the liquid phase, each individual polymer chain is free to occupy any orientation and results in zero net dipole moment. After solidification and stretching the polymer along particular direction, the chains are commonly aligned along the stretch direction. With the combination of poling, the permanent dipole moment of the PVDF films is produced and therefore the piezoelectric is imparted.[118] PVDF polymorphism is well known for possessing four crystalline phases, named α, β, γ and δ phases, as shown in Figure 2.27.[119] The most excellent form with the ferro-, piezo-, pyroelectric properties, is the β phase.[120] The current reports illustrate that fabricating 100 % pure β phase in PVDF is possible by producing nanocomposites between PVDF and carbon nanotubes (CNTs), with the proper modification of CNTs.[120]

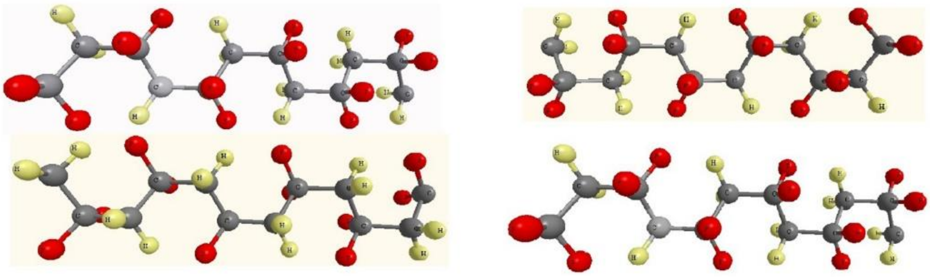

α-phase δ-phase

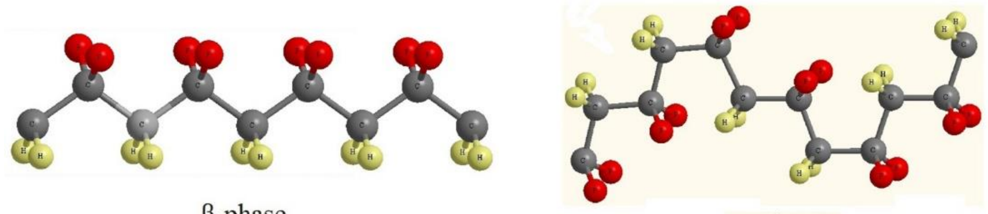

β-phase γ–phase

Figure 2.27 The four different phases molecule chains of PVDF. The grey balls represent the carbon atoms, yellow balls represent the hydrogen atoms and red balls represent fluorine atoms.[120]

The Terfenol-D/PVDF reported by Kiyotake Mori *et al.* in 2002 is composed by PVDF film as piezomagnetic phase and Terfenol-D as piezoelectric phase.[107] The 110 μm-thick PVDF film was electrically poled and then coated with silver electrodes on both sides. The film was then bonded by ultra-thin layer of epoxy onto the Terfenol-D bulk directly. This absolute ME coefficient of Terfenol-D/PVDF composite was optimised to 1430 mV·cm^{-1}·Oe^{-1} under regular mode (longitudinal or transverse magnetostrictive mode), as shown in Figure 2.28. The max ME coefficient corresponds to the point of the optimum ration of f_1 (piezoelectric material) and f_2 (piezomagnetic material), labelled by the open dot.[107]

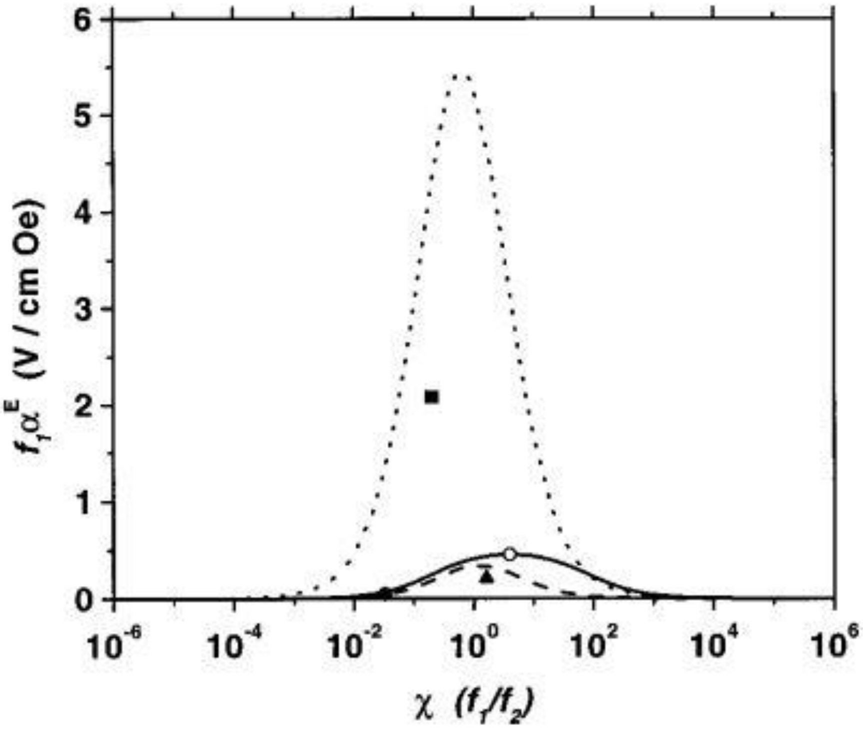

Figure 2.28 Analytical prediction of ME_H voltage coefficients of ME composite depending on the volume fraction relation between f_1 (piezoelectric material) and f_2 (piezomagnetic material). Terfenol/PVDF: solid line-calculated, • (solid dot)-measured, o (open dot)-optimum. $BaTiO_3/CoFe_2O_4$ dashed line-calculated, ▲ (solid triangle)-measured, PMN-PT/Terfenol-D: dotted line-calculated, ■ (solid square)-measured.[107]

In addition, for the Terfenol-D/PVDF/Terfenol-D laminated composite, the ME coefficient could up to 7930 $mV\cdot cm^{-1}\cdot Oe^{-1}$ under a DC bias of 2300 Oe with shear-shear mode reported by Meng-Chien Lu *et al.*[108] The principle of shear-shear mode is shown as Figure 2.29. A DC magnetic field and an AC magnetic field were applied simultaneously on the Terfenol-D layer, which would generate a displacement of Terfenol-D layer along the x-axis and further couple to the piezoelectric layer. Then the corresponding charge output will be generated in the piezo-layer.[108]

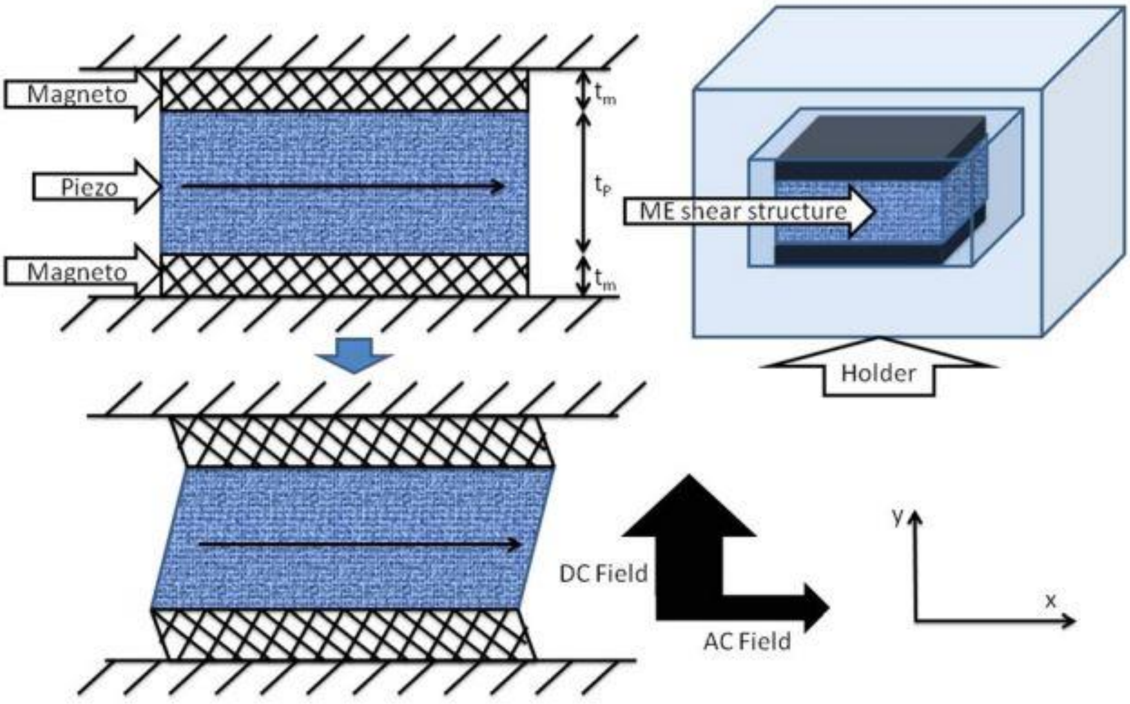

Figure 2.29 Schematic diagram of the principle of shear-shear mode ME sensor. The direction of DC and AC magnetic field in the magnetostrictive layer were marked by two black arrows.[108]

2.4 The potential application of multiferroics

Since the room temperature single phase multiferroics are very rare, the applications based on intrinsic multiferroicity within electrons' spin scale are still in dark. However, the macro magnetoelectric (ME) coupling between piezoelectric and piezomagnetic effect is well-developed upon composites and films. The great achieving ME coupling effect makes them present great potential on applications. Depending on the ME coupling effect, several applications such as magnetoelectric modulate sensor, high speed read-write memory, high-sensitive inductor and high-frequency signal processing device, has been proposed. Recent progress in design, fabrication and the characterizations of properties will be discussed in this section.

2.4.1 Magnetic field sensors and transducers

The ME material-based sensor devices are thought to act as the alternatives for traditional giant magnetoresistive (GMR) devices and Hall sensors. The low power consumption and no need of the cryogenic cooling are the main advantages for ME sensors comparing to conventional GMR and Hall sensors. The high-sensitive ME materials are proposed to be able to detect tiny magnetic field by monitoring the electric field induced by ME coupling effect. Commonly, when referring to the regular GMR and Hall magnetic sensors in the actual applications, the potentially high sensitive ME magnetic field sensors and transducers are proposed to meet several requirements listed below:

(1) High magnetic field measurement range: from below 10 μT to above 20 T. (Note: 1T = 10^4 Oe = 10^4 G = 10^6 μT = 10^9 nT = 10^{12} pT= 10^{15} fT = 10^{-18} aT = $1/4\pi\times10^7$ A/m)

(2) High signal to noise ratio (SNR). A higher SNR means a better capability of the higher sensitive for field detection.[121]

(3) High detection resolution. The magnetic field resolution of sensors should be detectable for aT or fT per $\sqrt{Hz}$ at low frequencies (10^{-2} to 10^3 Hz), referring to the SQUIDs sensitive to magnetic field as low as 5 aT (5×10^{-18} T). The resolution of different magnetic sensors is illustrated in

Figure 2.30.[122] The magnetic field resolution is also called equivalent magnetic noise (EMN). The EMN is mainly composed by two parts, dielectric loss noise (N_{DE}) and DC leakage resistance noise (N_R), which can be formularized by:[123,124]

$$N_{DE} = \sqrt{\frac{4kTC_p tan\delta}{2\pi f}} \tag{2.11}$$

$$N_R = \frac{1}{2\pi f}\sqrt{\frac{4kT}{R_{DC}}} \tag{2.12}$$

$$N_t = \sqrt{N_{DE}^2 + N_R^2} \tag{2.13}$$

The EMN can be further expressed via the total noise charge density N_t and the ME charge coefficient:[125]

$$EMN\left(\frac{T}{\sqrt{Hz}}\right) = \frac{N_t(C/\sqrt{Hz})}{\alpha_Q(C/T)} = \frac{\sqrt{\frac{4kTC_p tan\delta}{2\pi f} + \frac{1}{(2\pi f)^2}\frac{4kT}{R_{DC}}}}{\alpha_Q} \tag{2.14}$$

where k is Boltzmann constant, T is the temperature with unit kelvin, C_p is the capacitance, tan δ is the dielectric loss, R_{DC} is the resistance under DC magnetic bias field, f is the magnetic frequency in Hz and α_Q is the ME charge coefficient with unit of (C/Oe). Based on equation (2.11)-(2.14), two methods can be employed to achieve a low EMN: (1) to decrease capacitance and dielectric loss or increase DC resistance and (2) to increase the α_Q.

(4) High range of ambient temperature for applications and wide bandwidth (0.1 to 100 Hz) operation.[126]

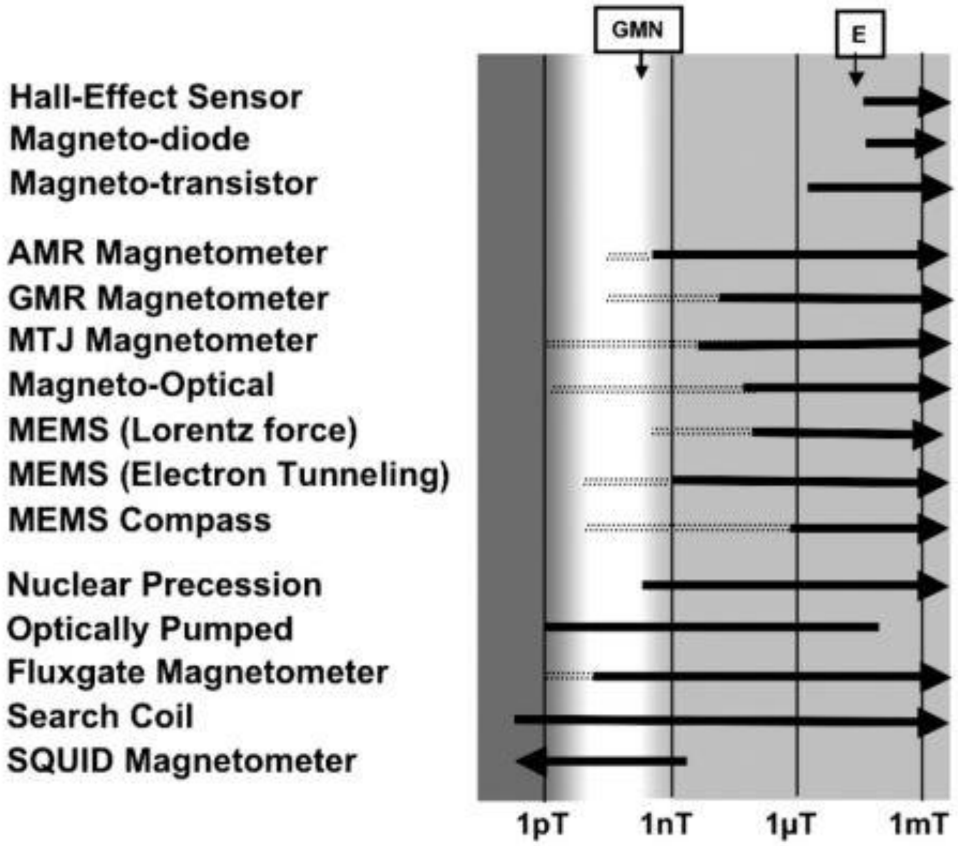

Figure 2.30 The sensitivity of different magnetic sensors. The symbol E and GMN represent the strength of the Earth's magnetic field and geomagnetic noise, respectively.[127]

In the follow section, three sets of ME composites that have potential magnetic field sensor applications will be introduced.

An ultra-low magnetic noise composite was also reported by Fang *et al.*[124] in 2015. It consists of Metglas/Mn-doped $Pb(Mg_{1/3}Nb_{2/3})O_3$-$PbTiO_3$ fibre. The structure and magnetic noise of this laminated composite are shown in Figure 2.31. In this work, Metglas/Mn-doped $Pb(Mg_{1/3}Nb_{2/3})O_3$-$PbTiO_3$ (PMNT) laminate composite was fabricated with an in-plane connected structure. The Mn-PMNT was grown directly from the melt by an improved Bridgman technique, and the Mn-PMNT fibres were carefully selected upon the value of C_p (~ 7.2 nF), piezoelectric constant (~ 1200 pC/N) and the dielectric loss tan δ (~

1.8 ‰). The fibres were then poled before fabrication to acquire a larger piezoelectricity. The extremely low dielectric losses of this poled single crystal Mn-PMNT can dramatically lower the N_{DE} of this composite.

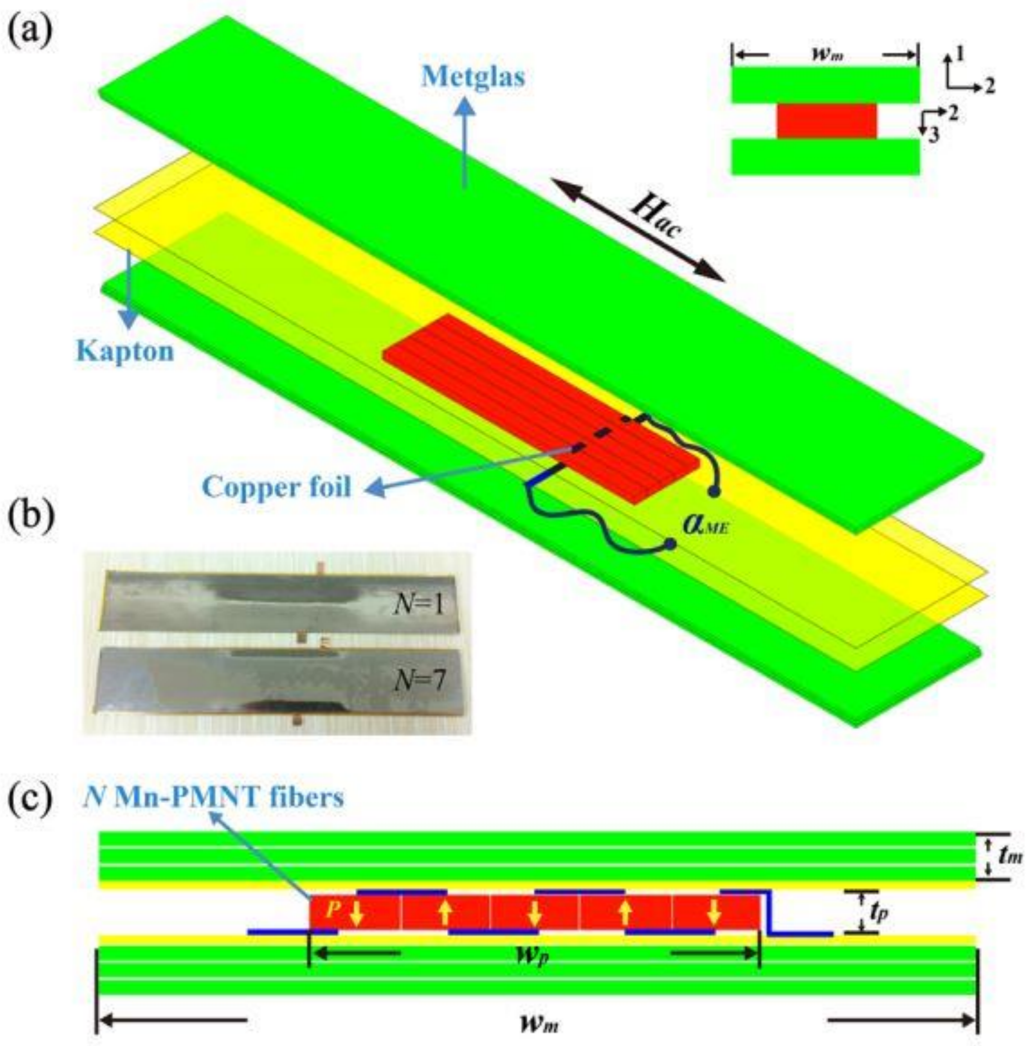

Figure 2.31 Schematic for (a) 3D structure, (b) photograph and (c) cross-sectional schematic diagram of the Metglas/Mn-PMNT composite.[124]

The numbers of Mn-PMNT fibres (N), was introduced to find out the most promising fabrication method, as shown in Figure 2.31(c). Theoretically, the number of Mn-PMNT fibres generates inversely proportional correlation with C_p, and based on equation (2.11)-(2.14), the decrease of C_p will give out a decrease on EMN. Furthermore, the increasing number of Mn-PMNT will theoretically result in the increase of C_p and decrease of R_{DC},[128,129] and the α_Q will keep as constant. The frequency dependence of equivalent magnetic noises (EMN) of four different configurations with different N is shown in Figure 2.32(a). It could be found that the EMN decreases with increasing N over the entire frequency range. The inset of Figure 2.32(a) illustrates that the sensor achieves a high signal to noise ratio at 15. And for a particular frequency of 30 Hz, the measured EMN and N_t decrease with increasing N, and as low as 0.87pT/$\sqrt{Hz}$ at 30 Hz when $N = 7$ in Figure 2.32(b).[124]

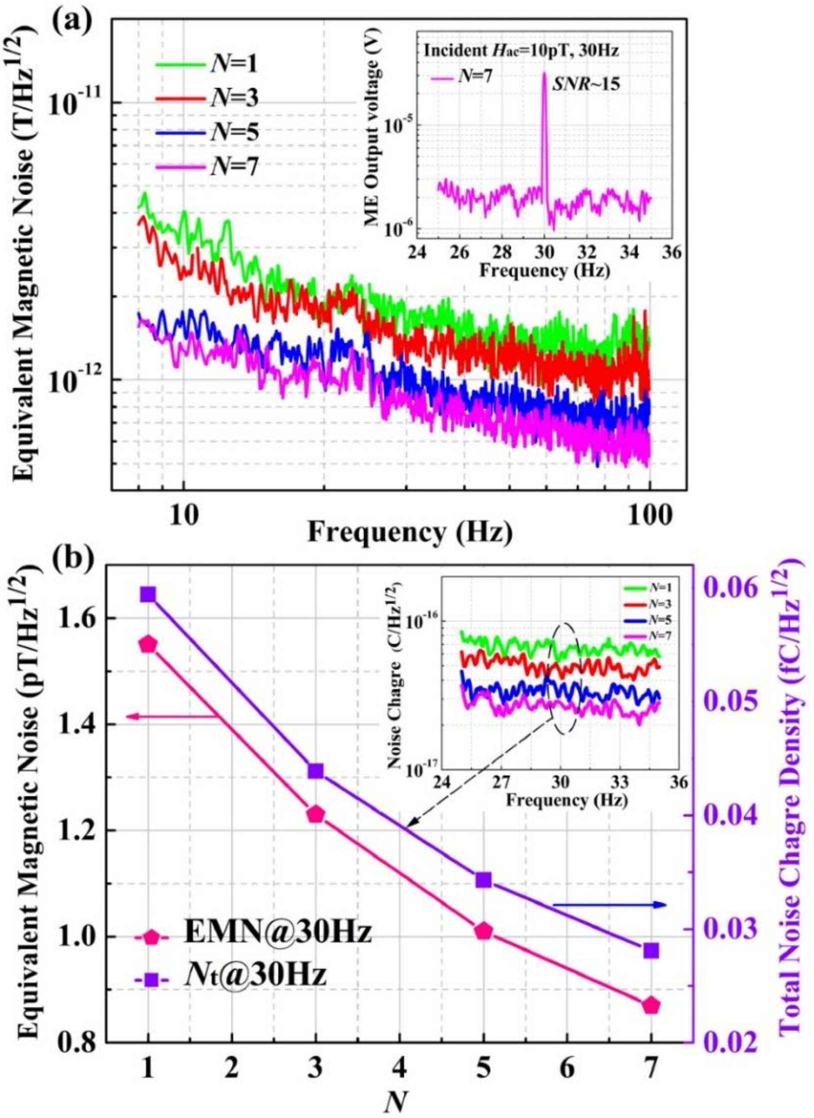

Figure 2.32 (a) The frequency dependence of EMN with different numbers of PMNT fibers (*N*) for Metglas/Mn-PMNT sensors. (b) The PMNT fibers number *N* dependence of EMN and N_t for Metglas/Mn-PMNT sensors at 30 Hz. The inset illustrates the N_t of the sensors with different PMNT fibers number over the frequency range between 25 Hz and 35 Hz.[124]

Lee *et al.*[130] reported a ME AC/DC magnetic field sensor fabricated by using $Pb(Zr_{0.52}Ti_{0.48})O_3$ (PZT) and $Tb_{0.3}Dy_{0.7}Fe_{1.9}$ (Terfenol-D) thin films in the form of 2.98 µm-thick and 300 µm-long micro-cantilevers (Figure 2.33(a) and (b)). These micro-cantilevers were composed of eight layers, which are SiO_2 (100 nm)/SiN_x (1.2 μm)/Ta (30 nm)/Pt (150 nm)/PZT (1μm)/Pt (100 nm)/SiO_2 (100 nm)/Terfenol-D films (300 nm), from bottom to the top layer. The cantilever structure is shown in Figure 2.33. The PZT was coated by platinum layer which allows the output electric signal be measured directly from the platinum electrode. And the inserted SiO_2 is used for preventing the direct contact between PZT and Terfenol-D. The deposited cantilevers were formed by well-crystallized large grains in Figure 2.33.

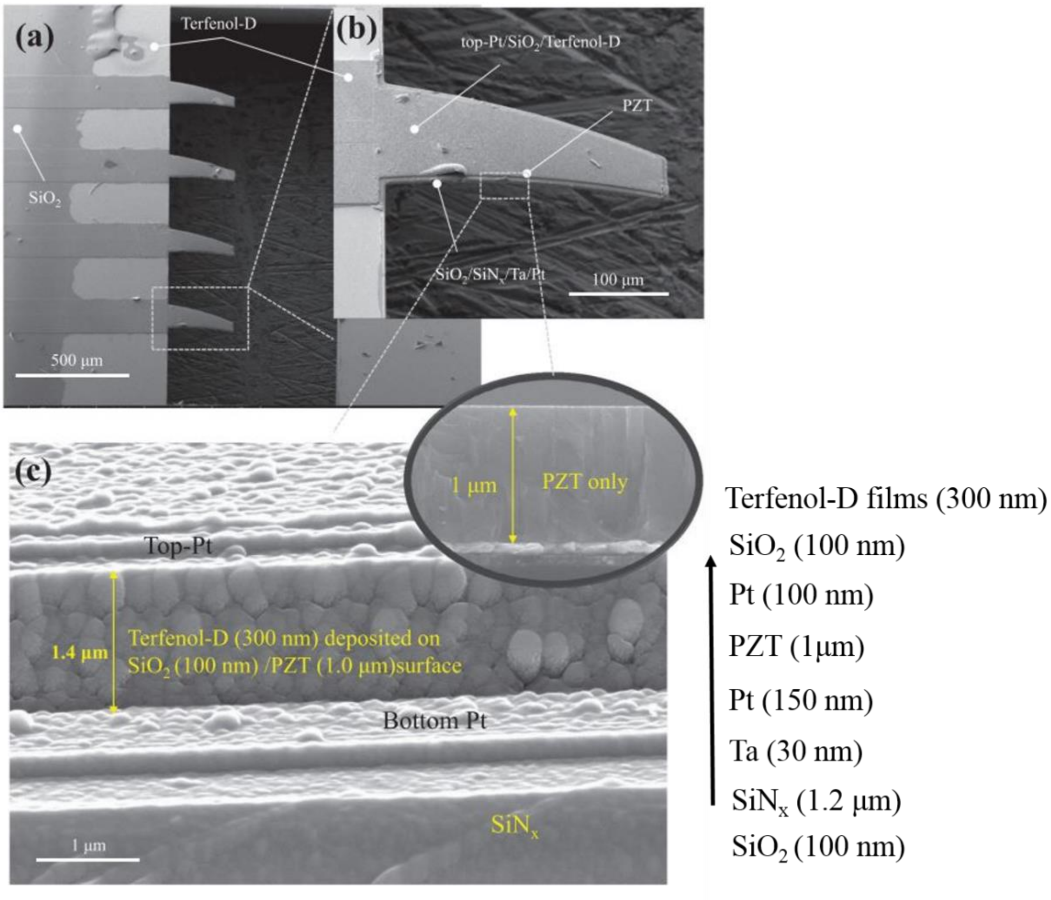

Figure 2.33 SEM images micro-cantilever consisting of Terfenol-D and PZT thin film. (a) The morphology of four cantilevers, (b) magnified image of single cantilever and (c) cross section images of cantilever.[130]

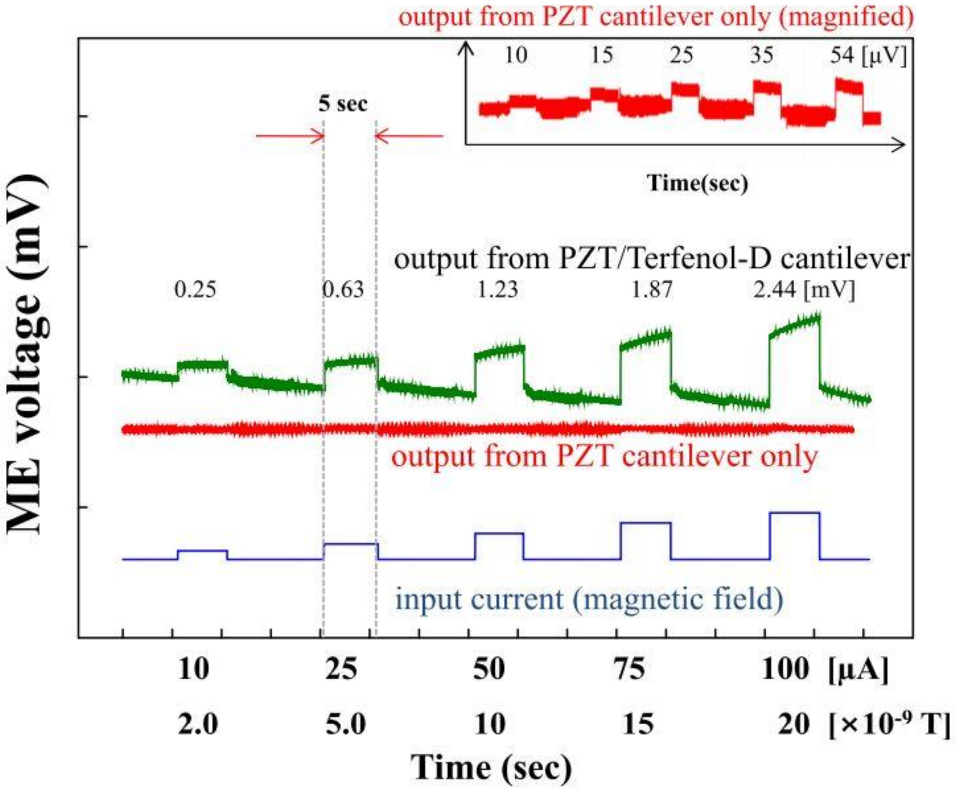

Figure 2.34 The ME output voltages from pure PZT cantilever and PZT/Terfenol-D cantilever under a varying AC magnetic field from 2×10^{-10} T to 2×10^{-9} T. The green line exhibits a sync variation with AC magnetic field frequency and magnitude. However, the red line measured from PZT-only cantilever shows a negligible output. The inset depicts the extremely small value of magnetic field induced output ME voltage of pure PZT cantilever by magnified the raw data.[130]

As shown in Figure 2.34, the output ME voltage signal of PZT/Terfenol-D cantilever was measured under an increasing DC magnetic field from 2×10^{-9} T to 2×10^{-10} T with a small AC magnetic field (60 Hz, 1 Oe). The ME voltages from ME coupling effect were determined as 0.25 mV, 0.63 mV, 1.23 mV, 1.87 mV and 2.44 mV with magnetic field at 2.0×10^{9} T, 5.0×10^{9} T, 10×10^{9} T, 15×10^{9} T, and 20×10^{9} T, respectively. The voltage output for the PZT-only cantilever, marked by the red line in Figure 2.34, is negligible under the same measurement conditions, which reveals that Terfenol-D is the main part for bringing in the piezomagnetic parts. The inset in Figure 2.34 further shows a magnified output ME voltage of PZT-only cantilever. It could be found clearly that the ME voltage for PZT-only cantilever is almost two orders of magnitude lower than PZT/Terfenol-D cantilever.[130]

These two reports proved that ME composites possess extremely low EMN at pT/$\sqrt{Hz}$ scale and have apparent ME coupling effect even at very small magnetic field at nT level. However, the highest resolution is still too low to complete accurate sensing work (referring to the sensitivity of SQUIDs at aT level), which indicates that ME composites are still far away from high sensitive magnetic field sensing. Nevertheless, the advantages such as low power consumption and no need for the cryogenic cooling still make ME composites as a promising option for magnetic field sensors.

2.4.2 Magnetoelectric nanoparticles for targeting therapy

The development and design of personalized nanomedicine for better health quality is a highly-focused direction in life science. For the sake of delivering and releasing a therapeutic concentration at the target site, novel magnetoelectric nanoparticles (MENs) were designed. MENs have outstanding properties like high drug loading amount, site-specificity and precise on-demand controlled drug delivery.[131]

Rakesh *et al.* reported that the $CoFe_2O_4$-$BaTiO_3$ (CFO-BTO) core-shell structure MENs can be used as the carriers to implement this hypothesis.[132] They successfully delivered drug into human ovarian carcinoma cells (SKOV-3) by CFO-BTO MENs. The drug intake strength by cell was proved by fluorescence imaging experiments as magnetic field dependence. The challenge was addressed through some new concepts that exploited: (i) the electrical properties are different between tumour cells and healthy cells; (ii) the magnetoelectric nanoparticles act as the converters by adjusting the magnetic field energy to change the MENs' intrinsic electric field energy. This characteristic allows the remote control of the electric field of tumour cells, which will modulate the pores on membrane and trigger specificity drug uptake activities.[132] The therapy process involves three threshold values of magnetic field, H_{th}, H_r and H_{th_health}. H_{th} is the critical magnetic field value above which would cause electroporation on tumour cells. H_r is the critical magnetic value above which would result the drug be released from MENs carriers. Usually, H_r is higher than H_{th}. Most importantly, the threshold magnetic field of electroporation of health cell H_{th_health} must be higher than H_r. For the therapy process as shown in Figure 2.35(a)-(c), firstly, the MENs carriers with drugs dispersed around tumour cells, and then, when the applied magnetic field $H > H_m$, the ME effect of the MENs will generate a native huge electric field around membrane to open up the pore on membrane base on electroporation mechanism, and the pores allow the MENs carriers go across cell membrane.[133] Then, with the applied magnetic field further increase to $H > H_r$, the drug can be released off by overcoming the binding force between MENs and drug. This field strongly depends on the binding force between MENs and drugs and can be tuned in a large range through employing different coating materials, field excitation frequencies and treatment durations.[132,134]

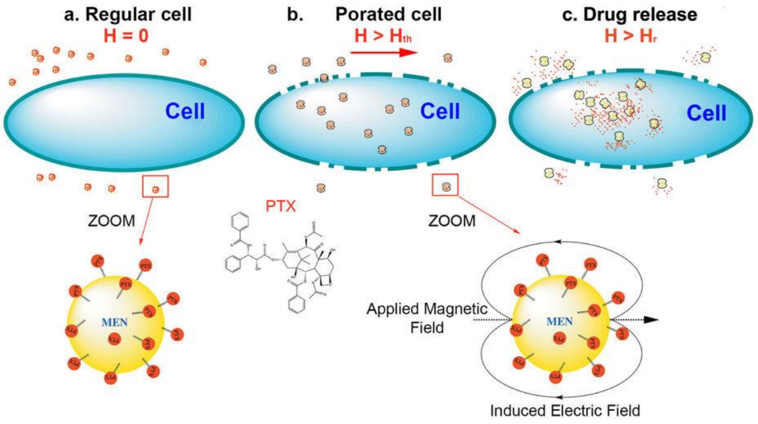

Figure 2.35 The brief process of MENs therapy. a: the membrane of regular tumor cell; b: the pores of membrane are produced under magnetic field applied and the MENs carriers would go throughout the pores of cells; c: when magnetic field is increased to a higher value beyond H_r, the drug is released into targeted cells.[132]

To understand the magnetic field dependence of the drug intake process, Rakesh *et al.* performed the cellular drug uptake experiments under a varying magnetic field applied on both cancer ovarian cell (SKOV-3) and healthy ovarian cell (HOMEC). The results of fluorescence imaging experiments are shown by Figure 2.36. When magnetic field at 5 Oe, 15 Oe, 30 Oe, the corresponding drug intake percentage per 1 mg celluelar cell protein are 1.50 ± 0.41, 2.36 ± 0.48, and 10.41 ± 1.54 % for SKOV-3. While for the HOMEC, the values are 0.18 ± 0.07, 0.30 ± 0.04, and 0.55 ± 0.16 %, respectively. It could be found that the drug uptake by SKOV-3 shows strong dependence correlation with magnetic field. However, it is also notable that the drug barely affected the drug uptake of HOMEC in this field range.

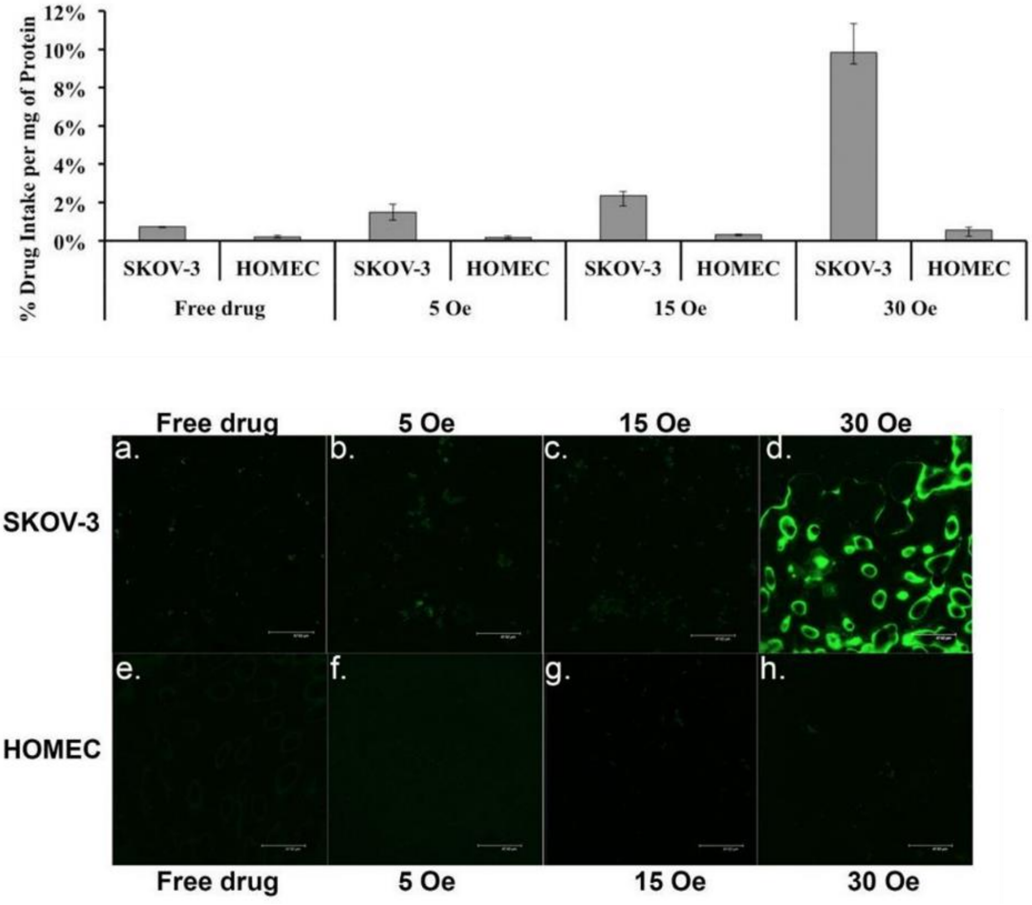

Figure 2.36 Magnetic field dependence of the drug uptake by SKOV-3 and HOMEC cells.[132]

In summary, the tunability of magnetoelectric properties induced remotely controlled drug release of MENs makes it suitable for the demand of delivering desired drug with high loading and high site-specificity. By building on these advantages, it can not only be used for therapy on cancer, but also give a perspective to curing HIV, Parkinson's disease and Alzheimer's disease.[131]

2.4.3 Magnetoelectric Random Access Memory (MERAM)

The volatility of Ferroelectric random access memory (FeRAM) and the huge currents consumption in the writing process in magnetic random access memory (MRAM) restrict the applications for both FeRAM and MRAM. The electric-field write, magnetoresistance read memory composed of magnetoelectric media that combine both the advantages of FeRAM and MRAM has been came up and is called magnetic-electric random access memory (MERAM). MERAM can offer greater memory density, lower power consumption and higher thermal stability. Due to its outstanding magnetoelectric properties, the multiferroics heterostructure, consisting of ferromagnetic (FM), antiferromagnetic (AFM), ferroelectric (FE) and ferroelastic phase, has been selected as the configuration for MERAM prototype.[135,136]

In terms of heterostructure, the characteristic called "exchange bias", is the most essential properties during manufacturing MERAM. When magnetoelectric layered heterostructure with ferromagnetic (FM)-antiferromagnetic (AFM) interfaces cooled from T ($T > T_N$) and through T_{Neel} of AFM (with the selected FM materials, T_c above the T_N), an anisotropy ("exchange bias") is induced in the FM. This anisotropy was firstly discovered by Meiklejohn and Bean in 1956 from the work on Co particles embedded in native AFM oxide (CoO).[137] The typical phenomenon is that the hysteresis loops of AFM-FM system after field cooling to $T < T_N$ would shift to the opposite direction. This hysteresis loops shift behaviour is known as exchange bias, H_E (see Figure 2.37). This phenomenon provides the anisotropy magnetoresistance for magnetic recording media applications. The magnetoresistance here is the change of electrical resistivity of the material under the applications of magnetic field.

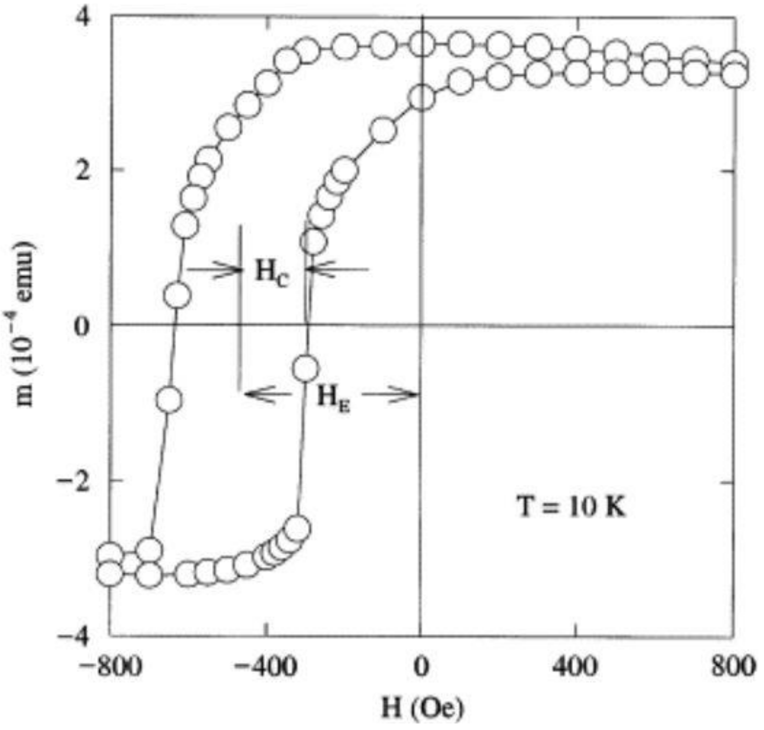

Figure 2.37 *M-H* hysteresis loops of FeF_2/Fe bilayer structure at $T = 10$ K after field cooling.[137]

The mechanism of the interaction on the AFM-FM interface is shown in Figure 2.38(i)-(v). When $T_N < T < T_C$ with a applied magnetic field, the spins of FM layer align toward single direction while the spins of AFM layer remain random. When cooling to $T < T_N$ due to the interface interaction between AFM and FM layer, the AFM spins next to the FM layer keep the same spin direction with the spins in FM layer by a exerted torque between them. The torque was marked by small grey pillars between black and grey arrows in Figure 2.38(iii).[138] Therefore, the magnetic field required to reverse the spins in FM will be larger because an extra field is needed to overcome the microscopic torque. However, the details of the intrinsic mechanism is still unclear.

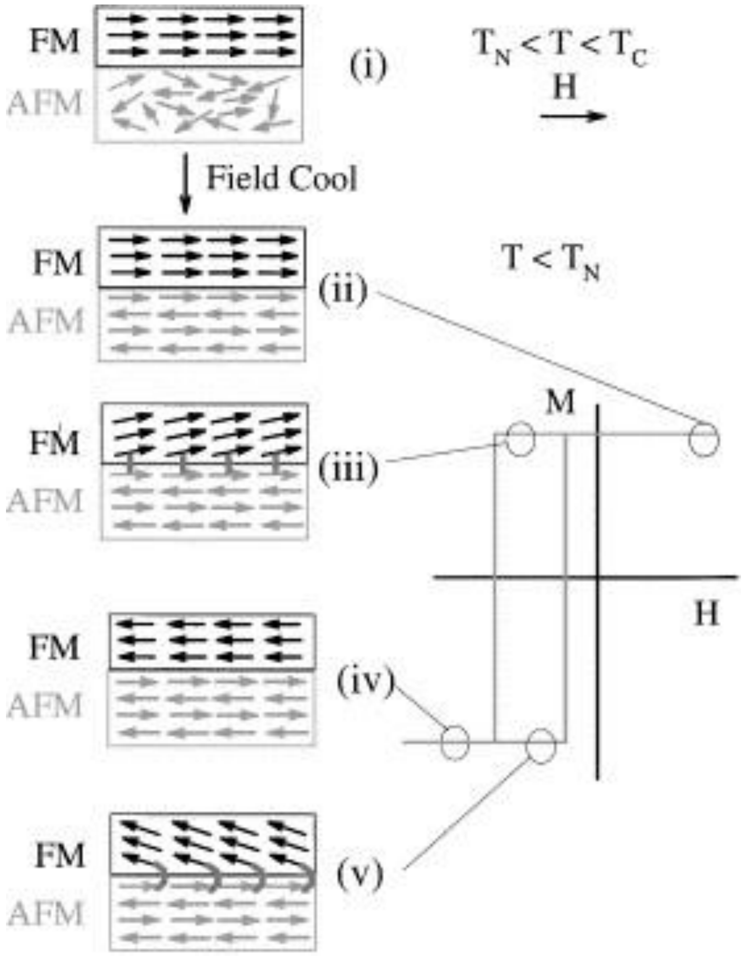

Figure 2.38 The schematic diagram of the spin configuration in an FM-AFM layered structure. The stages (i)-(v) represent the spins condition with magnetic field variation.[137]

Based on the shift of hysteresis loops of exchange bias effect, the conventional layered recording media can be built. As shown in Figure 2.39, this magnetoresistance recording media is composed of four layers materials, i.e. free FM, non-magnetic conductor layer, fixed FM and AFM layer. Because of the differences of the coercive field between free FM layer and fixed FM layer, the spins of these two FM layers can present parallel and anti-parallel states by changing the induced magnetic field and bring the composite with high magnetoresistance and low magnetoresistance states to obtain two logic sites for media recording.

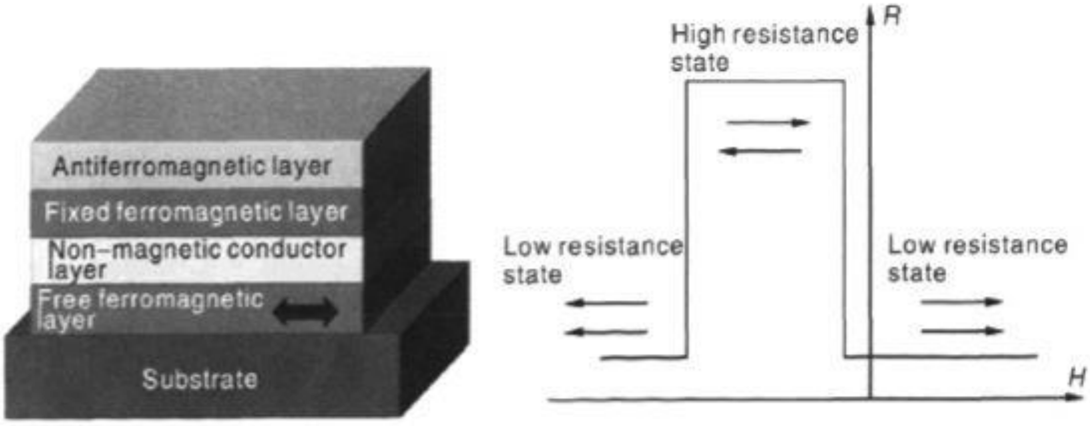

Figure 2.39 The structure magnetoresistance (MR) recording media (left) and its data storage mechanism.[139]

In order to mediate the magnetoresistance by electric field with low energy consumption, ferroelectric layer was introduced to AFM/FM heterostructure to form the AFM/FM/FE strain mediated ME structure. The high squareness magnetic hysteresis loops that origin from exchange bias and the electric tunability makes it the focus of fabricating the novel MRAM recording media.

With the developing understanding of memory media in recent years, Liu *et al.* reported a novel electric field control of exchange bias and 180° magnetization switching in AFM/FM/FE multiferroics heterostructure in 2011.[140] The multilayer film was composed by Ta (5 nm)/FeMn (15 nm)/$Ni_{80}Fe_{20}$ (2 nm)/FeGaB (14 nm)/Ta (20 nm). The film was deposited onto a single-crystal ferroelectric PZN-PT substrate. The FeGaB that occupies large magnetostriction constant of 70 ppm acts as the FM phase, and the FeMn film was deposited as the AFM phase. The inserted $Ni_{80}Fe_{20}$ between FeGaB and FeMn layer is to induce the strong exchange coupling between them. Because the piezoelectric anisotropic of PZN-PT and the FeGaB magnetization easy-axis can be modulated by in-situ magnetic bias field during film deposition to align as the same direction with the FE compression (d_{31}) or extension (d_{32}) direction,[141,142] it is realistic to build two configurations of ME heterostructure models that exhibit different E-field amplitudes and magnetic field angles dependence of magnetic hysteresis loops. As shown in Figure 2.40, the electric field is applied cross the thickness direction of PZN-PT substrate and the θ is the angle between external magnetic field and the magnetic easy axis. It could be found that the exchange bias can be modulated by the amplitude of applied E-field and the angle between easy-axis and external magnetic field.

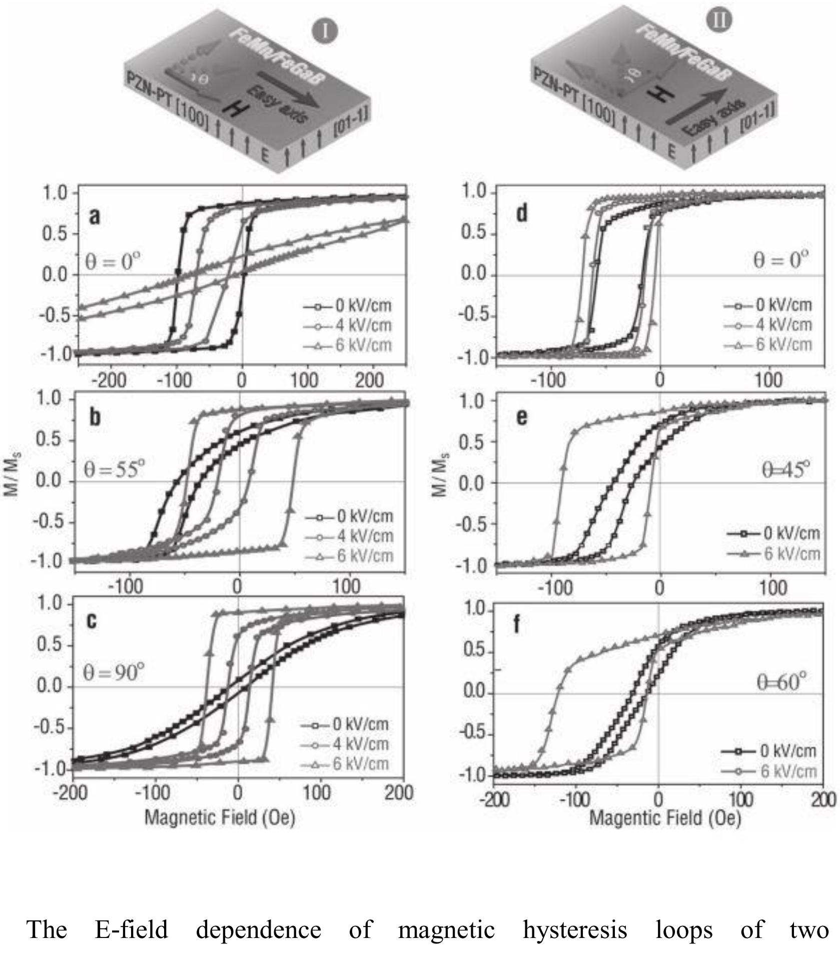

Figure 2.40 The E-field dependence of magnetic hysteresis loops of two configurations of FeMn/$Ni_{80}Fe_{20}$/FeGaB/ PZN-PT multiferroics heterostructure. (a) Configuration 1: FeGaB easy-axis along [100], the same as the d_{31} (-3000 pC/N) of PZN-PT and (b) configuration 2: FeGaB easy-axis along [01-1], the same as the d_{32} (1000 pC/N) of PZN-PT.[140]

Because the applied E-field is able to change the magnetic coercive field, which allows the magnetization switching very easily by changing the E-field, the continuously magnetization switching can be realized by applying a magnetic impulse to reverse the E-field induced magnetization switch back to the original magnetization value shown in Figure 2.41. The two stable reversible magnetization states provide this AFM/FM/FE heterostructure two corresponding magnetoresistance states, and the magnetoresistance state can be easily detected.

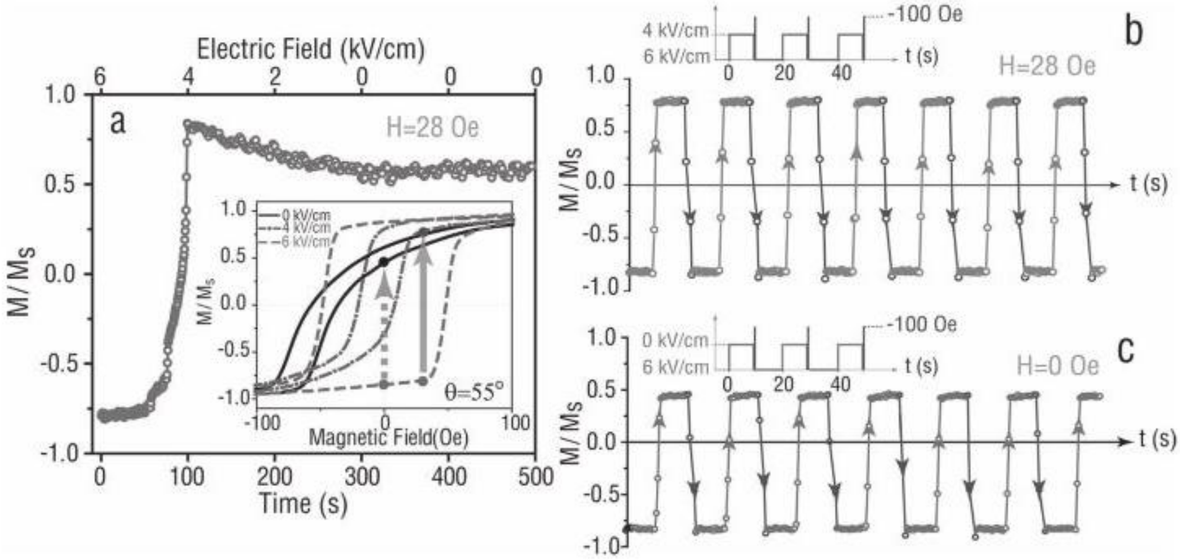

Figure 2.41 E-field induced switching of magnetization through E-field modulating exchange bias in AFM/FM/FE multiferroics heterostructure. (a) A 180° reversed magnetization could be found through changing E-field from 6 kV/cm to 4 kV/cm under 28 Oe magnetic bias field. The inset depicts the magnetization state transition with (solid arrow) and without (dash arrow) external magnetic bias field. (b) The magnetization is 180° reversible under a 100 Oe amplitude magnetic impulse with duration at 10 ms when the external magnetic bias field is 28 Oe and the two corresponding E-fields are 4 kV/cm and 6 kV/cm, respectively. (c) The incomplete magnetization reverse under a magnetic impulse with duration at 10 ms without the magnetic bias field and the two corresponding E-field are 0 kV/cm and 6 kV/cm, respectively.[140]

In 2015, Xue *et al.*[143] also reported an electric field induced reversible 180° magnetization multiferroics layered device which is composed of $Ni_{80}Fe_{20}$/NiCoO/glass/PZN-PT, with the magnetic easy axis along the [100] or [0$\bar{1}$1] PZN-PT crystal directions. The switching magnetization was from $0.76M_s$ to $-0.9M_s$ along PZN-PT [0-11] direction, shown in Figure 2.42.[143] The larger M/M_s ratio of NiFe/NiCoO/glass/PZN-PT provides it a higher magnetization stability to be compared with FeGaB system reported by Liu *et al.*[140]

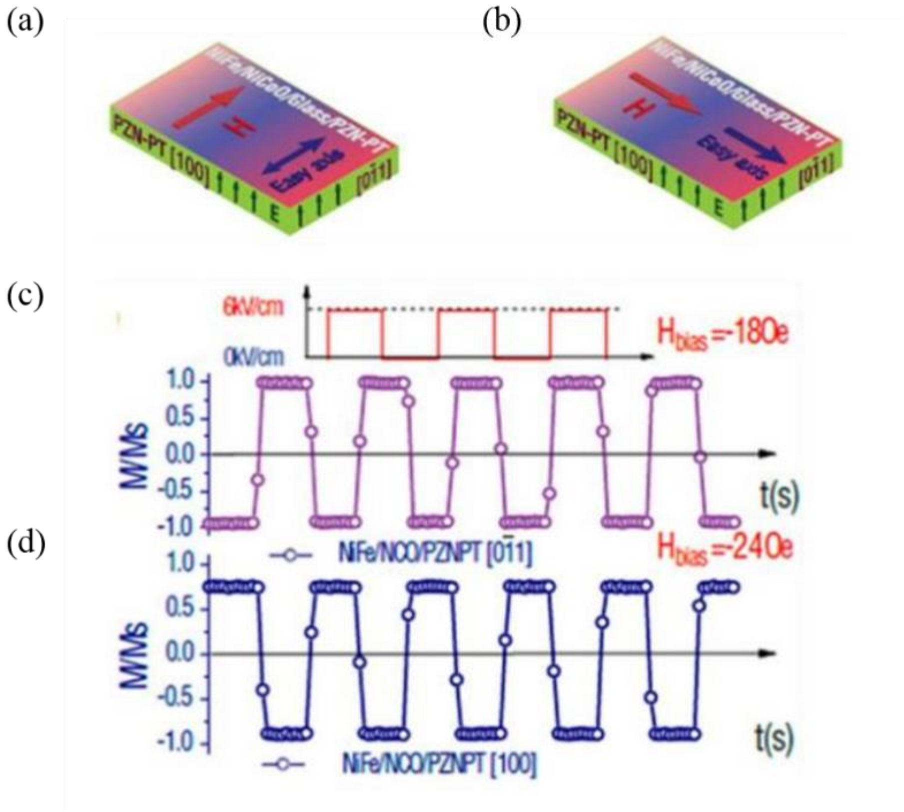

Figure 2.42 (a) Configuration 1: $Ni_{80}Fe_{20}$ easy-axis along [100], the same as the d_{31} (-3000 pC/N) of PZN-PT, and (b) configuration 2: $Ni_{80}Fe_{20}$ easy-axis along [0-11], the same as the d_{32} (1000 pC/N) of PZN-PT. (c) The E-field dependence of magnetization on configuration 1. The magnetization is near 180° reversible under two corresponding E-field of 0 kV/cm and 6 kV/cm, respectively, and the reversed magnetic field is 18 Oe. (d) The E-field dependence of magnetization on configuration 2. The magnetization is not 180° reversible under two corresponding E-field of 0 kV/cm and 6 kV/cm, respectively, and the reversed magnetic field is 18 Oe.[143]

2.5 The objectives of this thesis

In our studies, the researches mainly focus on three composition families, the objectives for each composition are not completely consistent with each other. The detailed objectives for:

(1) $Ba_2Bi_4Ti_5O_{18}$ (B2BT) and $Ba_2Bi_4Ti_{4.5}Mn_{0.5}O_{18}$ (B2BMT) ceramics

- To prepare the single phase ceramic of B2BT and B2BMT, which has never been reported before.
- To study the multiferroicity of $Ba_2Bi_4Ti_{4.5}Mn_{0.5}O_{18}$.
- To study the structure and dielectric/ferroelectric properties anisotropic of texturized B2BT.
- To make sure the structure of B2BT, for which has been disputed for long time. There are two main interpretations for most in most of the publications. Some studies regard it belongs to the B2cb space group, but the others thought it has I4/mmm space group.
- To investigate the correlation between frequency/temperature and dielectric/ferroelectric nature of B2BT.
- To study the mechanism of relaxation behavior of B2BT.

(2) $Na_{0.5}Bi_{0.5}Ti_{0.8}Mn_{0.2}O_3$ (BNT8M2) ceramic

- To prepare the single phase ceramic of BNT8M2.
- To investigate the morphology and structure of BNT8M2.
- To study the correlation between frequencies/temperature and dielectric/ferroelectric

properties of BNT8M2.

- To study the magnetic nature and transition point by temperature dependence M-H loops and ZFC-FC data.

- To check the magneto-electric coupling effect through piezoforce microscope (PFM).

- To simulate the origin of magnetic properties.

(3) $0.5(0.94Bi_{0.5}Na_{0.5}TiO_3$-$0.06BaTiO_3)$-$0.5BiFe_{0.8}Mn_{0.2}O_3$ (NBTB-BF8M2O) ceramic

- To synthesis the single phase BNTB-BF8M2O ceramic
- To modify the antiferromagnetic nature of pure BiFeO3 (BFO) to ferromagnetic nature of NBTB-BF82O.

- To create the large remnant ferroelectric polarization and small coercive electric field.

- To create the magneto-electric coupling effect under room temperature, and to characterize this effect by PFM observation.

- To analyze the ferroelectric to paraelectric transition point and ferromagnetic to paramagnetic transition point by ZFC and FC data.

- To simulate the origin of magnetic properties.

Chapter III Methodologies

The methodologies are composed by three parts, they are sample preparations, characterizations and calculations. The details were shown in the following sections. In this study, three types of different compositions were prepared and characterized, they are: (1) $Ba_2Bi_4Ti_5O_{18}/Ba_2Bi_4Ti_{5-x}Mn_xO_{18}$,

(2)$Na_{0.5}Bi_{0.5}Ti_{0.8}Mn_{0.2}O_3$

(3)$x(0.94Bi_{0.5}Na_{0.5}TiO_3-0.06BaTiO_3)-(1-x)BiFe_{(1-y)}Mn_yO_3$.

3.1 Samples preparations

the ceramic samples are prepared by three main steps, they are (1) 1st high energy planetary ball milling; (2) powders calcination; (3) 2nd high energy planetary ball milling (4) disks sintering. The main procedures were shown by Figure 3.1. For the step by step powder calcination procedures, the additional ball milling would be introduced between each calcination step, such as the powder calcination of $Ba_2Bi_4Ti_5O_{18}/Ba_2Bi_4Ti_{5-x}Mn_xO_{18}$ and $0.5(0.94Bi_{0.5}Na_{0.5}TiO_3-0.06BaTiO_3)-0.5BiFe_{0.8}Mn_{0.2}O_3$.

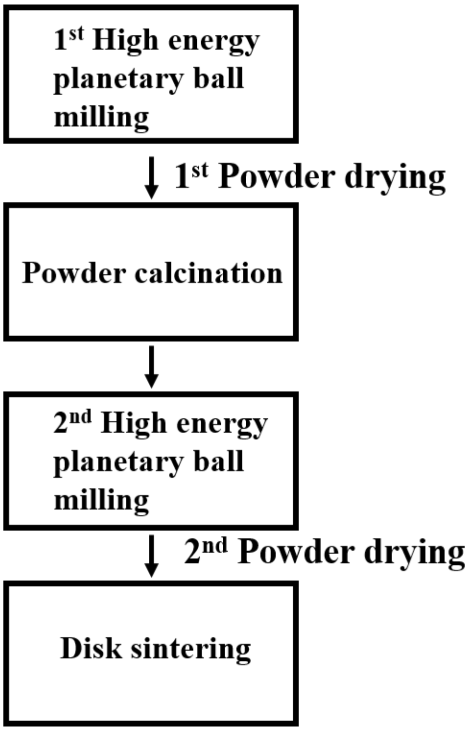

Figure 3.1 The main procedure for ceramic samples preparations.

(1) Sample preparation for $Ba_2Bi_4Ti_5O_{18}$/$Ba_2Bi_4Ti_{5-x}Mn_xO_{18}$:

The $Ba_2Bi_4Ti_5O_{18}$ powder was prepared by the conventional solid-state reaction route. Bi_2O_3 (99.9 %, Sigma-Aldrich), TiO_2 (99.8 %, Sigma-Aldrich) and $BaCO_3$ (99.8 %, Sigma-Aldrich) were used as starting materials. The stoichiometric mixture of raw powders was thoroughly mixed for 24 h in a planetary ball mill (QM-3SP4, Nanjing University Instrument Plant, China, 350 r/min), and then calcined for 24 h at 850 °C, 1000 °C and 1100 °C for 24 h, respectively. Between each independent calcination step the calcined powder was reground for 24 h. However, for the $Ba_2Bi_4Ti_{5-x}Mn_xO_{18}$, since the Mn doping affected the calcination temperature and result to easily over calcined behaviour. We attempted the final step calcined temperature of 1025 °C, 1050 °C and 1075 °C. But consequently, no single phase ceramics were produced. Therefore, no further sintering can be done on the Mn doped samples.

The textured ceramics of $Ba_2Bi_4Ti_5O_{18}$ were sintered by a two-step method[6] using a SPS furnace (HPD 25/1 FCT, SPS furnace, Germany). In the first step, the powders were sintered in a graphite die (20 mm diameter) under a pressure of 80 MPa at 1000 °C for 3 mins. In the second step, the sintered ceramic was placed into a graphite die of 30 mm in diameter and then sintered at 1050 °C for 5 mins under a pressure of 80 MPa. During the second sintering stage, the grain growth rate along the *a- and/or b*-axis was faster than that along the *c*-axis, resulting in the grains with the *c*-axis of aligned along the applied pressure direction. A heating rate of 100 °C/min was employed in both sintering stages. Finally, the spark plasma processed (SPSed) disks were annealed at 880 °C for 6 h in air to remove any residual carbon. The colour of the annealed disk was light yellow with translucent feature. The density of the disks, as measured by the Archimedes method, was 97.6 %. For the microstructure observation and electrical property characterization, the textured ceramics were cut perpendicular and parallel to the hot-pressing direction.

The $Ba_2Bi_4Ti_{4.5}Mn_{0.5}O_{18}$ powder was prepared by the conventional solid-state reaction route. Bi_2O_3 (99.9 %, Sigma-Aldrich), TiO_2 (99.8 %, Sigma-Aldrich) and $BaCO_3$ (99.8 %, Sigma-Aldrich), MnO_2 (99 %, Sigma-Aldrich) were used as starting materials. The stoichiometric mixture of raw powders was thoroughly mixed for 24 h in a planetary ball mill (QM-3SP4, Nanjing University Instrument Plant, China), based on the synthesis condition of pure $Ba_2Bi_4Ti_5O_{18}$, the calcination procedure of $Ba_2Bi_4Ti_{4.5}Mn_{0.5}O_{18}$ was kept as the same, which were 24 h at 850 °C, 24 h at 1000 °C, 24 h at 1100 °C, respectively. Between each independent calcination step the calcined powder was reground for 24 h. However, the final product was found seriously over-calcined after 1100 °C calcination. Hence, the final calcination was set under lower temperature, we tried three different value which are 1025 °C, 1050 °C and 1075 °C, respectively. And the final achieved powder was all inspected by X-ray diffraction to reveal its phase conditions.

(2) Sample preparation for $Na_{0.5}Bi_{0.5}Ti_{0.8}Mn_{0.2}O_3$ with Nb doping:

Pure $Na_{0.5}Bi_{0.5}Ti_{0.8}Mn_{0.2}O_3$ and $Na_{0.5}Bi_{0.5}Ti_{0.8}Mn_{0.2}O_3$ with 2 mol. % Nb additives samples were prepared by solid state calcination method. Bi_2O_3 (99.9 %), TiO_2 (99.8 %), Na_2CO_3 (99.6 %), MnO_2 (99 %) (all from Sigma-Aldrich) were used as starting materials. These raw powders were weighed in the stoichiometric composition and then thoroughly ball milled by planetary machine (QM-3SP4, Nanjing University Instrument Plant, China, 350 r/min) for 24 h by ZrO_2 balls in polypropylene containers with ethanol and the slurry was then dried on the hot plate to acquire the dry powder. The powder was then calcined at 800 ºC for 2 h then 850 ºC for 2 h. The calcinations were then ball milled for 4 h to obtain the homogeneous slurry. The slurry was then dried by hot plate to get the final powder. The Nb_2O_5 (99.9%, Sigma-Aldrich) was added and mixed by mortar when the calcination was finished. Then the powder was mixed with binder (5 wt% polyvinyl alcohol) by mortar and then cold-pressed uniaxial into pellets by 12 mm diameter mould, the pellets were all solid state sintered under 1050 ºC and covered by ZrO_2 powder to prevent the volatilization of Na and Bi. The temperature increasing rate for all the calcination and sintering procedures is 5 ºC/min. The dry procedure was all spent 12 h under 120 ºC on hot plate.

(3) Sample preparation for $0.5(0.94Bi_{0.5}Na_{0.5}TiO_3\text{-}0.06BaTiO_3)\text{-}0.5BiFe_{0.8}Mn_{0.2}O_3$

Samples were prepared by solid state calcination method. Bi_2O_3 (99.9 %), TiO_2 (99.8 %), Na_2CO_3 (99.6 %), MnO_2 (99 %), $BaCO_3$ (99.8 %), Fe_2O_3 (99.945 %) (all from Sigma-Aldrich) were used as starting materials. These raw powders were weighed in the stoichiometric composition and then thoroughly ball milled by planetary machine (QM-3SP4, Nanjing University Instrument Plant, China, 350 r/min) for 24 h by ZrO_2 balls in polypropylene containers with ethanol and the slurry was then dried on the hot plate to acquire the dry powder. The powder was then firstly calcined by a two stages process in one calcination which is 850 ºC for 2 h then 900 ºC for 4 h, followed by re-mill the calcined powder for 24 h, then the powders were further calcined under the other two stages process of 950 ºC for 4 h and then 1000 ºC for 2 h. The calcinations were then ball milled for 4 h to obtain the homogeneous slurry. The slurry was then dried by hot plate to get the final powder. Then the powder was mixed with binder (5 wt% polyvinyl alcohol) by mortar and then cold-pressed uniaxial into pellets by 12 mm diameter mould, the pellets were all solid state sintered under 1000 ºC and covered by ZrO_2 powder to prevent the volatilization of Na and Bi. The temperature increasing rate were kept same as $Na_{0.5}Bi_{0.5}Ti_{0.8}Mn_{0.2}O_3$ calcination at 5 ºC/min. And the dry procedure was all spent 12 h under 120 ºC on hot plate.

3.1.1 High energy planetary ball milling

The first step of sample preparation is high energy planetary ball milling. This step start from place the raw powders as calculated stoichiometric ratio into the ball milling containers. The containers were then fixed onto the planetary disk of planetary balling machine. The high energy impact between raw powders and milling balls that created by conversed rotation between planetary disk and containers could smash the raw powder into micro particles. The basic rotation conditions were shown by Figure 3.2.

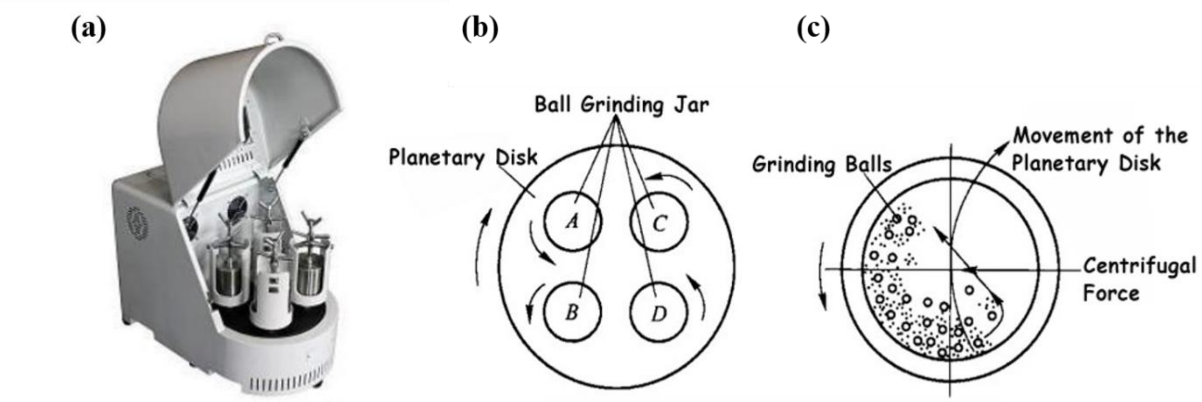

Figure 3.2 Principle of high energy planetary ball milling. (a) The appearance of planetary ball milling machine. (b) The rotation relations between planetary disc and four ball milling containers. (c) The rotation condition between grinding balls, raw powders and planetary disk during ball milling. (https://deco-mill.en.alibaba.com/product/60006372559222012965/Nano_Milling_Machine_Nano_Powder_Grinding_Equipment_Lab_Planetary_Ball_Mills.html)

The rotation speed and milling duration were all adjusted to a proper value for different compositions after vast number of trials. Since the rotation velocity difference between planetary and milling containers would affect the impact intensity of the balls which contributes to the energy input to the powder charge.[144] The type of ball milling machine in this study is QM-3SP4, Nanjing University Instrument Plant, China. We adopted milling balls made by ZrO_2 with the mass ratio of $M_{powders} : M_{balls} = 1 : 2$.

3.1.2 Powder calcination

Powder synthesis is a step where the chemical reactions take place between the constituents resulting in the desire phase. There are many types of methods for powder synthesis, including conventional solid state calcination method, chemical precipitation method, sol-gel method, hydrothermal method, et al,. The method using in this study is the conventional solid state calcination method. Proper calcinations at the right temperature (below the melting point of constituents) and atmosphere (oxydic/reductive/inert atomosphere) are necessary to obtain the final product with good properties. Using the preparation of $BaTiO_3$ as an example, the calcination could be described by the formula below:

$$BaCO_3 + TiO_2 \longrightarrow BaTiO_3 + CO_2\uparrow \tag{3.1}$$

The calcination normally take place at 1200 °C - 1400 °C in air atmosphere. The particle size could be adjusted by tuning the calcination temperature. The chemical reactions in our studies are similar with formula (3.1), almost all of the sub-reaction were proceed under proper temperature and atmosphere. The starting materials are oxidation and carbonate compounds.

3.1.3 Solid state sintering

Solid state sintering is a processing technique to produce density-controlled materials and components from metal or/and ceramic powders by applying thermal energy.[145] The ceramic sintering and densification is generally composed by four basic steps: (1) Physical contact between ceramic particles driven by applying pressure on pre-sintering samples. (2) The formation of concave sintering necks between adjacent particles, which enhance the touching surface between particles. (3) Evolution and diffusion of grain boundaries and sintering necks. (4) The pores were eliminated and isolated finally. The procedures are shown by Figure 3.3.[146] Solid state sintering for ceramic normally happen in box furnace or tube furnace without applied pressure during process. Moreover, the sintering can also occur within highly controlled atmosphere through injecting different type of oxydic, reductive or inert gas.

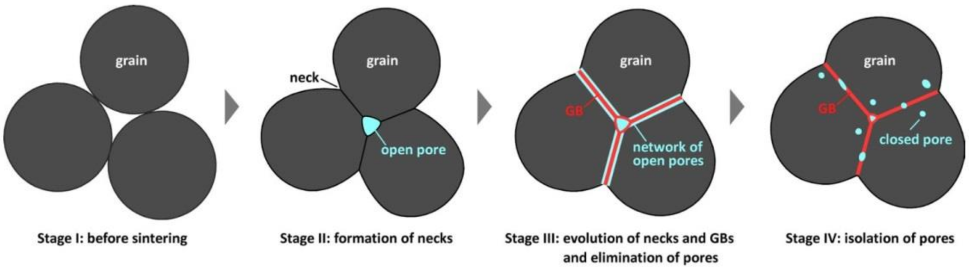

Figure 3.3 The solid state sintering procedure of ceramics.[146]

3.1.4 Spark plasma sintering (SPS)

Spark plasma sintering is a field-assisted sintering technology (FAST) that sintering occurs under low voltage, direct pulsed current, high heating rate and pressure applied condition. It has already been applied on many types of materials processing in recent years.[147] The applied pressure allows homogeneous subsequent densification and limited grain growth. The high-heating rate benefits to enhance densification due to retarding grain size coarsening.[147-149] The basic working principle of SPS device is shown by Figure 3.4. The raw powders for sintering are placed into the graphite die and the pressure is applied by the punch for densification purpose. Furthermore, during sintering, a DC pulse current is also applied on the sample for leading the Joul heating. The heat can effectively transferred to the sample to further decrease the sintering temperature and increase the density of ceramics.[147]

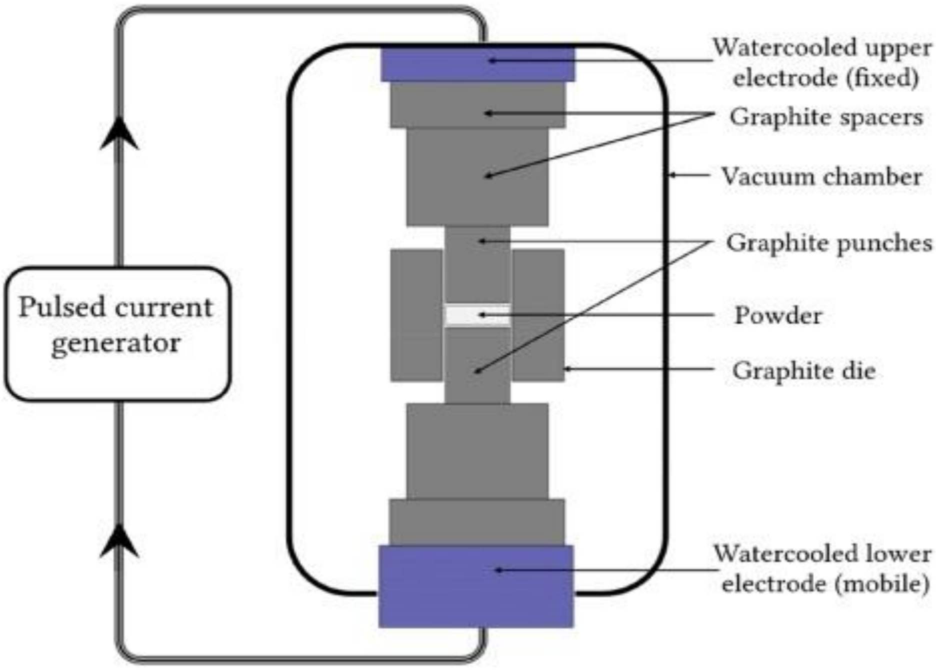

Figure 3.4 The basic working principle of SPS.[150]

The texture of bismuth-layered structure ferroelectric (BLSF) in this work was done by SPS, the procedure is described by Figure 3.5, in the first step, the sintering happened in a ϕ20 mm graphite die with 50 MPa pressure to densify ceramics into disk for minimize the grain growth. In the second step, the disk that prepared by 1st step was texturized by a bigger graphite die of ϕ30 mm with higher pressure at 80 MPa. The mechanism of texture is that the grain growth easy axis would prefer to along the direction without pressure, which results to the orientation grain growth. The basic processes schematic for texture are illustrated by Figure 3.5.

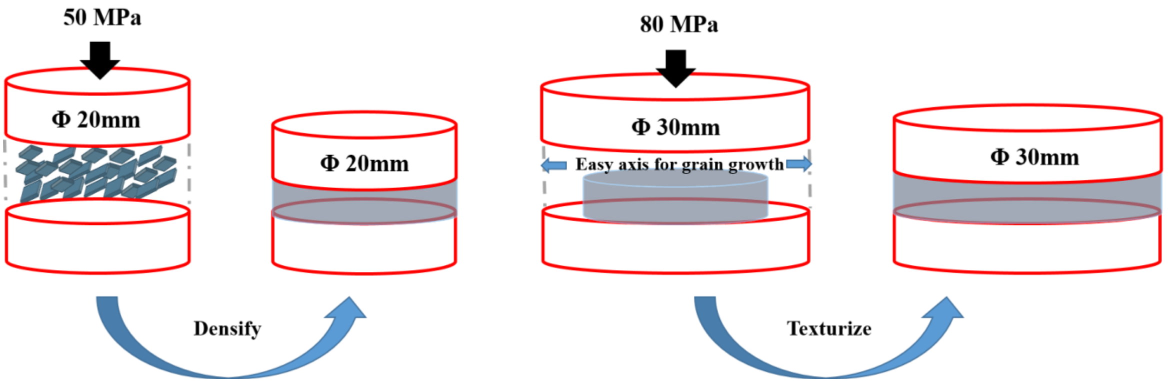

Figure 3.5 The basic process of ceramic texturized by SPS.

3.2 Characterizations

3.2.1 Crystallographic structure characterization

X-ray diffraction (XRD) is an effective and scientific technique primarily used for crystallographic structure characterization. The obtainable information from XRD can be used for:[151]

1) Qualitative analysis.

2) Quantitative analysis.

3) Unit cell lattice parameter calculation.

4) Crystallite size and strain calculation.

The X-rays are generated from a cathode ray tube, and the X-ray that incident to the sample produces constructive interference when conditions satisfy with Bragg's law:[152]

$$n\lambda=2d\sin\theta \tag{3.2}$$

where n is the order of reflection, λ is the wavelength of x-rays, d is the characteristic spacing between adjacent crystal planes. And θ is the angle between the normal of crystal plane and the incident beam.

The basic Bragg's law of XRD is shown by Figure 3.6. The equation can be described as the path difference is multiple of the X-ray wavelength. Because the used X-ray wavelength is known. The distance between the crystal planes can be determined by only measuring the incidence angle of X-ray,

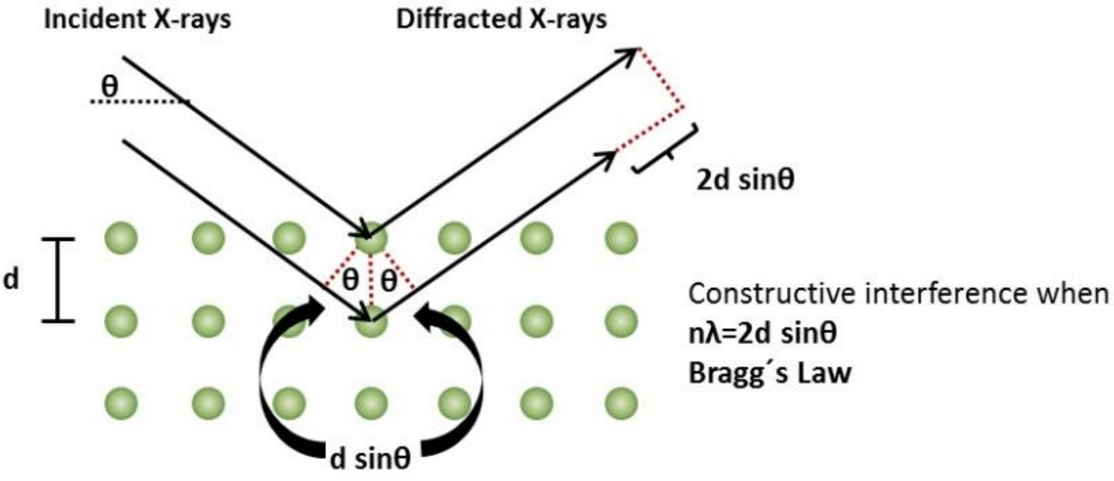

Figure 3.6 The basic schematic of Bragg's law of XRD (https://wiki.anton-paar.com/en/x-ray-diffraction-xrd/).

The phase were monitored via XRD for both the calcined powders and the crushed sintered samples. The step size of the scan was always 0.02°/2θ. The scanning speed was 0.033 2θ/s ranging from 10° to 80° and 0.008° 2θ/s for 2θ ranging from 27° to 34°, respectively.

3.2.2 Crystal and domain microstructure characterization

(i) Scanning electron microscopy (SEM)

The crystal microstructure is observed by using scanning electron microscopy (FEI Inspect-F, Hillsboro, OR, USA). Commonly, the break-off cross section or pre-polished-surface were all satisfied with the scanning conditions. In order to reveal the grain boundaries clearly, the sample should be thermal-etched in the calcination corresponding atmosphere and temperature (100-150 ºC below sintering temperature) for 10-20 mins. And the sample should be coating with gold or carbon to generate the conductive surface.

(ii) Piezoresponse force microscopy (PFM)

The PFM is based on the piezoelectric effect that exhibit strong coupling between the displacement change of ferroelectric sample's surface and applied electric field. The displacement of sample can be monitored by probe oscillation and then amplified by using a lock-in amplifier. The principle of piezoelectric effect happens on out-of-plane (d_{33}) and in-plane (d_{15}) and then couple back to probe, which is illustrated by Figure 3.7. Figure 3.7 (a) and (b) describe the electric field applied parallel and antiparallel to the spontaneous polarization and leads to vertical and horizontal movement. Figure 3.7(c) and (d) illustrate the electric field applied perpendicular to the polarization and results in shear movement. The corresponding signal change of incidence laser spot on probe would be monitored and then output piezo response signal that composed by amplitude and phase signal. These signals are presented as the position change of red circle in Figure 3.7. These characteristics allow PFM to detect the ferroelectric domain micro-structure and switching. The model of PFM be used for this work is NT-MDT (Ntegra systems).

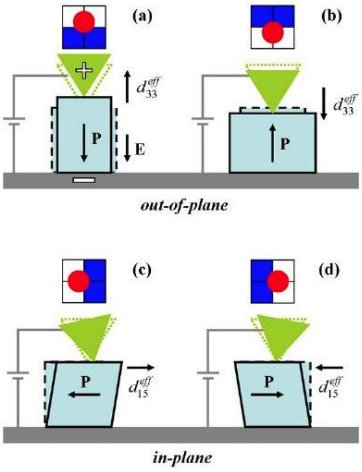

Figure 3.7 Schematic of PFM working principle based on piezoelectric effect. (a-b) Electric field applied parallel and antiparallel to the spontaneous polarization leads to the vertical and horizontal displacement of samples. (c-d) Electric field applied perpendicular to the polarization results in shear displacement of samples. The corresponding signal change of incidence laser spot on probe would be monitored and output piezo response signal that composed by amplitude and phase signal.(https://www.azonano.com/article.aspx?ArticleID=2682)

The pellets for PFM observation were all polished to the criterion that same as the SEM observation and thermal-etched in the calcination corresponding atmosphere and temperature (100-150 ºC below sintering temperature) for 10-20 mins. The Pt tips (HQ: HSC14/Pt) using in this study all provided by *umasch* company with the resonance frequency at 160 kHz and stiffness factor of 5.0 N/m.

3.2.3 Dielectric properties measurements

The sample for dielectric properties measurement were all cut into small square disks. And the disks were all coated with silver paste. The temperature and frequency dependencies of the relative dielectric permittivity and loss tangent were measured by an LCR meter (Agilent, 4284A, USA) connected to a purpose-designed furnace (25 ºC to 600 ºC) or a low temperature test container (-195 ºC to 150 ºC). The polarization-electric field (*P*-*E*) and current-electric field (*I*-*E*) loops were measured by a ferroelectric measurement instrument (NPL, UK). The testing frequency of a triangular voltage waveform for both the *P*-*E* and *I*-*E* loops were 10 Hz for the two fully completed cycles.

The piezoelectric constant, d_{33}, was measured using a Berlincourt piezo d_{33} meter (ZJ-3B, Institute of Acoustics, Chinese Academic of Science, Beijing).

3.2.4 Magnetic properties measurements

The magnetic properties were measured by superconducting quantum interference device (SQUID). SQUID is an extremely sensitive magnetometer used for measuring subtle magnetic fields, its most key parts is the superconducting loop which working principle based on Josephson junctions, shown by Figure 3.8. The loop is composed by two types of materials, the superconductor ring (brown parts) and isolator layers (black parts). During magnetic field detection, a DC bias current is applied on the superconductor, when the current value is above the threshold, the isolator layer turns into the conductor and permit the current flow through and simultaneously emit out the photon. Meanwhile, the electromagnetic wave is produced. When the external magnetic flux effect on the superconducting loop, the induced cycling current in superconducting loop will change simultaneously based on Lenz's law to make the net magnetic flux minimum. Therefore, this induced current will change the phase angle of the magnetoelectric wave that produced by DC bias current. By detecting the electromagnetic wave phase angle change, the magnetic flux strength can therefore be indirectly detected. Since the Josephson effect works under quantum scale, the superconducting quantum interference device (SQUID) can be used for the high sensitive magnetometers.[153] The magnetic properties measurements including temperature dependence *M*-*H* loop, zero field cooling and field cooling (ZFC-FC) in this study, which were all done by SQUID detector based on Josephson effect.

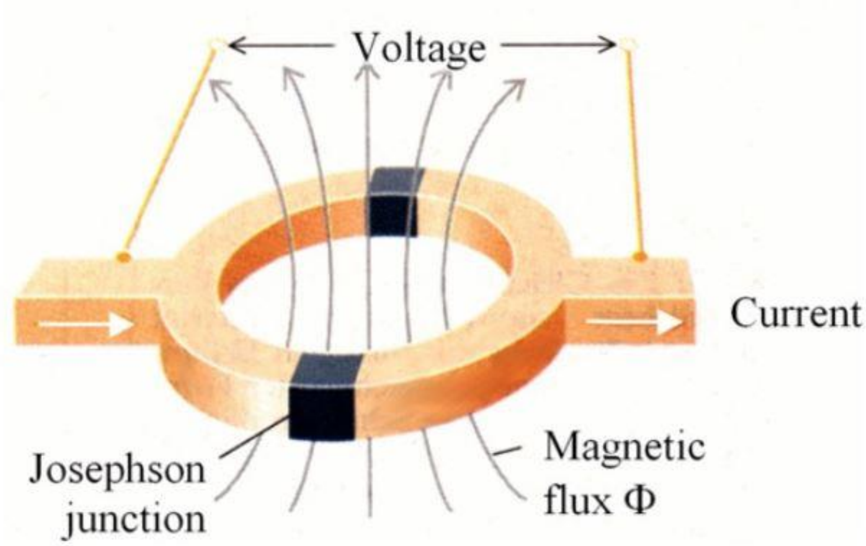

Figure 3.8 Schematic of superconducting loop that containing Josephson junctions. The loop is composed by a superconductor ring (brown parts) separated by thin isolating layers (black parts). (http://www.sjsu.edu/people/raymond.kwok/courses/physics/phys120s-lab/squid/)

The zero-field cooling/field cooling (ZFC-FC) and magnetic (M–H) hysteresis loops were measured using a superconducting quantum interference device magnetometer (Quantum design, model MPMS (SQUID) VSM, USA) in the magnetic field range -2 T to 2 T under the corresponding temperature range. The M–T curves were corrected for a paramagnetic contribution of individual magnetic atoms with no magnetic interaction.

3.2.5 X-ray photoelectron spectroscopy

The X-ray photoelectron spectroscopy (XPS) data were acquired using a bespoke ultra-high vacuum system fitted with a Specs GmbH Focus 500 monochromated Al Kα X-ray source, Specs GmbH Phoibos 150 mm mean radius hemispherical analyser with 9-channeltron detection, and a Specs GmbH FG20 charge neutralising electron gun. Survey spectra were acquired over the binding energy range 1100 – 0 eV using a pass energy of 50 eV and high resolution scans were made over the C 1s, O 1s, Ba 3d, Ta 2p and Sr 3d lines using a pass energy of 15 eV with the medium area lens mode, 7 mm diameter input aperture and 30 mm diameter lens iris. Under these conditions the full width at half maximum of the Ag $3d_{5/2}$ reference line is ~0.7 eV. In each case, the analysis was an area-average over a region approximately 2 mm in diameter on the sample surface. The energy scale of the instrument is calibrated according to ISO standard 15472, and the intensity scale is calibrated using an in-house method traceable to the UK National Physical Laboratory. Data were quantified using Scofield cross section corrected for the energy dependencies of the electron attenuation lengths and the instrument transmission. Data interpretation was carried out using CasaXPS software v2.3.16.

Chapter IV Investigation of Aurivillius $Ba_2Bi_4Ti_5O_{18}$ and $Ba_2Bi_4Ti_{4.5}Mn_{0.5}O_{18}$ ceramics

4.1 Crystal structure and electrical properties of textured $Ba_2Bi_4Ti_5O_{18}$ ceramics

4.1.1 Introduction

Bismuth layer-structured ferroelectrics (BLSFs) with the general formula $(Bi_2O_2)^{2+}(A_{m-1}B_mO_{3m+1})^{2-}$ can be described as the regular stacking of $[Bi_2O_2]^{2+}$ layers and pseudo-perovskite $(A_{m-1}B_mO_{3m+1})^{2-}$ slabs, where m denotes the number of sheets of corner-sharing BO_6 octahedra. The 12-coordinated A-site can be occupied by mono-, di-, or trivalent metallic cations, while the octahedral-coordinated B-sites are entered by tetra-, penta-, or hexavalent metallic cations. The origin of ferroelectricity in BLSFs is attributed to the displacement of the A- and/or B-site cations in the perovskite blocks with cooperative tilting of the BO_6 octahedra.[89,90] The offset of polarization between each BO_6 layer on *c*-axis only permits non-zero net polarization appears along *c*-axis when the number of BO_6 layer is odd in BLSF, which makes the vast majority of ferroelectricity of BLSF almost appears only on *a* (*b*)-axis.[90,91] In compounds with an even number of octahedral layers ($m = 2n$, where n is an integer), the spontaneous polarization is formed along the *a*-axis direction. The odd layer compounds ($m = 2n+1$) exhibits the polarization in the *a*-*c* plane (the major component in the [100] direction).[90]

BLSFs have received increasing attention due to their high Curie point (T_c), which makes them attractive for high-temperature piezoelectric devices.[93,154,155] These materials are also promising candidates for nonvolatile ferroelectric random-access memories due to their large polarizations and fatigue-free properties.[1,156] Moreover, BLSFs can be used for oxide-ion conductors[157] and photocatalysts[158]. Some of them also exhibit mutliferroic properties[159] and relaxor behaviour.[12]

If compared to normal ferroelectrics, relaxor ferroelectrics (RFEs) are much more attractive for piezoelectric transducer and actuator applications due to their high dielectric permittivity and large electromechanical constants.[160] RFEs exhibit a broad, frequency-dependent, dielectric anomaly at the temperature of the maximum of the relative dielectric permittivity (T_m). Most of the current research on RFEs is focused on lead-based complex perovskites, such as $Pb(Mg_{1/3}Nb_{2/3})O_3$-$PbTiO_3$ and $Pb(Zn_{1/3}Nb_{2/3})O_3$-$PbTiO_3$. However, relatively low T_c or T_m temperatures of these relaxor systems restrict their high-temperature applications. Therefore, there is a great effort in developing new lead-free RFE materials for the efficient conversion of electrical energy to mechanical, and vice versa, at high temperatures. Within the BLSFs family, only a limited number of compounds, such as $BaBi_2Nb_2O_9$, $BaBi_2Ta_2O_9$, $BaBi_4Ti_4O_{15}$ etc., show relaxor behavior.[161-163] The RFE behavior in these systems is attributed to the positional static disorder between Bi^{3+} and Ba^{2+} cations, which is associated with fluctuations in composition.[164] However, compared with above conventional lead-based RFE, the studies and understanding on the RFE behavior of BLSFs system are extremely limited.

$Ba_2Bi_4Ti_5O_{18}$ (B2BT) belongs to the family of BLSFs that exhibit relaxor characteristics. The Ba and Bi ions occupy the A-sites and the Ti ions enter the B-sites of the pseudo-perovskite blocks $(A_{m-1}B_mO_{3m+1})^{2-}$. The synthesis and ferroelectric properties of B2BT were first reported by Aurivillius and Subbarao in 1962.[165,166] However, the existence of single phase in B2BT is still disputable. While Subbarao reported a mixture of a four-layer oxide $BaBi_4Ti_4O_{15}$ and $BaTiO_3$ in the B2BT ceramics synthesized via solid state reaction[18],Aurivillius found only a single tetragonal phase (SG: *I4/mmm*) in B2BT single crystal[165] However, the existence of an exclusive non-polar structure in the B2BT single crystal precludes the observation of the ferroelectric hysteresis loops. Moreover, Aurivillius observed a maximum of the dielectric permittivity, typical of a displacive ferroelectric transition, at 329 °C. Irie *et al*. have reported that the B2BT crystal adopts an orthorhombic *B2ab* structure.[89,91] They measured the polarization vs. electric field (*P*-*E*) loops of the B2BT single crystal in different crystallographic directions and found that the saturated remnant polarization (P_r) shows non-zero values along both the *a*-axis (or *b*-axis) and the *c*-axis. On the other hand, P_r (~ 8.5 mC/m^2) measured along the *c*-axis does not comply with the symmetry conditions of the space group *B2ab*. The frequency dependence of the maximum relative dielectric permittivity ($\varepsilon_{r\,\mathrm{max}}$) was observed along both the *a*- or *b*-axis and the *c*-axis, which indicates the RFE behaviour of the B2BT single crystal. Based on high-resolution powder neutron diffraction data, Ismunandar demonstrated that the crystal structure of B2BT is orthorhombic with space group *B2eb* (an alternative setting of *B2ab*)[167]. Lightfoot *et al.*[168] employed high-resolution powder neutron diffraction and Fuentes *et al.*[169] used Synchrotron x-ray diffraction to study the precise structure of B2BT, but they all did not obtain deterministic conclusions. Hou *et al.*[170] have observed a very broad frequency independent dielectric anomaly in B2BT ceramics at about 330 °C, extending from 10 kHz to 1 MHz. Dubey *et al.*[171] have synthesized the B2BT powder by a solution combustion route. The sintered B2BT had an orthorhombic symmetry (*B2cb*) and exhibited a diffuse phase transition at about 350 °C. The transition temperature of the B2BT ceramic was slightly frequency sensitive. Obviously, compared to the conventional BLSFs with $m = 2, 3$, there are rare reports about the $m = 5$ group. In addition, the current understanding of both the crystal structure and electrical properties of B2BT ceramic is inconsistent, containing controversial issues.

Single crystals are considered as the most suitable materials for studying the RFE behaviour, as they enable to evaluate variations in the electrical response of a relaxor with respect to the different crystal axes. However, fabrication of single crystals is difficult and costly. The structural grains in sintered ceramics are usually randomly orientated, so that the measured properties correspond to the average value over each grain. The textured ceramics exhibit a single crystal-like nature in terms of the orientation of crystal axes, and thus offer enhanced electrical properties.[6, 12] Textured BLSFs ceramics can be produced by the templated grain growth method and spark plasma sintering (SPS) technique.[172-174] So far, there have been published only a few studies on the processing and electrical properties of the textured BLSF relaxor-type ceramics. Yan *et al.* and Karthik *et al.* have both investigated the effect of texture on the electrical properties of the $BaBi_2Nb_2O_9$ ceramic.[161,175] Both these studies revealed that the dielectric permittivity of the material exhibits a high anisotropy. The dielectric permittivity along the direction perpendicular to the pressing direction was much higher than that in the direction parallel to the pressing direction. Duran-Martin *et al.* fabricated the textured $Bi_{1.75}Te_{0.25}Sr_{0.75}Na_{0.25}Nb_2O_9$ ceramics by hot press sintering.[176] From the dielectric and ferroelectric property measurements, they suggested the existence of the RFE state in the prepared material.

Apparently, in spite of tremendous effort over several decades, there is no general understanding on both the crystal structure and electrical (dielectric, ferroelectric and piezoelectric) properties of the B2BT ceramics. To our best knowledge, this is the first report about processing, microstructure and electric properties of the textured B2BT ceramics. We prepared the grain-oriented ceramic samples of B2BT by the SPS technique. The crystal structure, dielectric, ferroelectric, and piezoelectric properties of the ceramics were systemically investigated in the parallel and perpendicular direction to the direction of SPS hot-pressing.

4.1.2 Characterizations

Crystal structure determination and refinements

The Rietveld refinement was performed on the XRD data obtained for powders, as ground from the textured ceramics. The GSAS software was used for Rietveld refinement.[177]

Microstructural characterization

The samples for SEM analysis were thermally etched at 1100 °C for 15 mins in order to reveal structural grains.

Electrical property characterization

An anisotropy in electrical properties of the SPSed samples was tested by applying an external electric field in the perpendicular [⊥] and parallel [||] direction to the SPS hot-pressing direction. The polarization-electric field (*P*-*E*) and current-electric field (*I*-*E*) loops were measured by a ferroelectric measurement instrument. [30] The testing frequency of a triangular voltage waveform for both the *P*-*E* and *I*-*E* loops were 10 Hz for the two fully completed cycles. The piezoelectric constant, d_{33}, was measured using a Berlincourt piezo d_{33}.

4.1.3 Results and discussions

B2BT crystal structure characterization

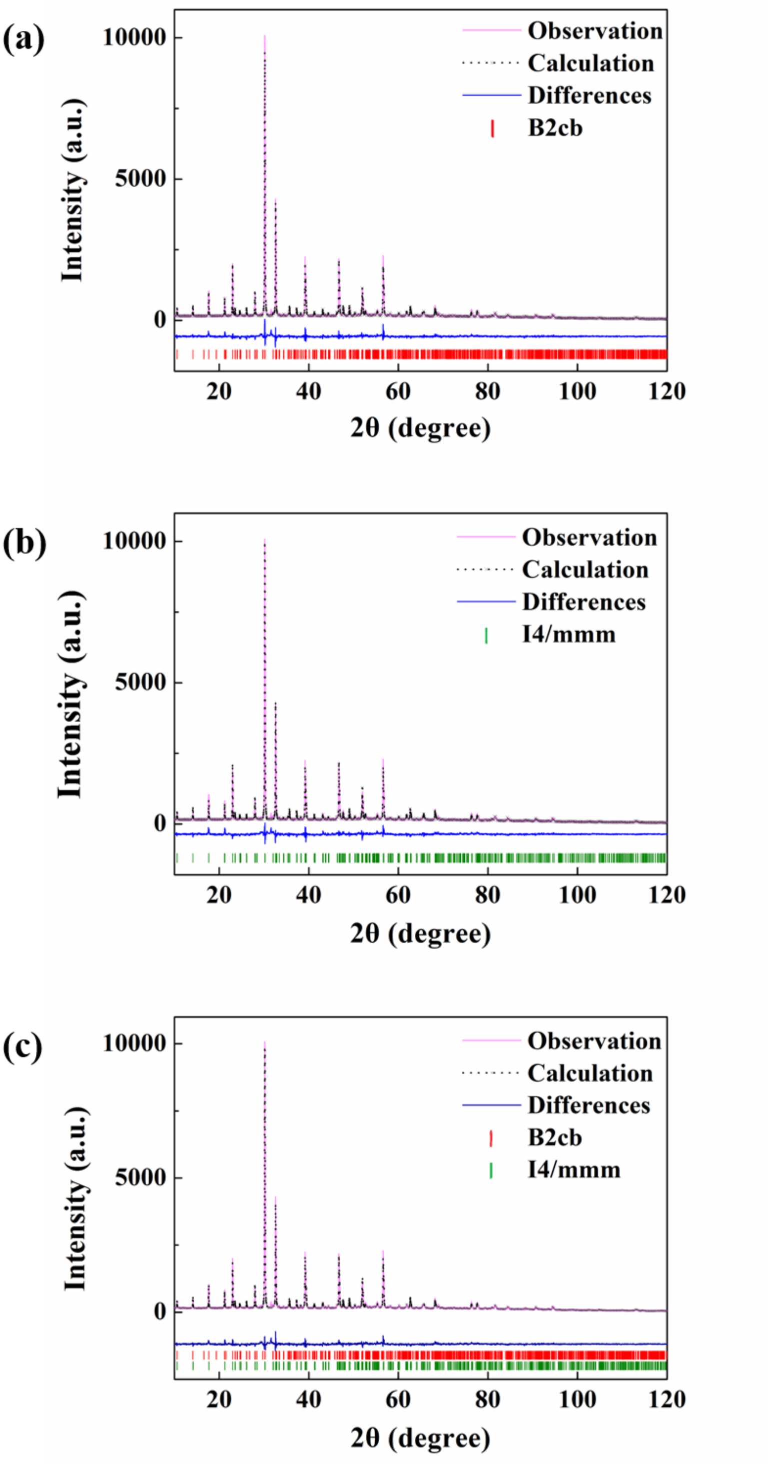

Figure 4.1 Rietveld XRD refinement of the B2BT powder using a structural model: (a) *B2cb* model (b) *I4/mmm* model (c) *B2cb* + *I4/mmm* mixture model, assuming the coexistence of the two phases.

Figure 4.1 shows the Rietveld refinement of the room-temperature XRD data of B2BT powder using the different structural models: an orthorhombic (SG *B2cb*) model [Figure 4.1 (a)], a tetragonal (SG *I4/mmm*) model [Figure 4.1 (b)], and a mixed (*B*2*cb*+*I*4/*mmm*) model [Figure 4.1(c)] which considers the coexistence of the orthorhombic and the tetragonal phases in the material, the standard XRD neutron diffraction data of *I4/mmm* and *B2cb* for Rietveld refinement were achieved from the reference JCPDS cards 01-073-6259 and 01-072-9952, respectively.[167,178] Tables 1 shows the refined structural parameters for the different polymorphs, as obtained by the Rietveld method using GSAS program.[177] A lower value of the weighted profile R-factor (R_{wp}) and profile residual (R_p) for the mixed model, if compared to that of the individual phases (*B2cb*, *I4/mmm*), suggesting the coexistence of the orthorhombic and tetragonal structures in B2BT ceramics. Moreover, the results of Rietveld refinements indicate that the mass fraction of the orthorhombic structure and the tetragonal structure is about 72 %/28 %, thus the main phase in B2BT ceramic is the polar *B*2*cb* structure. The crystal structure of *B2cb* and *I4/mmm* are shown by Figure 4.4.

Table 4.1 The refined structural parameters for the B2BT powder, as obtained by the Rietveld method using the single phase of orthorhobmic (*B2cb*) or tetragonal (*I4/mmm*) and the mixture of two phase orthorhobmic (*B2cb*) and tetragonal (*I4/mmm*).

Phase Existence State	Space Group	Refined Lattice Parameters			*wt %*	R_{wp}	R_p	x^2
		a (Å)	b (Å)	c (Å)				
B2cb or I4/mmm	*B2cb*	5.5009 (6)	5.4992(6)	50.379(2)	100 %	0.1122	0.0866	2.399
	I4/mmm	3.8892(1)	3.8892(1)	50.384(2)	100 %	0.1171	0.0854	2.615
B2cb and I4/mmm	*B2cb*	5.5009(7)	5.4975(7)	50.417(4)	71.8 %	0.1080	0.0829	2.227
	I4/mmm	3.8904(7)	3.8904(7)	50.323(3)	28.2 %			

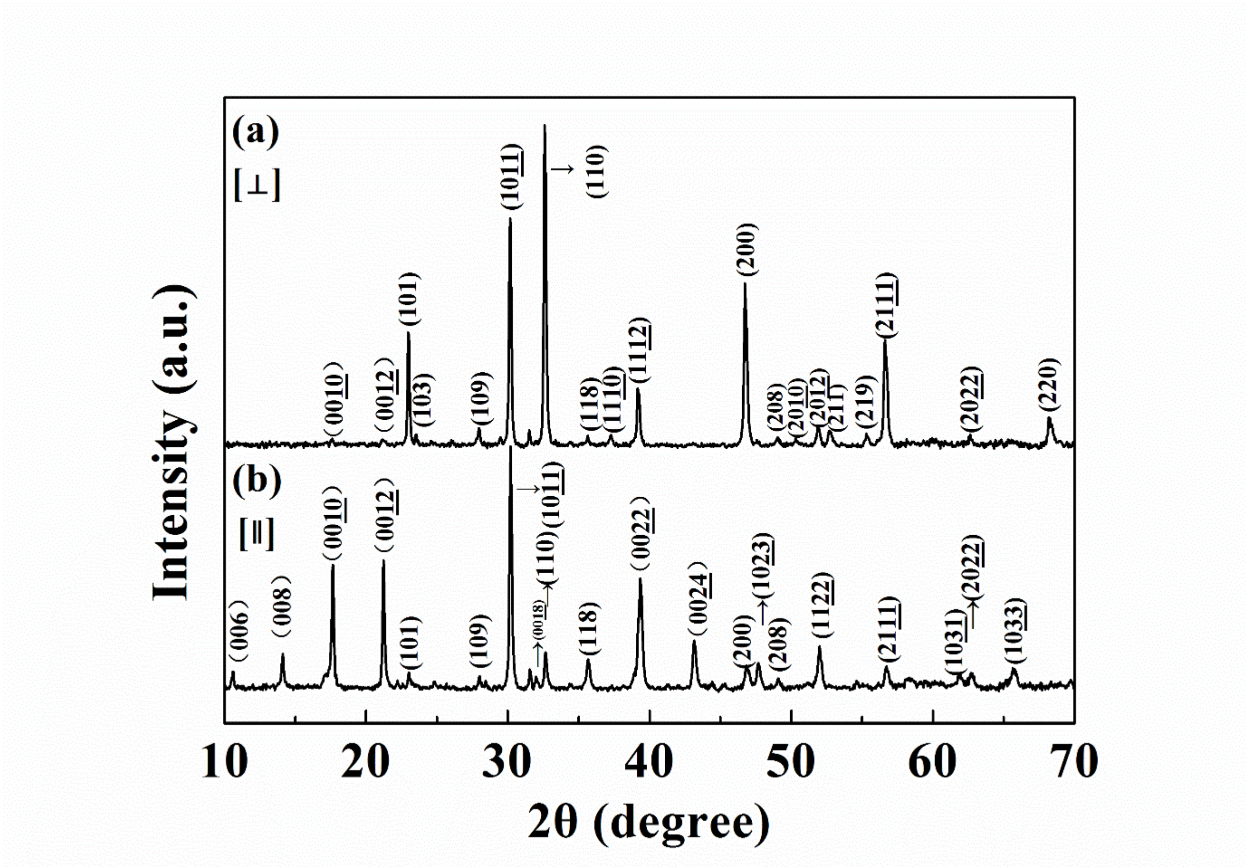

Figure 4.2 XRD patterns of the B2BT ceramics labelled by the *B2cb* space group (a) The X-ray incidence direction [⊥] and (b) the X-ray incidence direction [||] to the hot-pressing direction.

Figure 4.2 shows the XRD patterns of the SPSed B2BT ceramic collected at room temperature with the X-ray incidence direction perpendicular [⊥] and parallel [||] to the hot-pressing direction. In order to quantify a preferred orientation, the XRD patterns were indexed with reference to the orthorhombic *B2cb* crystal structure from the JCPDS card 01-072-9952. The XRD pattern [||] [Figure 4.2 (b)] shows strong (*00l*) diffraction peaks, while the [⊥] pattern [Figure 4.2(a)] has the weak (*00l*) reflections. This behaviour implies that the SPSed samples are textured. The degree of texture was estimated using the Lotgering factor *f*, which can be expressed as follows:[179, 180]

$$f = (p - p_0)/(1 - p_0) \tag{4.1}$$

where $p = \sum_{l} I(00l) / \sum_{hkl} I(hkl)$, $\sum_{l} I(00l)$ and $\sum_{hkl} I(hkl)$ are the sums of the intensities of (00*l*) and (*hkl*) reflections, respectively, and p_0 represents the value of p for a randomly oriented microstructure (in this study, p_0 is calculated from the XRD pattern of the powder ground from the SPSed ceramics). For the textured B2BT, the calculated *f*-factor is 0.62.

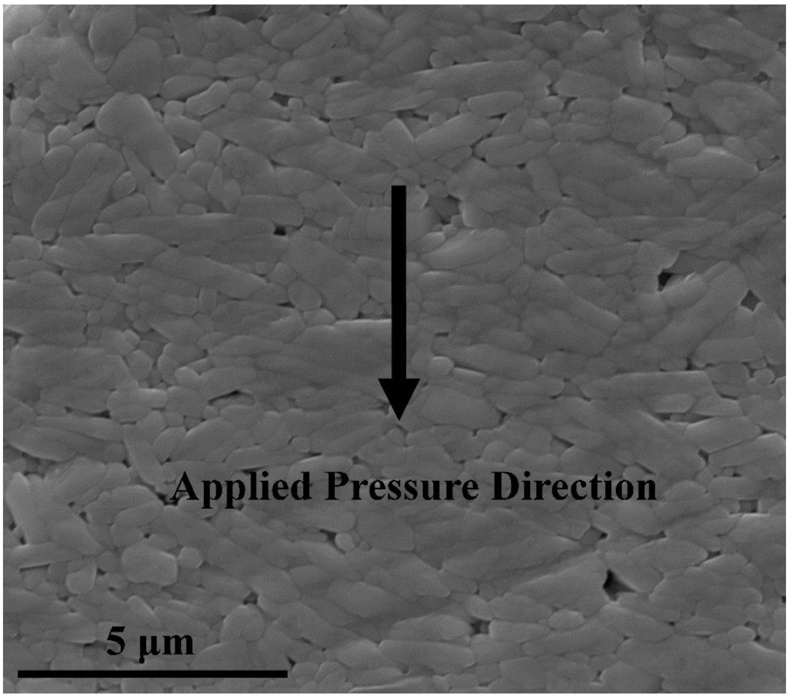

Figure 4.3 SEM image of the B2BT ceramic surface oriented parallel [||] to the hot-pressing direction. White arrow represents the applied pressure discretion.

Figure 4.3 shows the SEM image of the polished and thermally etched surface oriented parallel to the hot-pressing direction. The plate-like grains of B2BT form a brick-wall-like structure, in which the short axis is aligned preferentially parallel to the hot-pressing direction (marked by a white arrow in Figure 4.3). Thus, the grain morphology of the B2BT ceramics is consistent with the preferred orientation identified by X-ray diffraction (Figure 4.2). Due to the existence of high pressure, the easy growth plane would perpendicular to the pressure direction. The easy growth plane of B2BT is (*00l*) plane, which is consistent with the ferroelectric polarization preferred direction.[181] Therefore, texture would result in the high anisotropic characteristic on the structure and properties of B2BT. Theoretically, the dielectric and ferroelectric properties are stronger on the testing direction perpendicular to the pressure applied direction than parallel direction, which would be further investigated in the following sections.

Electrical properties characterization

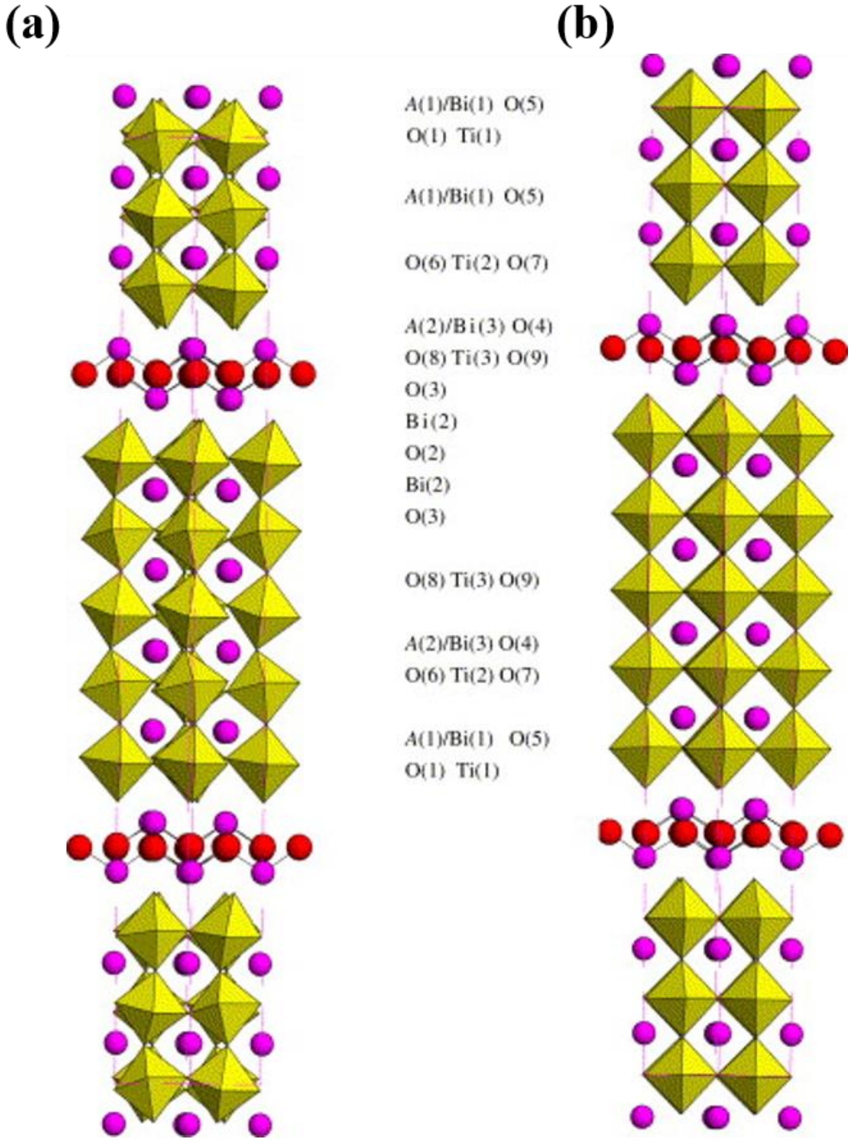

Figure 4.4 (a) polar structure of $A_2Bi_4Ti_5O_{18}$ with *B2cb* space group (b) non-polar structure with *I4/mmm* space group.[182]

The co-operative displacement of the atoms from the corresponding positions in tetragonal (*I4/mmm*) structure to orthorhombic (*B2cb*) structure along the a-axis lead to the appearance of the ferroelectric spontaneous polarization P_s in the B2BT ceramics. Figure 4.4 shows the ionic position of the non-polar phase (*I4/mmm*) and polar phase (*B2cb*). Figure 4.5 shows the ionic displacements and their contribution to the total spontaneous polarization (P_s). P_s was calculated as follows:[183]

$$P_s = \sum_i (m_i \times \Delta x_i \times Q_i e)/V \qquad (4.2)$$

where m_i is the site multiplicity (amount for each ions in one unit cell), Δx_i is the absolute atomic displacement along the a-axis, $Q_i e$ is the ionic charge for the ith constituent ion, and V is the volume of the unit cell. The atomic displacement data for the non-polar structure (*I4/mmm*) and the polar structure (*B2cb*) were achieved from the JCPDS cards 01-073-6259 and 01-072-9952, respectively.[167,178] And the multiplicity, displacement and volume conditions for each ions can be acquired by introducing the standard XRD PDF cards into *CrystalMaker*. The calculated P_s is 6.16 μC/cm^2, which is smaller than that of a single crystal (P_s = 12 μC/cm^2), The difference can be attributed to the electrical conductivity, which was present in the *P*-*E* loops measurements of the B2BT single crystal.[2,91]

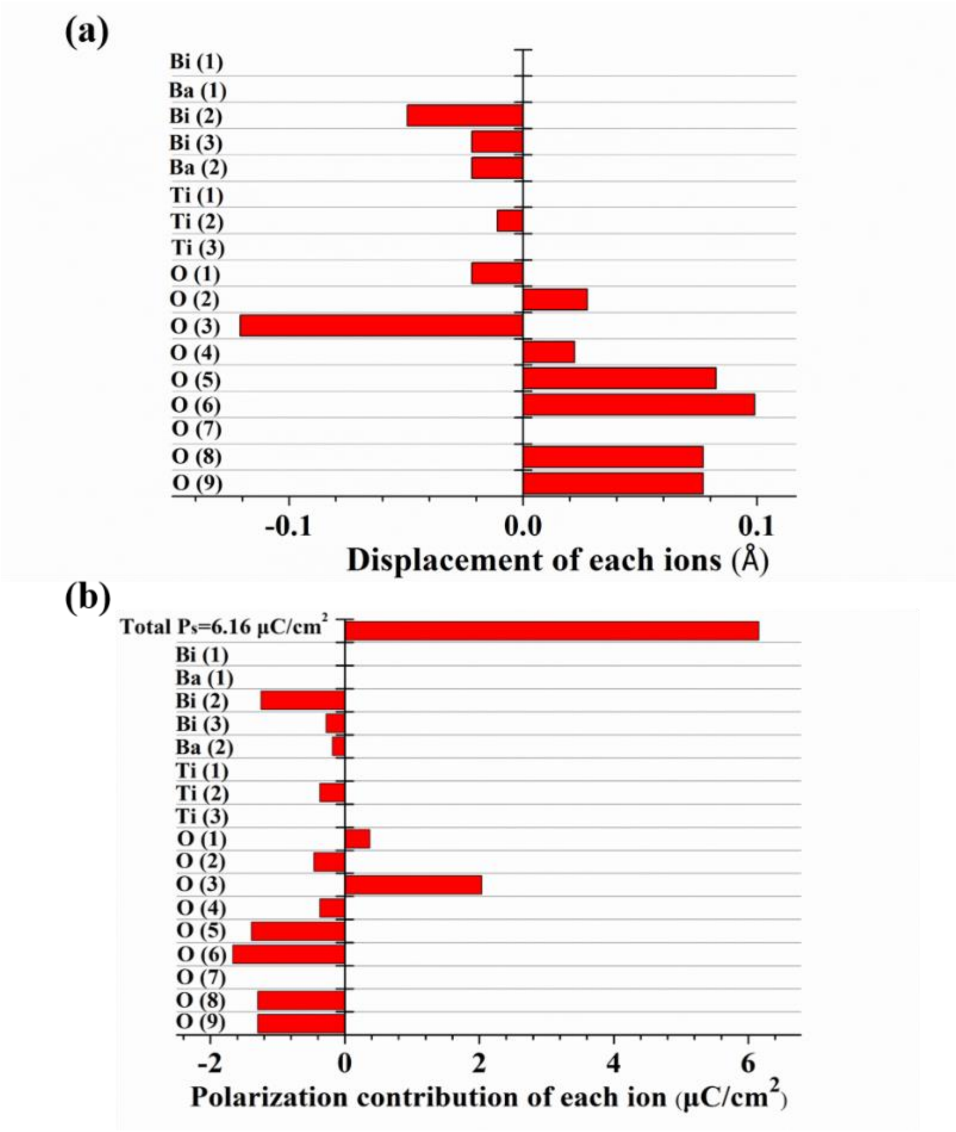

Figure 4.5 (a) Ionic displacements and (b) contributions of each constituent ion to the total spontaneous polarization P_s of B2BT.

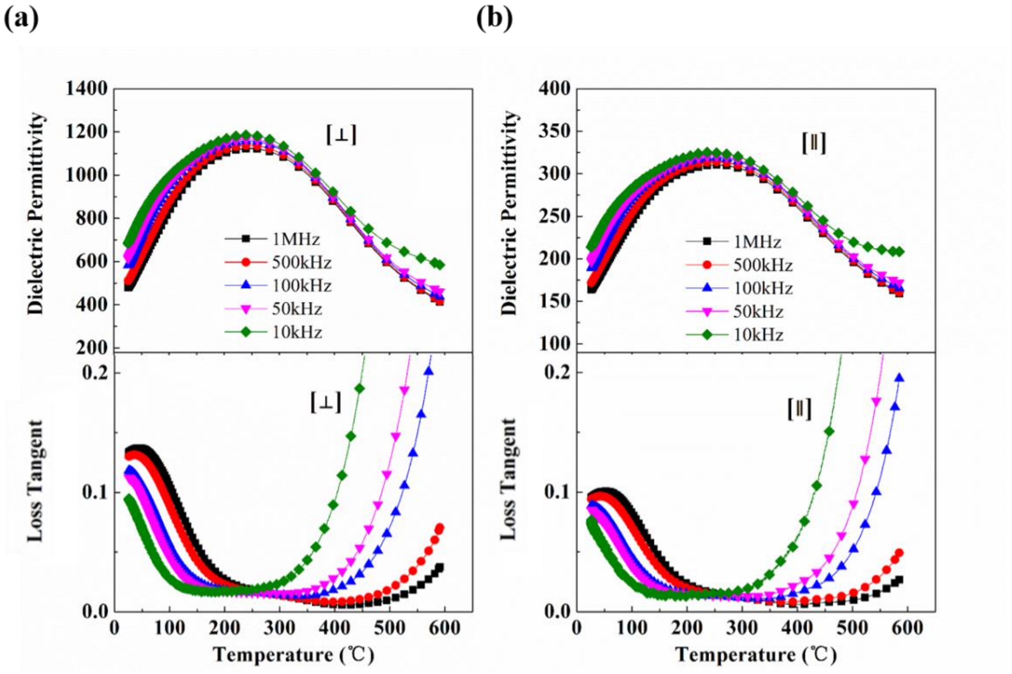

Figure 4.6 Temperature dependence of the relative dielectric permittivity and loss tangent (a) along the direction [⊥] and (b) along the direction [∥] to the hot-pressing direction (measured from 25 °C to 600 °C).

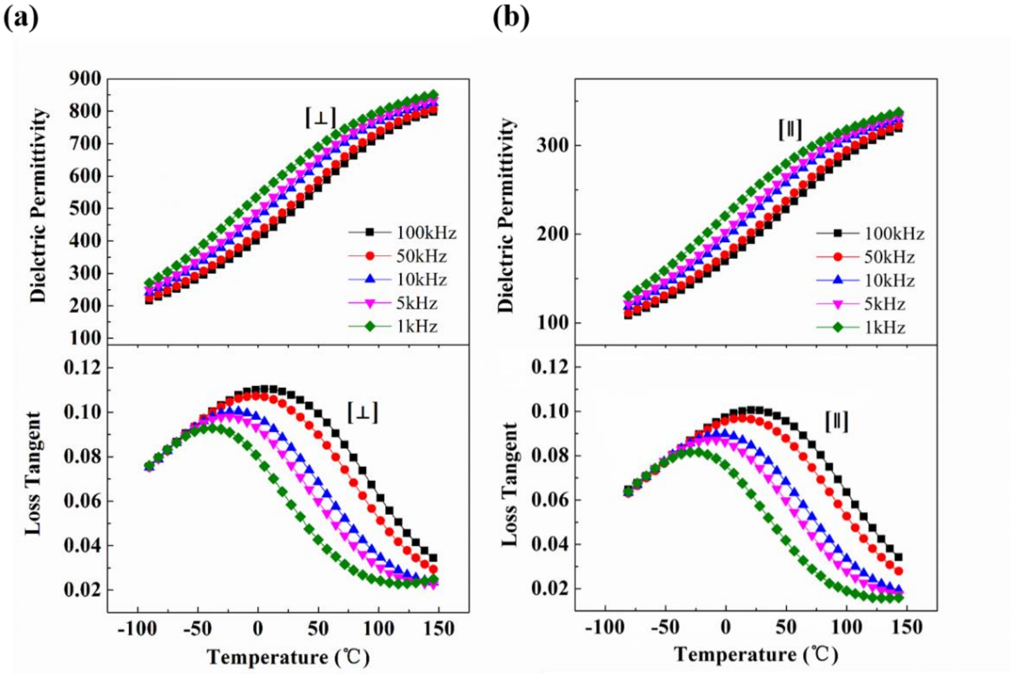

Figure 4.7 Temperature dependence of the relative dielectric permittivity and loss tangent (a) along the direction [⊥] and (b) along the direction [∥] to the hot-pressing direction (measured from -95 °C to 150 °C).

Figure 4.6 and Figure 4.7 show the relative dielectric permittivity (ε') and loss tangent ($\tan \delta$) of the B2BT ceramic, as measured at various frequencies (from 10 kHz to 1 MHz) along the different orientations as a function of the temperature. For both [⊥] and [||] directions, a very broad dielectric permittivity peak can be observed at around 240 °C and its positions does not change with frequency. The temperature of the maximum of the relative dielectric permittivity is denoted as T_m. The value of T_m along the perpendicular direction is close to that along the parallel direction. The dielectric permittivity peak value is about 1200 and 325 along [⊥] and [||] directions, respectively. A diffuse phase transition is often observed in Ba-substituted BLSFs. It is believed that the presence of the cation disorder between the perovskite A site cations and the bismuth cations in the Bi_2O_2 layer is responsible for the diffuse phase transition.[167] The frequency dependency of loss tangent peaks, characteristic of RFEs with the cation disorder, is evident at low temperatures (see Figure 4.7).

To describe the relaxation degree of RFE, a modified Curie-Weiss law has been employed:[184,185]

$$\frac{1}{\varepsilon} - \frac{1}{\varepsilon_m} = \frac{(T - T_m)^\gamma}{C_1} \tag{4.3}$$

where the degree of relaxation is described by the constants γ and C_1. The value of γ ranges between 1 and 2 (1 is for the conventional ferroelectrics and 2 is for an ideal relaxor).[185] γ was determined from the dielectric data collected at 100 kHz in the temperature region of 240-600 °C (Figure 4.6). The calculated γ is 1.35 and 1.23 in the perpendicular [⊥] and parallel [||] direction to the direction of the SPS pressing, respectively.

Table 4.2 The relaxation parameters obtained for the textured B2BT ceramic from V-F law.

Direction	Freezing temperature, T_{VF} (K)	Activation energy, E_a (eV)	Pre-exponential factor τ_0 (Hz)
[⊥]	186 (±6)	0.102 (±0.012)	1.0×10^9
[‖]	205 (±18)	0.082 (±0.024)	1.5×10^7

The dielectric relaxation of RFEs is known to follow the Vogel-Fulcher (V-F) law:[15, 16]

$$\tau = \tau_0 exp[\frac{E_a}{k_B(T_m - T_{VF})}] \tag{4.4}$$

where τ is the relaxation time in relaxors, τ_0 represents the inverse attempt frequency, E_a is the activation energy barrier for the fluctuation of each isolated PNRs, k_B is the Boltzmann constant, T_m is the temperature corresponding to the loss tangent maxima. Because the apparent REF behaviors only appear on loss tangent parts for B2BT, TVF is the 'static' dipole freezing temperature for relaxation, at which all relaxation times diverge and the distribution of relaxation times, τ, becomes infinitely broad. By fitting the loss tangent in the temperature range of -95 °C to 150 °C, the relaxation V-F parameters were obtained (Table 4.2). T_{VF} of the B2BT ceramics along [‖] and [⊥] directions is 186 ± 6 K and 205 ± 18 K, respectively. From the Table 4.2, one can see that the calculated values of both T_{VF} and E_a along [⊥] and [‖] directions are close to each other indicate that the different dielectric behavior origins from the same dipoles.

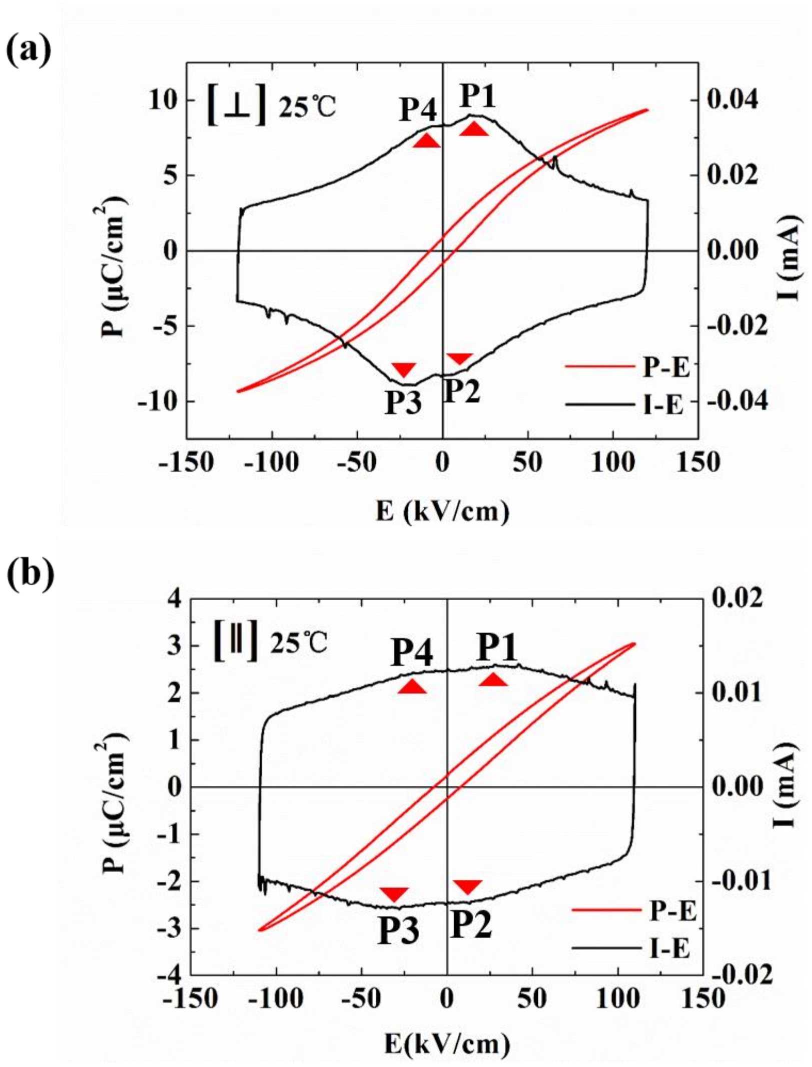

Figure 4.8 *P-E* and *I-E* loops of the B2BT ceramic measured (a) along the direction [⊥] and (b) along the direction [‖] to the hot-pressing direction (25 °C).

Figure 4.8 shows the *P-E* and *I-E* loops of the B2BT ceramic tested along [⊥] and [‖] directions at a frequency of 10 Hz and at room temperature. The maximum applied field for the *P-E* loops measurements were 120 kV/cm and 110 kV/cm in the perpendicular [⊥] and parallel [‖] direction to the SPS pressing direction, respectively. It is well known that ferroelectric domain switching in an ordinary ferroelectric is manifested by sharp current peaks in the 1st and the 3rd quadrants of the *I-E* loops.[186,187] In Figure 4.8, these peaks are marked as P1 and P3. Interestingly, the *I-E* loops of the B2BT ceramic display additional peaks, P2 and P4, which appear in the 2nd and the 4th quadrant of the *I-E* loops in course of decreasing electric field. Although, the P2 and P4 peaks in the B2BT [ǁ] sample are not as obvious as these of the [⊥] sample, they are discernible in the loops of both samples, as shown in Figure 4.8 (b). Similar observations were previously reported for $Bi_{0.5}Na_{0.5}TiO_3$-based ferroelectric materials and the appearance of four switching peaks in the *I-E* loops were linked with electric field-induced reversible transitions.[188-190] This is the first time, to our best knowledge, that four switching current peaks are observed in the *I-E* loops of relaxor ferroelectrics in the BLSFs family.

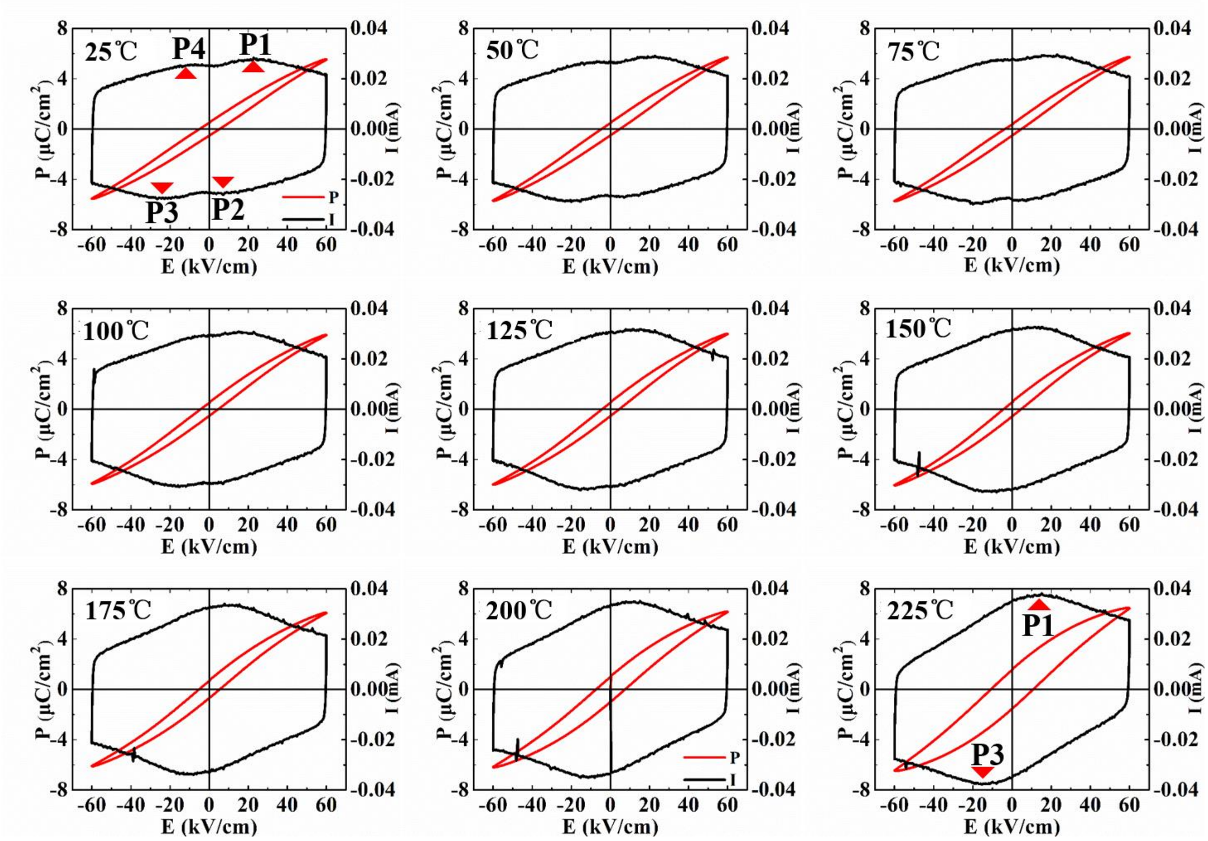

Figure 4.9 *P-E* and *I-E* loops of the B2BT ceramic, as measured in the perpendicular direction [⊥] to the hot-pressing direction at temperatures from 25 °C to 225 °C.

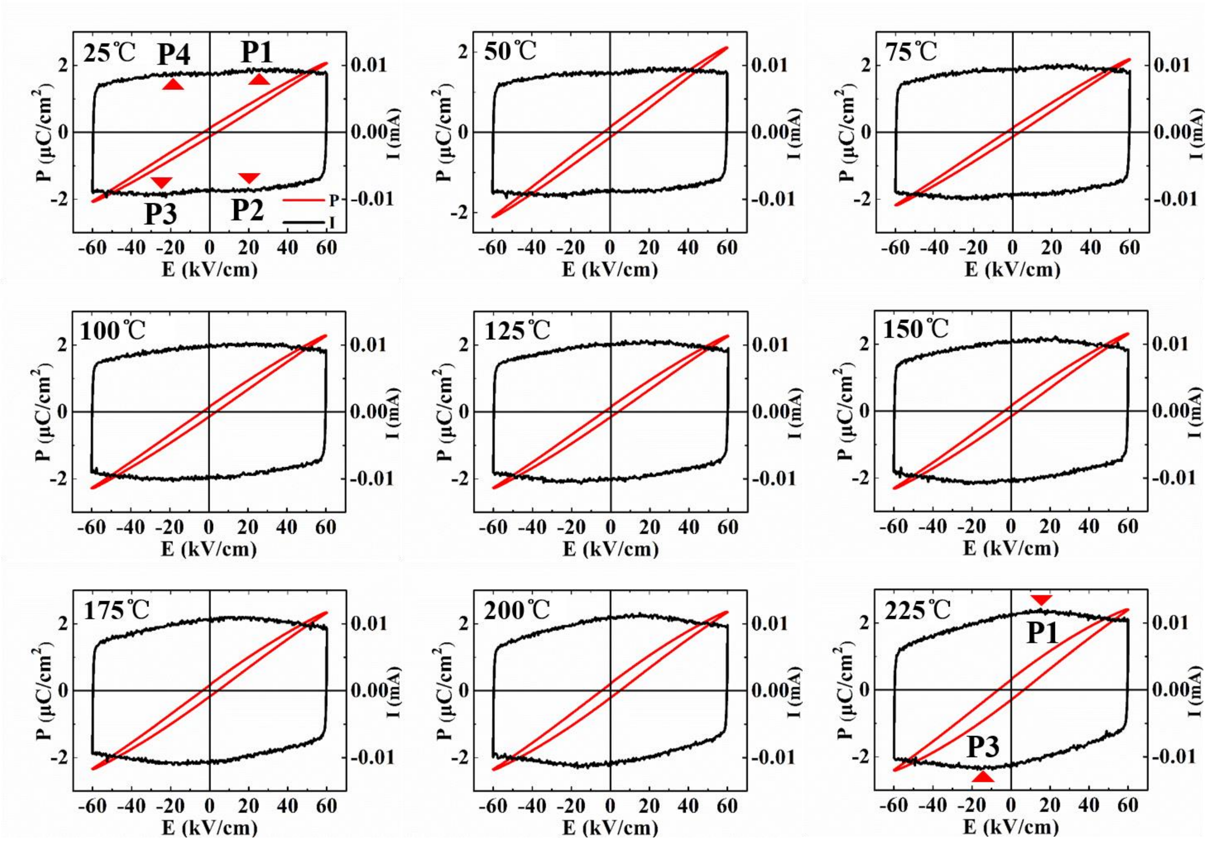

Figure 4.10 *P-E* and *I-E* loops of B2BT ceramic, as measured in the parallel direction [ǁ] to the hot-pressing direction at temperatures between 25 °C and 225 °C.

Figure 4.9 and Figure 4.10 show the evolution of the *P-I-E* loops of the B2BT [⊥] and [ǁ] ceramics, respectively, with increasing temperature from 25 °C to 225 °C (recorded at 10 Hz). Four switching current peaks (P1, P2, P3 and P4) are clearly visible in the *I-E* loops of both the [⊥] and [ǁ] ceramic samples in the temperature region from 25 °C up to 100 °C. While the switching current peaks P1 and P3 are discernible up to 225 °C for both the [⊥] and [ǁ] ceramics, the P2 and P4 peaks disappear at temperatures above 100 °C. The *P-E* loops are slim over the all temperature range studied. The remnant polarization (P_r) of both the B2BT [⊥] and [ǁ] ceramics slightly increases with the increasing temperature. Such an enhancement of the polarization can be attributed to a temperature-driven increase in leakage current.[187]

As shown in Figure 4.8 (a), the field induced polarization (9.0 μC/cm^2) is relatively high while the remnant polarization (P_r = 0.82 μC/cm^2) is extremely low, indicating that the electric field-induced polarization is unstable when the applied field is removed. Piezoelectric constant d_{33} of the poled B2BT [⊥] ceramic was 0.4 pC/N, while there was no detecable pizeoelectric response for the [||] sample. Although the measured d_{33} value is very small, it is far beyond the instrumental error of the piezo d_{33} meter (±0.1 pC/N). Thus, we propose that that the textured B2BT ceramics exhibits a piezoelectric response in the perpendicular direction to the direction of the SPS hot-pressing. The weak piezoelectricity is consistent with the extremely small value of P_r (Figure 4.8 (a)). Our findings about slim *P-E* loops, switching current peaks behaviour, and non-zero d_{33} coefficient allow us to conclude that the B2BT ceramic is a relaxor ferroelectric.

Most ferroelectric materials undergo a structural phase transition from a high-temperature paraelectric phase into a low-temperature ferroelectric phase at the so-called Curie temeprature (T_c). The B2BT ceramic consists of the ferroelectric *B2cb* phase, which is a major phase, and the paraelectric *I4/mmm* phase at room temperature. This indicates that the high-temperature paraelectric phase does not fully transform into the ferroelectric phase on cooling. We believe that the evolution of the four peaks in the *I-E* loops (Figure 4.9 and Figure 4.10) can be related to the structure evolution and the temperature dependent polarization reversal in B2BT. The ferroelectric orthorhombic phase is thermally stable up to T_m or T_c (~ 240 °C). The application of a sufficiently high electric field to a ferroelectric may induce an irreversible transition from random orientated small domains into strongly aligned large domains via domain switching. The majority of the aligned domains in the B2BT ceramics do not backswitch upon removal or reduction of the electric field in the temperature range from 25 °C to 225 °C. This behaviour results in the appearance of the P1 and P3 peaks in the *I-E* loops. However, when the paraelectric tetragonal phase is cooled down from the temperature above T_B, a localized symmetry breaking (i.e. short-range order) may occur at the Burns temperature T_B (normally higher than T_m or T_c). As a consequence, weak polar nanoregions (PNRs) are formed within the non-polar paraelectric phase, giving rise to the onset of relaxor characteristics of the tetragonal *I*4/*mmm* phase. The relaxor phase is subject of strong thermal fluctuations, and thus it is the thermally unstable structure. Upon further cooling, a glass-like transition occurs at the freezing temperature T_{VF} (~ 200 K for B2BT as shown in Table 4.2), where thermal fluctuations of PNRs vanish. At temperatures above T_{VF}, a reversible electric field-induced transition occurs in the relaxor phase. The application of an external electric field enables the weak polar state to transform into a long-range ferroelectric state, which contributes to the electrical polarization and current peaks at the 1st and 3rd quadrant of the *I-E* loops (Figure 4.8, Figure 4.9, Figure 4.10). However, this electric field-induced polar state is highly unstable and returns back to its initial state immediately upon removal or reduction of the electric field.[189,190] The recovering of the weak polar state is manifested in the *I-E* loops (Figure 4.8, Figure 4.9, Figure 4.10) by the switching current peaks P2 and P4. When the temperature is below 100 °C, both the electric field-induced PNRs in the paraelectric phase and the ferroelectric domain switching in the ferroelectric phase can contribute to the switching current peaks P1 and P3 in the 1st and 3rd quadrant of the *I-E* loops. The current peaks P2 and P4 in the 2nd and 4th quadrant are only associated with the electric field-driven reversible transformation in the tetragonal phase. When the temperature is above 100 °C, the electric field-induced transition is difficult to occur within the tetragonal phase due to strong thermal fluctuations. Therefore, the P2 and P4 peaks are not observed in the *I-E* loops at temperatures above 100 °C (see Figure 4.9, Figure 4.10). From the ferroelectric property measurements, it is suggested that the current peaks P1 and P3 can be related to the electric field-induced irreversible transition in the ferroelectric *B*2*cb* phase. The non-zero d_{33} value of the poled B2BT [⊥] ceramic is also supportive of the domain switching in the orthorhombic *B*2*cb* phase.

4.1.4 Summary

The highly textured B2BT ceramic with the Lotgering factor of 0.62 was successfully prepared by SPS. Rietveld refinement of the room-temperature XRD data revealed that the crystal structure of the ceramic consists of both the polar orthorhombic (*B2cb*) phase and the non-polar tetragonal (*I4/mmm*) phase. A diffused phase transition at around 240 °C was identified in the sample measured along the perpendicular [⊥] as well as the parallel [||] direction to the SPS hot-pressing direction. No shift of the transition temperature with frequency was observed. In the *I-E* loops, four distinct current peaks were found for both the [⊥] and [||] samples. The evolution of the switching peaks with increasing temperature is explained by the structural changes and temperature dependent polarization reversal. In the temperature range from 25 °C to 225 °C, the electric field-induced domain switching in the ferroelectric *B2cb* phase contributes to the current peaks only in the 1st and 3rd quadrant of the *I-E* loops. On the other hand, it was found that at temperatures between 25 °C and 100 °C the electric field-induced reversible transition from a weak polar state to a long-range ferroelectric state in the paraelectric (or relaxor) phase contributes to the switching current peaks at every quadrants of the *I-E* loops. Above 100 °C, no polarization reversal within the paraelectric (or relaxor) phase was observed due to large thermal fluctuations. The observation of slim ferroelectric *P-E* hysteresis loops, the appearance of additional switching current peaks in the *I-E* loops and non-zero d_{33} piezoelectric coefficient (~ 0.4 pC/N for the B2BT [||] ceramic) are considered as a strong evidence of relaxor ferroelectric state in the B2BT ceramic.

4.2 The crystal structure of $Ba_2Bi_4Ti_{4.5}Mn_{0.5}O_{18}$ ceramics

4.2.1 Introduction

Based on the work of textured $Ba_2Bi_4Ti_5O_{18}$ ceramic, we designed a novel multiferroics of $Ba_2Bi_4Ti_{4.5}Mn_{0.5}O_{18}$. In terms of Aurivillius compounds, due to the movement of BO_6 octahedral cations within *a- (b-)* plane generates the spontaneous polarization. It is possible to introduce transition metal elements (such as Fe, Co and Mn) into the B-site to build the novel multiferroics that magnetic and electric properties all originate from the B-site. And the magnetoelectric (ME) effect can also be generated through the movement of BO_6 octahedral. In this work, $Ba_2Bi_4Ti_{4.5}Mn_{0.5}O_{18}$ was tried to be calcined under different temperature conditions. However, no single phase ceramics was achieved after vast times of trials.

4.2.2 Characterizations

Crystal structure determination and refinements

X-ray diffraction (XRD) patterns of the ceramics were collected at room temperature by an X-ray diffractometer (Panalytical Xpert Pro diffractometer, $CuK\alpha$ radiation).

4.2.3 Results and discussions

The XRD patterns of calcinated powders at three different temperature (1025 °C, 1050 °C, 1075 °C) was shown by Figure 4.11, it can be found that the positions of diffraction peaks that corresponding to three different calcination temperature are the same. Only the intensity of peaks changed slightly. In contrast with the standard XRD patterns of the pure

$Ba_2Bi_4Ti_5O_{18}$ (B2BT) that belongs to *B2cb* space group (blue line in Figure 4.11, JCPDS-01-072-9952), pure $BaBi_4Ti_4O_{15}$ (BBT) belongs to *I4/mmm* space group (orange line in Figure 4.11, JCPDS-01-035-0757) and pure $BaTiO_3$ (BTO) belongs to *Pm-3m* space group (black line in Figure 4.11, JCPDS-01-075-0212), it could be found that the achieved powder is the combination of BBT and BTO under both three different calcination conditions. That's because the melting point of MnO_2 and Mn_2O_3 are only 535 ºC and 940 ºC, respectively, which could reduce the melting point of powders. The lower melting point result to the maximum synthesis temperature for this composition is not high enough to provide the energy to acquire the single phase $Ba_2Bi_4Ti_{4.5}Mn_{0.5}O_{18}$.

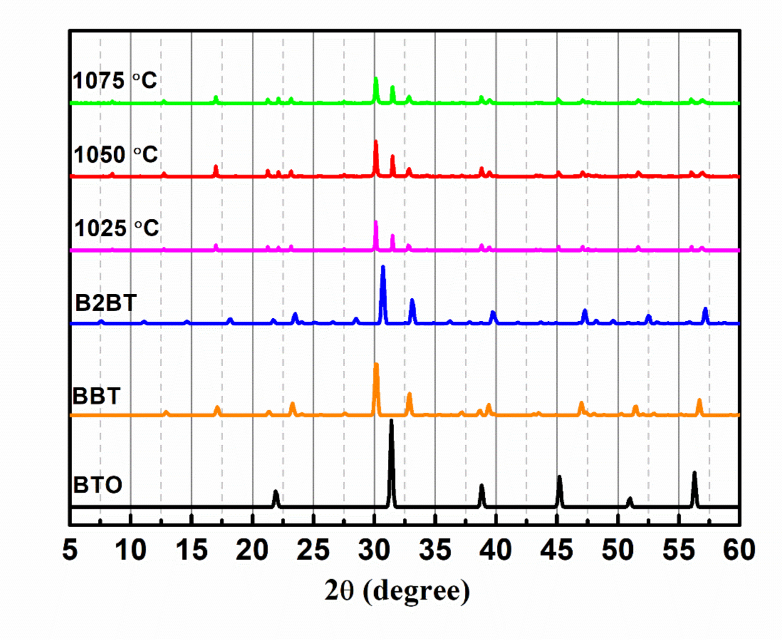

Figure 4.11 The XRD results corresponding to four different calcination temperature 1025 ºC (pink), 1050 ºC (red), 1075 ºC (green). The possibilities of composed compound's standard XRD results are listed as B2BT, BBT and BTO by blue, orange and black curves, respectively.

4.2.4 Summary

These unsuccessful calcinations remind us introducing Mn into this compound will lower the mixture melting point, which could be ascribed to the melting point of MnO_2 and Mn_2O_3 are only 535 ºC and 940 ºC, respectively. Moreover, it is suggested that the doping of Mn lead to the theoretical calcination temperature increase to more than 1100 ºC. This could be proved by the final products were the combinations of four layers Aurivillius of BBT and the BTO below 1100 ºC calcination temperature. The doping of Mn makes melting point decrease and the calcination temperature increase. These two changes result to the unsuccessful calcinations.

Chapter V Investigation of multiferroics ceramics behaviour of Na0.5Bi0.5Ti0.8Mn0.2O3 with Nb doping

5.1 Introduction

In the past decades, the perovskite compounds (ABO_3) act as a type of new class of ferroelectrics that possess both ferroelectricity and piezoelectricity, which have attracted numerous application explorations on sensors, transducers, actuators, etc. It is well known that the ferroelectrics commonly exhibits B-site disorder, such as $Pb(Mg_{1/3}N_{2/3})O_3$ (PMN), for which the disordered dispersion of Mg^{2+} and Nb^{5+} is the origins of the relaxor behavior.[191] Unlike to the B-site disorder ferroelectrics, $Bi_{0.5}Na_{0.5}TiO_3$ (BNT) is the very rare lead-free perovskite with A-site disorder occupied by half Na^+ and half Bi^{3+}, it possesses rhombohedral distortion ($R3c$ space group).[191-193] BNT is also well known as its strong ferroelectricity with relatively large remnant polarization (P_r = 38 μC/ cm^2) under room temperature.[194] The 6s lone pair electrons in Bi^{3+} ions for BNT lead to the Bi-O bonding anisotropic and further result in the mismatch between Bi ions and oxygen octahedrons. This strongly relative displacement is responsible for remnant polarizations. This configuration is similar with the lead-based ferroelectrics in which 6s lone pairs electrons contribute to the polarizations.[193,195,196]

In this study, the well-known ferroelectric $Na_{0.5}Bi_{0.5}TiO_3$ was selected as the basic compound for doping. The designated novel multiferroic is $Na_{0.5}Bi_{0.5}Ti_{0.8}Mn_{0.2}O_3$ with 2 mol. % Nb additive (BNT8M2+Nb). It is promising that the exchange interaction between each pair of adjacent electrons spin of Mn ions contribute to the magnetism.[197] We also anticipate the distortion of cells during ferroelectric polarization changes would simultaneously change the electrons spin status of Mn ions and verse vice, to achieve the intrinsic magnetic-electric coupling.

5.2 Characterizations

Crystal structure determination and refinements

X-ray diffraction (XRD) patterns for the ceramics were achieved by an X-ray diffractometer.

Microstructural characterization

The microstructure of ceramic pellet was obtained by a scanning electron microscope (SEM). The samples for SEM observation were etched under 900 ºC for 20 mins to reveal the grain boundaries.

Electrical property characterization

The temperature (-195 ºC to 600 ºC) and frequency (100 Hz to 10 MHz) dependence of dielectric permittivity, loss was measured by using an LCR meter. The polarization-current-electric field (*P-I-E*) hysteresis loops were captured by using a hysteresis at frequency of 10 Hz.

Magnetic property characterization

The magnetization hysteresis (*M-H*) loops and zero-field cooling and field cooling (ZFC-FC) data were all measured by superconducting quantum interference device magnetometer (Quantum Design, a model MPMS (SQUID) VSM). The *M-H* loops were measured under temperature of 10 K, 20 K, 30 K and 285 K. The ZFC-FC data were measured from 10 K to 300 K. The *M-H* loops have been subtracted the paramagnetic contribution to reveal the pure ferromagnetism.

5.3 Results and discussions

BNT8M2+Nb crystal structure characterization

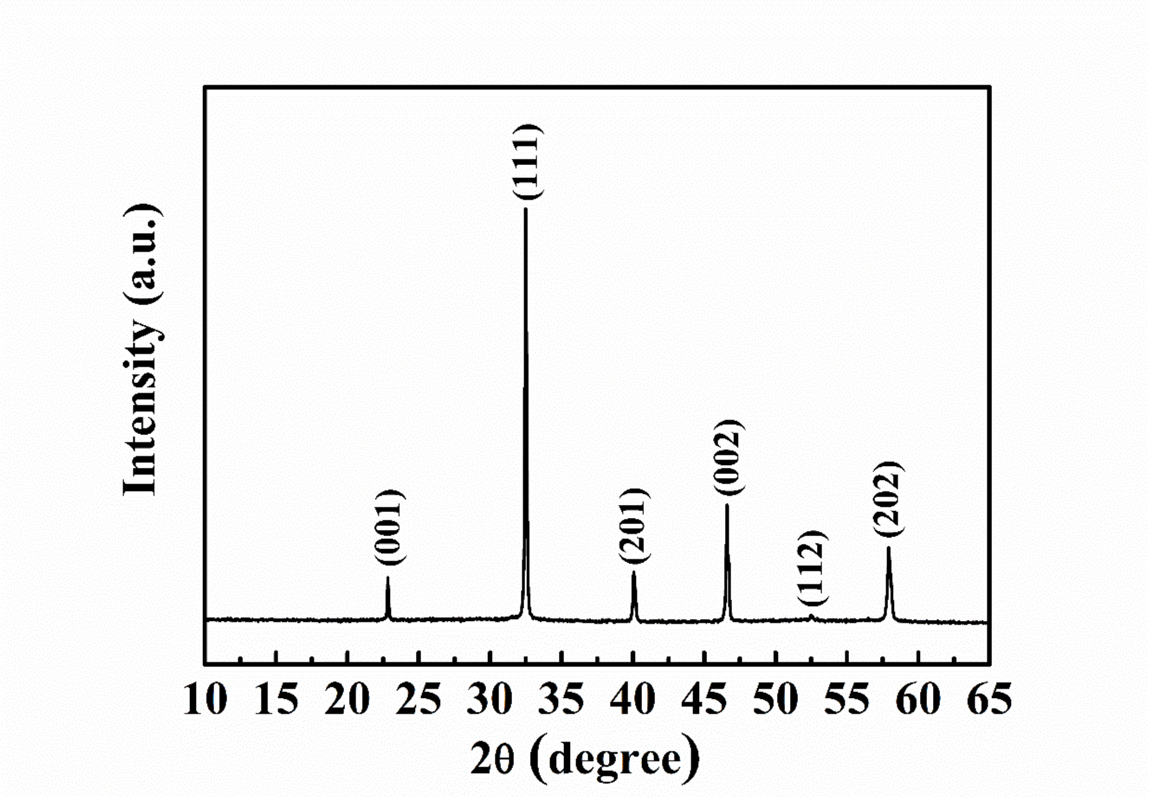

Figure 5.1 The XRD patterns of BNT8M2.

Figure 5.1 shows X-ray patterns of BNT8M2+Nb powders after calcination. These powders are single phase present no impurities phase peaks and belongs to *R3c* space group. The similar structure of pure BNT was reported by Thomas Pamela *et al.* in 2005.[198] The practical peak position shift to higher angle slightly with respect to standard peak position, According to the Bragg's law:

$$n\lambda=2d\sin\theta \tag{5.1}$$

where λ is the X-ray wavelength, d is the lattice spacing and θ is the incidence angle of X-ray wavelength. The phenomenon of peak shift to higher angle could be attributed to the ionic radius of Mn^{4+} (53 pm) is smaller than Ti^{4+} (60.5 pm).

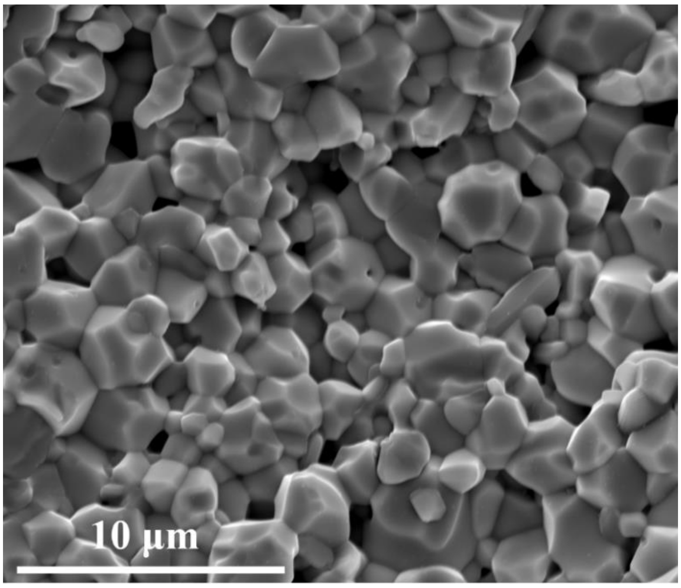

Figure 5.2 SEM microstructure of the thermally etched surface of BNT8M2.

Figure 5.2 shows the microstructure of BNT8M2+Nb ceramic with high density (97.4 %) that prepared by solid state sintering method. The grains are rectangular shape with grain size at about 1-3 µm, the similiar microstructure of BNT has been reported by Ranjit Pattanayak *et al.*, which reveals that the Mn doping has not changed the grain shape apparently.[199]

Electrical properties characterization

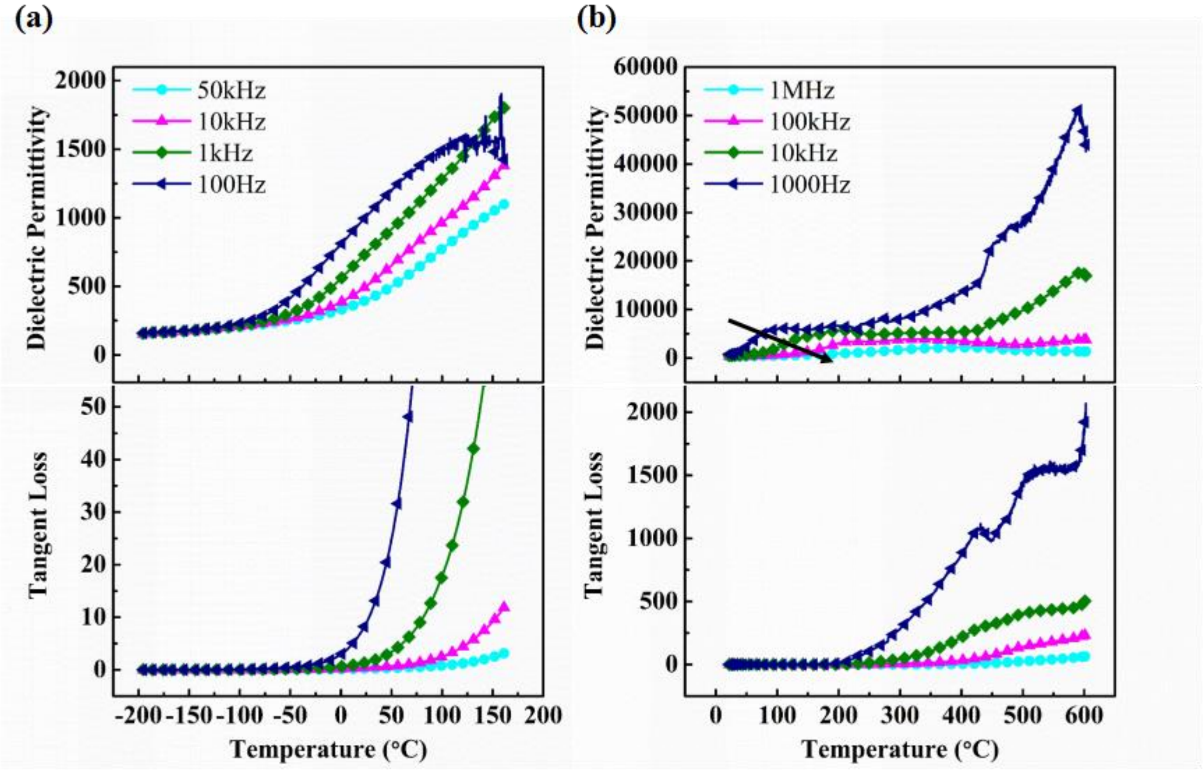

Figure 5.3 The temperature dependence of dielectric permittivity and loss tangent for BNT8M2+Nb at different frequencies.

Figure 5.3 shows the temperature dependence of dielectric permittivity and loss tangent for BNT8M2+Nb from -195 ºC to 600 ºC at different frequencies. A strong dielectric relaxation is observed from 25 ºC to 200 ºC, as shown by the black arrow in Figure 5.3(b). Within this temperature range, an evident hump is observed at 1000 Hz. For the frequency increase from 1000 Hz to 1 MHz, this hump transfer to slope gradually. And it is notable that for temperature range from 200 ºC to 600 ºC, the dielectric permittivity and tangent loss transfer from weak temperature dependent to strong temperature dependent with frequency decrease. That’s because the relaxor type dipoles are the main contribution for tangent loss. The loss tangent increase exponentially with temperature increase, which is consistent with AC leakage conductivity.

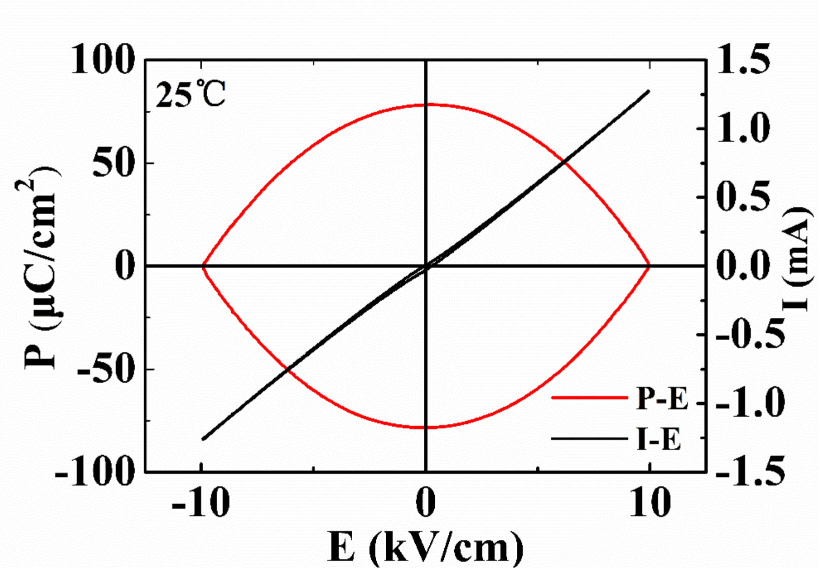

Figure 5.4 The *P-I-E* loops of BNT8M2 under room 25 ºC.

Figure 5.4 shows the *P-E* and *I-E* hysteresis loops of BNT8M2+Nb under temperature of 25 ºC with measuring frequency at 10 Hz. We can easily find the round-shape *P-E* loops that demonstrate the extremely high leakage conductivity. Even though the conductivity is still high, but it has been improved dramatically to be compared with the Nb free BNT8M2 that commonly been broke down under electric field of 1 kV/cm, which restrict the *P-E* and *I-E* loops measurements. It is suggested that the leakage conductivity contributed by the variable valence of Mn ions. Since the Mn doped BNT is rarely reported, the Mn ions induced leakage conductivity mechanism is still not clear. For BNT based ceramics, Nb is the commonly used dopants that served as the donor to restrict the forms of oxygen vacancies. Ming Li *et al.*,[200] reported the Nb-doped BNT (Nb content ~ 0.5 at. % - 1.0 at. %) that presents much higher activation energy (E_a ~ 1.5-1.8 eV) than the undoped BNT (E_a < 0.9 eV), which provides the Nb-doped BNT much higher resistivity. In this study, 2 mol. % Nb was added into BNT8M2+Nb. For the Nb doped samples, the max applied electric field has been increased to 10 kV/cm (breakdown electric field < 1 kV/cm for the undoped BNT8M2), which indicated that Nb is effective for leakage conductivity reduction. However, the nearly linear response of *I-E* loops reveal that the leakage conductivity is still a barrier for the observation of ferroelectric domain switching in *I-E* loops.

Magnetic properties characterization

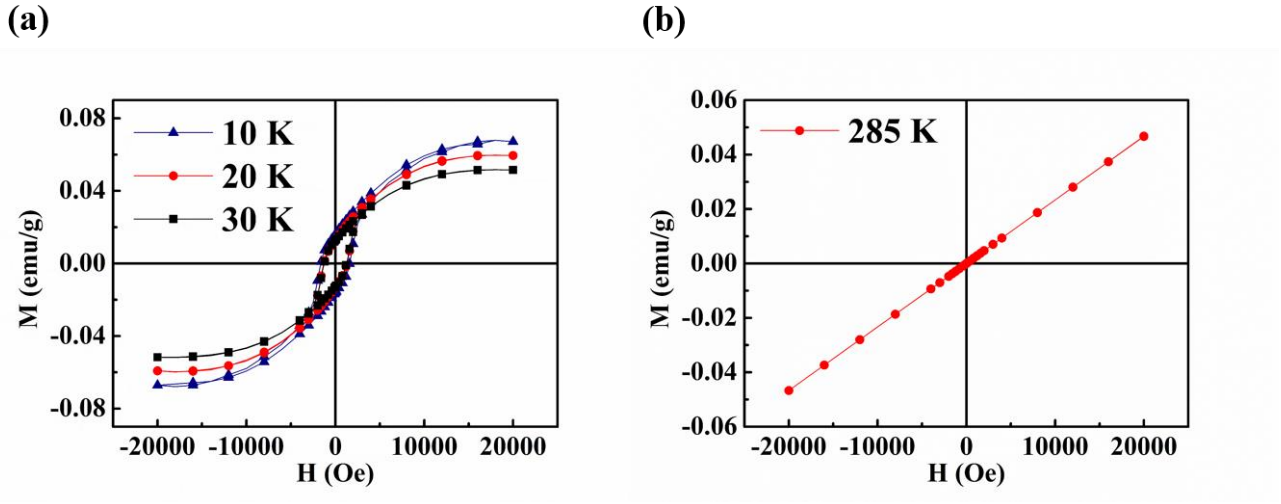

Figure 5.5 The magnetic field dependence of magnetization for BNT8M2+Nb under different temperature (a) 10K, 20 K, 30 K and (b) 285 K.

The magnetic field dependence of magnetization for BNT8M2+Nb were measured by SQUID magnetometer at four temperature point of 10 K, 20 K, 30 K and 285 K, which were depicted by Figure 5.5. At temperature of 30 K, 20 K and 10 K, the BNT8M2+Nb present ferromagnetism, the remnant magnetization increase with temperature decrease and reaches approximately 0.016 emu/g at 10 K, as illustrated by Figure 5.5 (a), where the paramagnetic contribution from substrate was subtracted. The room temperature paramagnetic nature is strongly supported by the linear *M-H* loops with almost no remnant magnetization, shown by Figure 5.5 (b).

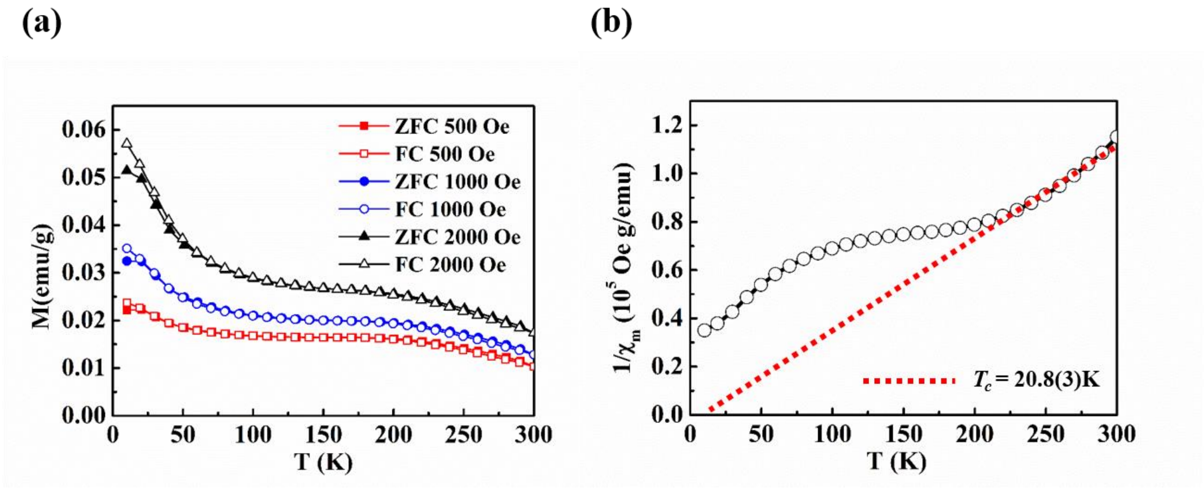

Figure 5.6 (a) Zero-field cooled (ZFC) and field cooled (FC) magnetization curves of BNT8M2+Nb at 500 Oe (Red curve), 1000 Oe (blue curve) and 2000 Oe (black curve). (b) Black open circles represent the temperature dependence of inverse magnetic susceptibility $1/\chi_m$ derived from FC magnetization for 2000 Oe. The red straight line is the linear fitting by the Curie-Weiss law on the high temperature paramagnetic linear part of $1/\chi_m$ for BNT8M2+Nb.

In order to understand the magnetic behaviour of BNT8M2+Nb, the zero-field cooled (ZFC) and field cooled (FC) magnetization curves were measured between temperature 10 K and 300 K under 500 Oe, 1000 Oe and 2000 Oe magnetic field, respectively. The ZFC data were collected on the heating process after samples were zero-field cooled and the FC data were collected on the following field cooling process, the curves are shown by Figure 5.6 (a). It is observed that there are two critical point at around 200 K and 50 K for all ZFC and FC curves. The ZFC and FC curves show apparent bifurcation, and the bifurcation temperature increase with magnetic field increase. This irreversible FC and ZFC magnetic behaviour without the sudden drop of ZFC curve after divergence point is suggested as the proof of the existence of the spin glass state.[201,202]

In order to further confirm the magnetic phase transition behaviour. The plots of inverse susceptibility ($1/\chi_m$) as a function of temperature is fitted with Curie Weiss law, shown by Figure 5.6 (b), which could be expressed as:[21,203]

$$\chi = \frac{C}{(T-\theta)} \tag{5.2}$$

where C is the Curie constant and θ is the paramagnetic Curie temperature, which has no actual physical meaning. The positive intercept of linear fitting function on x-axis, θ = 20.8(3) K, combined with the apparent remnant magnetization at low temperature, which further confirm the magnetic interaction in BNT8M2O+Nb system is low temperature ferromagnetic (FM) with T_c at around 50 K.[21,204,205]

5.4 Summary

In this chapter, the structures, dielectricity, ferroelectricity and magnetic properties were strictly investigated for $Bi_{0.5}Na_{0.5}Ti_{0.8}Mn_{0.2}O_3$ with 2 mol. % Nb additive (BNM8T2O+Nb). The XRD results and SEM morphologies found that the BNM8T2O+Nb exhibits a single phase with rhombohedral symmetry in space group of *R3c*. Moreover, the low temperature (< 30 K) remnant magnetization of the *M-H* loops and the ZFC-FC results indicate that BNM8T2O+NB possesses the low temperature ferromagnetic nature. The research of room-temperature multiferrocity on this single-phase ceramic reveals that the BNT based multiferroic is a valuable research direction for the new generation of magnetic-electric coupling devices.

Chapter VI Investigation of multiferroics ceramics behaviour of x(0.94Bi0.5Na0.5TiO3-0.06BaTiO3)-(1-x)BiFeyMn(1-y)O3

6.1 Multiferroics ceramics of $0.5(0.94Bi_{0.5}Na_{0.5}TiO_3\text{-}0.06BaTiO_3)\text{-}0.5BiFe_{0.8}Mn_{0.2}O_3$

6.1.1 Introduction

In 1865, James Clerk Maxwell revealed that the magnetic spin order and the electric charge motion are intrinsically coupled mutually, for which are thought to be completely independent initially.[206] The found of the mutual interaction between electric and magnetic provide researchers numerous novel explore directions such as multiferroics materials. Multiferroics materials are the compounds that show coexistence of ferroelectricity and ferromagnetism and coupling between them.[207] The magnetoelectric (ME) coupling signifies the magnetic field is capable of tuning the electric order and vice versa. The ME coupling makes it is highly anticipated to build new generation magnetoelectric random access memories (MERAMs) with low energy consumption and magnetoelectric sensors that capable for sensing extremely small magnetic field (pT scale) by reading electric signal and vice versa.[208-210] However, there are very few room temperature single phase multiferroics materials at present. The main reason is that the ferroelectricity and ferromagnetism are hardly origin from the same ion. As the empty *d* orbital is required for generating ferroelectricity while ferromagnetism order structure needs partially filled *d* orbital.[68,211] In this work, the novel composition of $0.5(0.94Bi_{0.5}Na_{0.5}TiO_3\text{-}0.06BaTiO_3)\text{-}0.5BiFe_{0.8}Mn_{0.2}O_3$ (50NBTB-50BF8M2O) has been selected to reveal the multiferroicity.

Trace back to the ferroelectric development history, the (1-x)$Bi_{0.5}Na_{0.5}TiO_3$-x$BaTiO_3$ (NBTB) based ceramics was initially explored in 1991 by Takenaka *et al.*[212-215] as the new candidate of lead-free ferroelectric ceramics. Especially for the NBTB composition at x = 0.06, which presents excellent dielectric properties, with high dielectric permittivity ~ 6000, high T_m ~ 570 K, reasonable coercive field ~ 30 kV/cm, large remnant polarization ~ 30 μC/cm under room temperature.[216] $BiFeO_3$ (BFO) is well-known as the very rare room temperature multiferroics with paramagnetic-antiferromagnetic transition temperature of T_N ~ 370 ºC and ferroelectric Curie temperature at T_C ~ 820 ºC. BFO shows spontaneous polarization of 100 μC/cm^2 on [111] direction and ~ 150 μC/cm^2 on [001] direction, respectively.[217,218] In terms of magnetic properties for BFO, it is antiferromagnetic with G-type spin configuration, each Fe^{3+} spins is surrounded by six antiparallel Fe spins ions and the spins are actually not perfect antiparallel.[65] This result in each pair of antiferromagnetic spin would produce a tiny net magnetic moment.[219] However, the tiny magnetic moment is macroscopically cancelled by a cycloidal spiral spin structure along antiferromagnetic axis with the wavelength period of 62 nm.[68,81] Therefore, in order to improve the magnetic state, twenty percent of Mn atoms were substituted by Fe atoms to create the magnetic moment differences in each pair of antiparallel magnetic spins. And the spin cycloid propagation period is expected to be modified to generate the macroscopic magnetic moment after doping.[220] In terms of the ME coupling mechanism, the excellent ferroelectric properties of NBTB is mainly contributed by Bi^{3+} ions.[221] And the stereo-chemical activity of Bi^{3+} 6s^2 lone pair electrons would also contributes to the Fe^{3+} ions displacement to further effect the magnetic spin order behaviour. Therefore, it is possible to form the ME coupling effect under ionic scale for this ceramic.[65,67,68,221] In this work, the single phase 50NBTB-50BF8M2O was successfully produced, and the characterizations of dielectric properties, room temperature of ME coupling was strictly confirmed.

6.1.2 Characterizations

Crystal structure determination and refinements

The density of each pellets was measured by Archimedes principle. X-ray diffraction (XRD) patterns for the ceramics were achieved by an X-ray diffractometer. The Rietveld refinement XRD data was scanned on the powder thoroughly ground from pellet, and the data of Rietveld refinement was analysed by the Rietveld method using the FullProf program.

Microstructural characterization

The microstructure of ceramic pellet was obtained by a scanning electron microscope (SEM). The morphology of the ferroelectric domains was observed by PFM at 70 kHz with a 10 V AC electric field, all the PFM scans were operated under room temperature. All the samples for SEM and PFM observation were etched under 900 ºC for 20 mins to reveal the grain boundaries.

Electrical property characterization

The temperature (-195 ºC to 600 ºC) and frequency (100 Hz to 10 MHz) dependence of dielectric permittivity, loss was measured by using an LCR meter. The polarization-current-electric field (P-I-E) hysteresis loops were captured by using a hysteresis tester at frequency of 10 Hz.

Magnetic property characterization

The magnetization hysteresis (M-H) loops and zero-field cooling and field cooling (ZFC-FC) data were all measured by superconducting quantum interference device magnetometer

(Quantum Design, a model MPMS (SQUID) VSM). The *M-H* loops were measured under temperature of 10 K, 20 K, 30 K and 285 K. The ZFC-FC data were measured from 10 K to 300 K. The *M-H* loops have been subtracted the paramagnetic contribution to reveal the pure ferromagnetism.

6.1.3 Results and discussions

Crystal structure characterization

The 50NBTB-50BF8M2O powder was refined by GSAS software shown as single phase can be indexed with a cubic lattice with the space group of Pm-3m, shows in Figure 6.1.[222] The parameters of XRD refinement is illustrated in Table 6.1, the low R_{wp} value of 50NBTB-50BF8M2O reveals the good fitting between the observed and calculated XRD patterns. Figure 6.2 illustrates the peak details correspond to 2θ=40° and 2θ=46.5°, respectively, shows two clear peaks of (111) and (200) without split. However, it can be noticed that for typical 0.94BNT-0.06BT, there would exist the peak split of (003)/(021) and (002)/(200) at 2θ = 40° and 46.5° that correspond to rhombohedral and tetragonal phase, respectively.[223] This phenomenon can be ascribed to BFMO and BNT-BT can form solid solution easily due to the similar structure between BFO (*R*3*c*)[224] and BNT-BT (*R*3*c*+*P*4*bm*)[216] under room temperature. This phenomenon is similar to the $NaNO_3$ (NN) doped 0.94BNT-0.06BT, the lattice symmetry changes to a pseudo-cubic structure with NN doping, and with NN content increase, the two split peaks disappeared gradually.[223]

Table 6.1 Rietveld refinement Structure Parameters by space group *Pm-3m* for 50NBTB-50BF8M2O

Space Group	Refined Lattice Parameters					Weighted Profile R-factor (W_{rp})	Goodness of fit (x^2)
Pm-3m	a (Å)	b (Å)	c (Å)	γ (°)	Volume (Å^3)	0.0989	2.990
	3.929195	3.929195	3.929195	90	60.661		

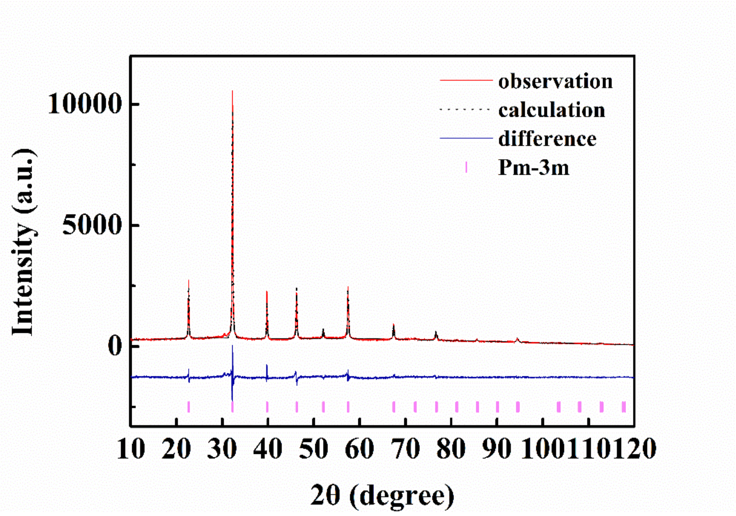

Figure 6.1 Rietveld XRD patterns refinement by GSAS of 50NBTB-50BF8M2O powders ground from disk modelled as non-polar phase of Pm/3m space group.

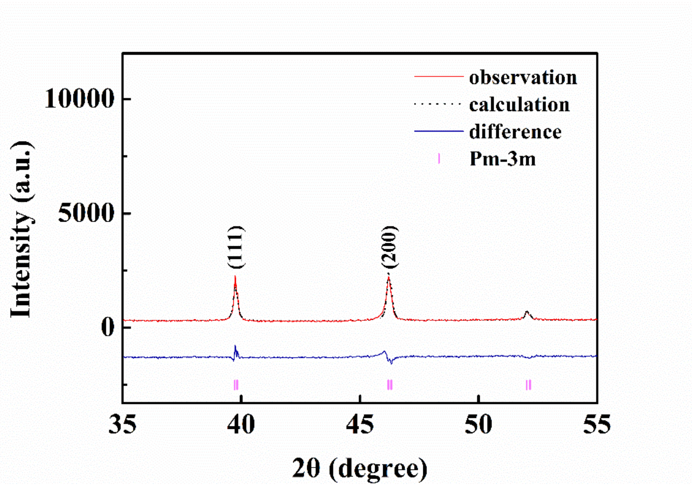

Figure 6.2 Rietveld XRD patterns refinement by GSAS of 50NBTB-50BF8M2O powder ground from disk modelled as non-polar phase of *Pm-3m* space group between 35° and 55°.

Figure 6.3 shows the scanning electron microscope morphology of 50NBTB-50BF8M2O ceramic. The cubic like grains was calculated by image J software with average grain size at around 4.72 μm, which is much larger than the grain size of pure 0.94BNT-0.06BT at around 0.91 μm reported by W X, Jia et al. That's because for the undoped 0.94BNT-0.06BT calcination, the volatilization of Na^+ promote the for of V_{Na}'-V_O''-V_{Na}' defects dipole for the sake of neutrality, the V_{Na}'-V_O''-V_{Na}' defects dipole may cause grain boundary pinning effect, which yielding small grains in pure NBTB.[223] However, in 50NBTB-50BF8M2O, Mn ions and Fe ions can suppress the form of V_{Na}'-V_O''-V_{Na}', as the high valence of Mn ions can compensate the loss of positive charge leaded by Na ions volatilization. The lower amount of V_{Na}'-V_O''-V_{Na}' lead to the less pinning effect during grain growth.[225,226]

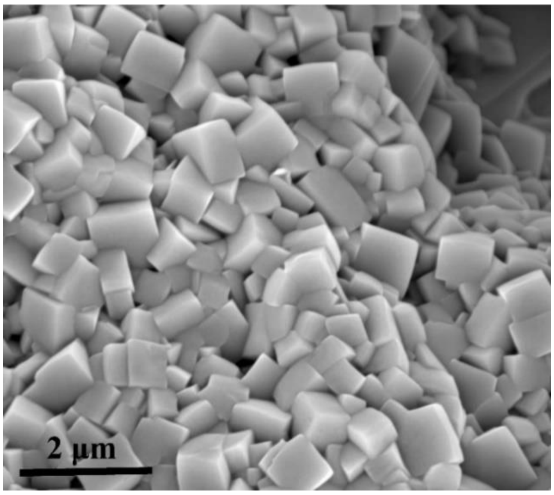

Figure 6.3 The morphology of 50NBTB-50BF8M2O ceramics.

Electrical properties characterization

The temperature (-195 ºC to 600 ºC) and frequency dependence on dielectric permittivity and loss tangent were depicted by Figure 6.4(a) and Figure 6.4(b). It could be found that the 50NBTB-50BF8M2O exhibit stable value of dielectric permittivity at low temperature (below -150 ºC), followed by a continuous increase to $\varepsilon' > 10^3$ when temperature above 75 ºC over all measurement frequencies. The tangent loss is extremely high over all measuring temperature range (-195 ºC to 600 ºC), which may attribute to the high leakage conductivity of BF8M2O. The anomalies of dielectric permittivity and tangent loss at around 450 ºC shown in Figure 6.4(b) is considered as the ferroelectric to paraelectric phase transition temperature.

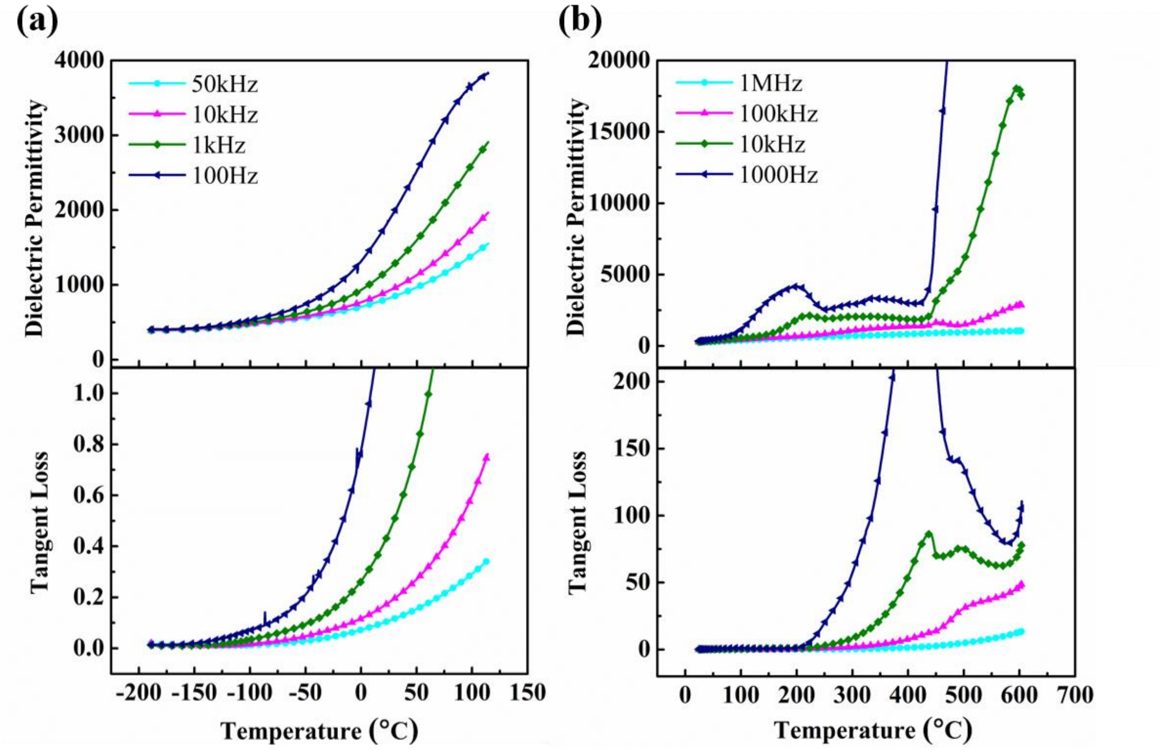

Figure 6.4 The temperature and frequencies dependence of dielectric permittivity and dielectric loss of 50NBTB-50BF8M2O ceramics.

The black and red lines in Figure 6.5 depict the polarization-electric field (*P*-*E*) and current-electric field (*I*-*E*) loops of the 50NBTB-50BF8M2O ceramics, respectively. The round-like shape *P*-*E* loops and linear-like *I*-*E* loops indicate 50NBTB-50BF8M2O possesses high current leakage.

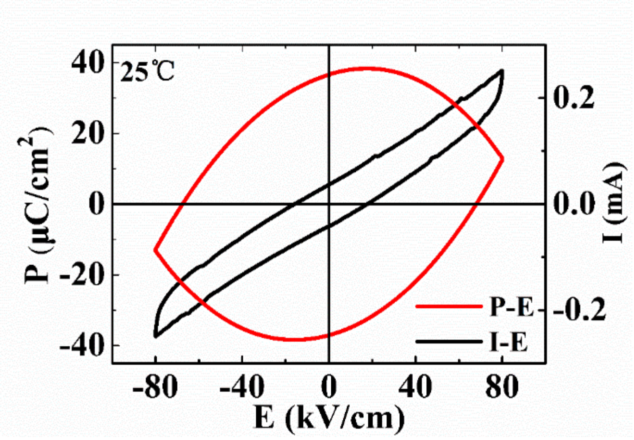

Figure 6.5 The *P-I-E* loops of pure 50NBTB-50BF8M2O ceramics.

To further investigate the leakage mechanism, the X-ray photoelectron spectroscopy (XPS) was performed for Fe 2p and Mn 2p in 50NBTB-50BF8M2O ceramics, calibrated by C 1s line (284.8 eV) binding energy, show by Figure 6.6.[227] The binding energy of Fe $2p_{3/2}$ is at 710.3 eV with an observed satellite peak 8.6 eV above this principle peak. Because the d orbital electron spin configuration between Fe^{2+} and Fe^{3+} are different, the Fe^{2+} and Fe^{3+} show satellite peak at 6 eV or 8 eV above their principle $2p_{3/2}$ peaks, respectively.[228] This Fe 2p XPS spectra of 50NBTB-50BF8M2O presents similar behaviour with the study on pure BFO, which denotes that Fe in 50NBTB-50BF8M2O is mainly as +3 valence state. Therefore, the contribution of leakage conductivity by Fe^{2+} has been excluded. Apart from the Fe ions, the doped Mn ions also easy to possess the mixed valence state in compounds. The binding energy for principle peak of Mn $2p_{3/2}$ is at 641.9 eV and an evident shoulder marked by blue arrow below the energy of principle peak can be observed, which indicate the Mn ions mainly exist as Mn^{4+} with small amount of Mn^{2+}.[228] Therefore, it can be confirmed that the mechanism of high leakage conductivity mainly ascribed to the existence of large amount of Mn^{4+} that lead to the corresponding free electrons carriers.

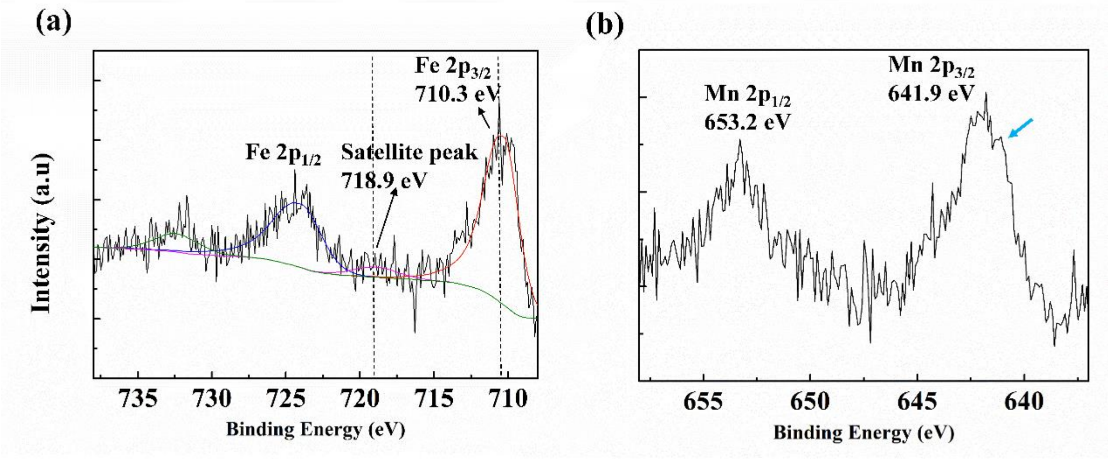

Figure 6.6 XPS spectra of (a) Fe 2p and (b) Mn 2p of 50NBTB-50BF8M2O ceramics.

Ferroelectric domain microstructure characterization

The local *P-E* loops captured by PFM shows in Figure 6.7, the green dot in Figure 6.7 (a) and Figure 6.7 (b) is the position where PFM polarization-electric field (*P-E*) hysteresis loops achieved. Figure 6.7 (c) presents the local *P-E* loops on green dot, the *P-E* loops were captured with a local AC electric field from -0.8 V to 0.8 V, the slim saturated local *P-E* loops indicate that the green area might be dominated by polar-nano regions (PNRs). The black curve in Figure 6.7(d) illustrates the height signal intensity, the differences between local *P-E* and the height signal intensity reveals that the local *P-E* signal is not from the signal induced by ceramic roughness.

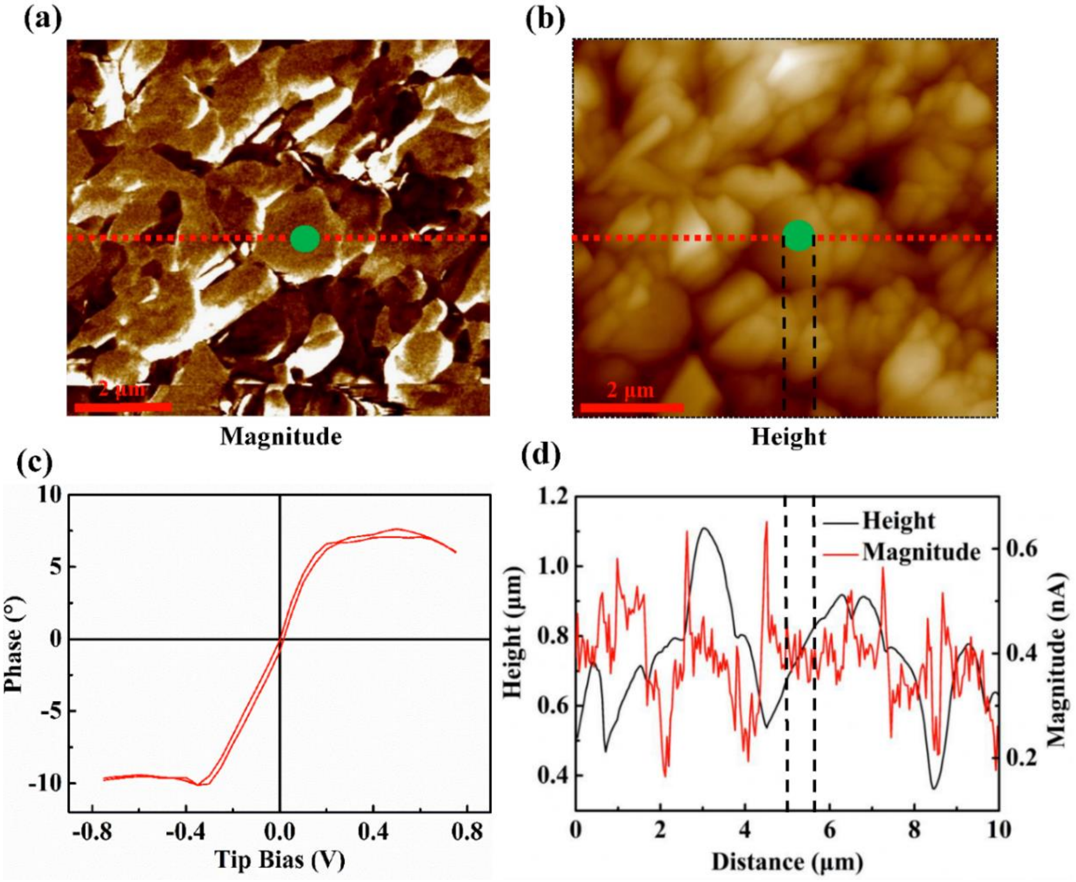

Figure 6.7 The local *P-E* loops captured by PFM of 50NBTB-50BF8M2O ceramics. (a) Polarization magnitude of this area, (b) topography of this area (c) the local *P-E* loops and (d) the polarization magnitude signal and height signal intensity along the red dashed line.

In order to observe the ferroelectric domains and its electric field tunability at room temperature, the ferroelectric domain switching behaviour were investigated using piezo-response force microscope (PFM) under an out of-plane electric field (Figure 6.8). Figure 6.8(a) and (b) illustrate the topography before and after poling. Figure 6.8(c) and Figure 6.8(d) depict the phase signal changes before and after poling, respectively. The unchanged topography reveals that the switching of phase signal all contributed by the polarizations. The poling area was marked within red area shown in Figure 6.8(c) and (d), the applied poling field was DC electric field at +30 V (+ represents the electric field applied from top to bottom perpendicular to ceramic surface) at red upper half rectangle and -30 V at red lower half rectangle, the poling duration is 30 s. It is found that the phase signal with most of the white area transfer to black and verse vice. The apparent contrast changes observed in the phase signals provide the evidence for electric field tuneable ferroelectric domain switching.

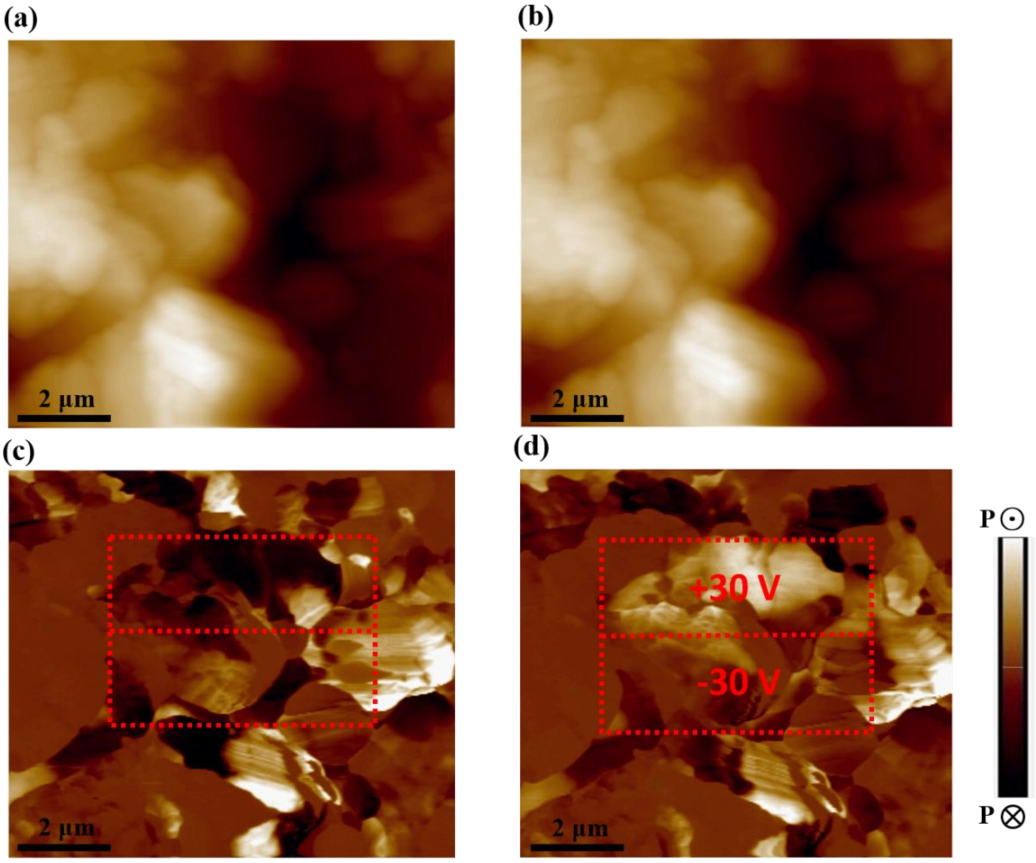

Figure 6.8 Ferroelectric domain switching under electric field of 50NBTB-50BF8M2O ceramics (a) topography and (c) vertical PFM phase signal under zero electric field; (b) topography and (d) vertical PFM phase signal after DC electric field (±30 V) for 30 s.

To further study the ferroelectric domain characteristics, the point electric field tuneable ferroelectric domain switching was also carried out by PFM. The DC electric field for poling was 30 V and applied from top to bottom and perpendicular to the sample surface under room temperature. The contrast on topography, magnitude and phase correspond to before and after poling states was shown by Figure 6.9. Figure 6.9(a1) and Figure 6.9(a2) present the topography before and after point poling, respectively, the position of point poling was marked by a red circle with a cross, it is clearly found that the topography shows no change after poling. The blue dotted line that cross the poling area are the regions for achieving magnitude and phase signals changes to reveal the polarization switching state at the point poling area, the signals are presented by Figure 6.9(d1) and Figure 6.9(d2), corresponding to the before and after poling area, respectively. The red curves in Figure 6.9(d1) and Figure 6.9(d2) that within green line regions indicate the magnitude increase after poling, which reveals that the point poling enlarges the domain size. Moreover, the black curves present the phase transition from positive to negative position, which indicates the polarization directed towards to the bottom electrode. Furthermore, the observed contrast of magnitude and phase also visually interpret the changes after poling, which are shown by Figure 6.9(b1) (b2) and Figure 6.9(c1) (c2), respectively. It is also noteworthy that for the area that without poling, the magnitude and phase signal and their observation just present slight changes after point poling, which denotes that this multiferroic not only presents the piezoelectric/ ferroelectric behaviour but also capable to be accurately tuned by external electric field.

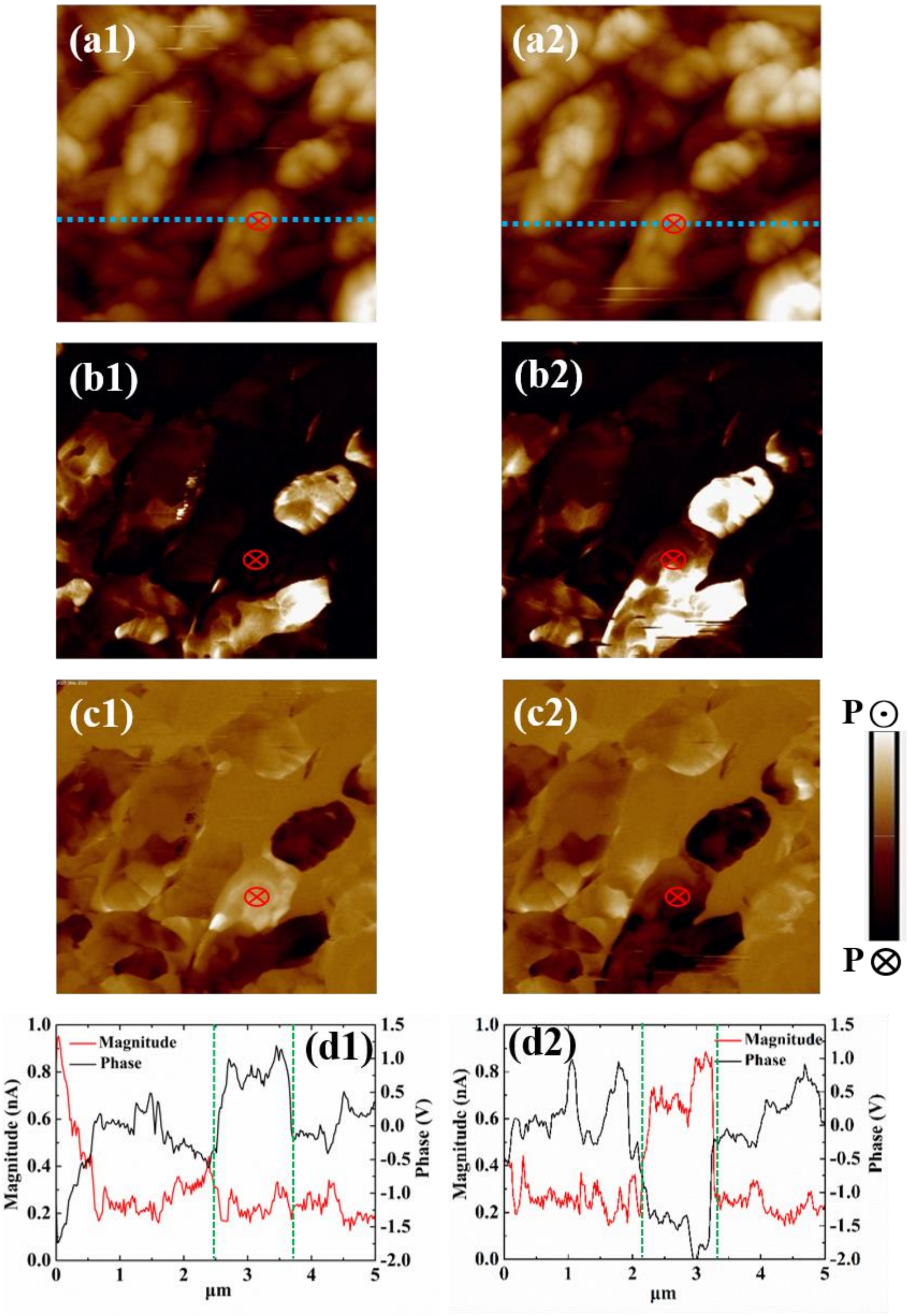

Figure 6.9 Ferroelectric domain switching by point poling of 50NBTB-50BF8M2O ceramics under PFM, the point poling area is marked by red circle with an across. The magnitude intensity and phase position on this point is achieved on the blue line to across the poling area. (a1) Topography before poling, (a2) topography after poling, (b1) vertical magnitude intensity before poling, (b2) vertical magnitude intensity after poling, (c1) vertical phase before poling, (c2) vertical phase after poling, (d1) the magnitude and phase signal intensity before point poling and (d2) the magnitude and phase signal intensity after point poling.

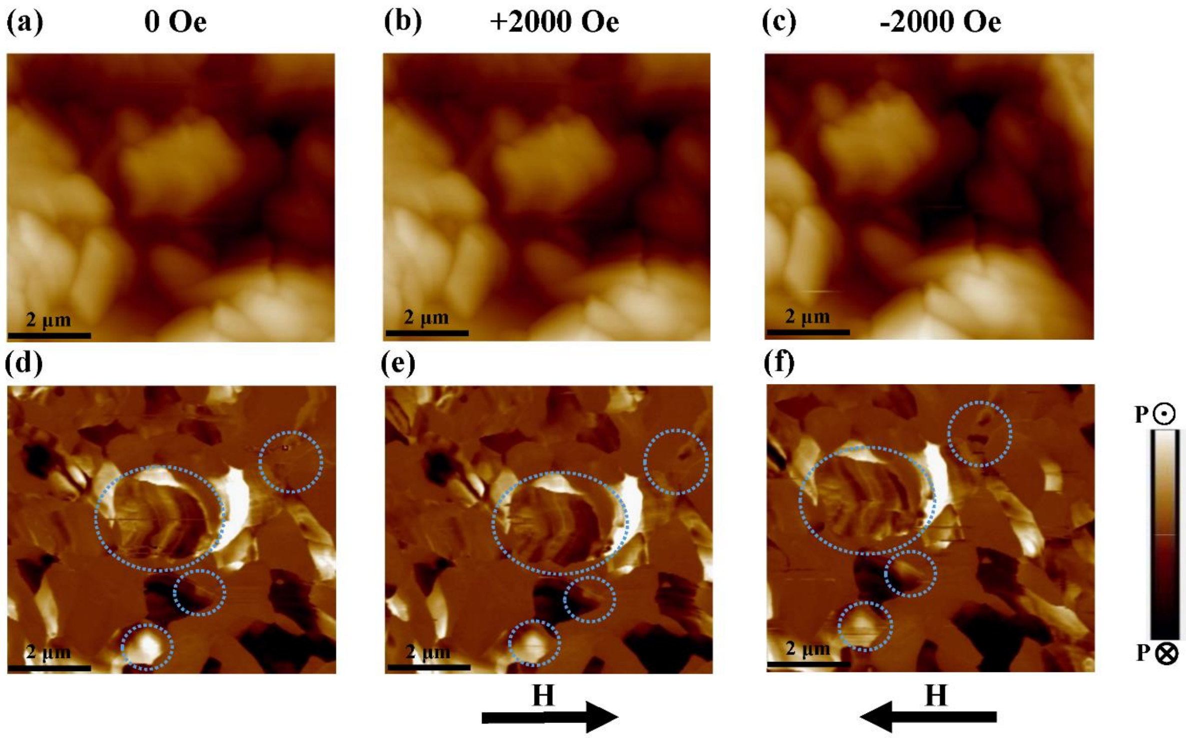

Figure 6.10 Ferroelectric domain switching under applied magnetic field of 50NBTB-50BF8M2O ceramics. (a) Topography and (d) vertical phase signal under 0 Oe H field; (b) topography and (e) vertical phase under +2000 Oe H field; (c) topography and (f) vertical phase signal under -2000 Oe H field.

The magnetic field induced ferroelectric domain switching was investigated by using PFM under an in-plane magnetic field (Figure 6.10) under room temperature. After positive (+2000 Oe) and negative (-2000 Oe) magnetic field were applied parallel to the sample surface, the direction of the ferroelectric polarization changed within the highlighted areas. This behaviour provided the evidence for the ferroelectric polarization is tuneable by magnetic field under room temperature.

Magnetic properties characterization

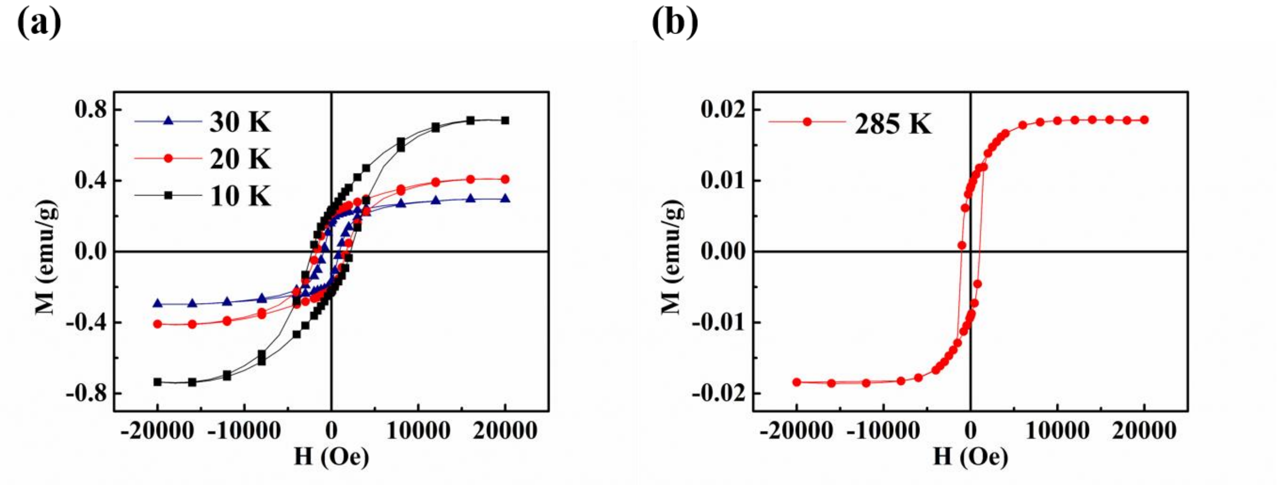

Figure 6.11 The magnetic field dependence of magnetization for 50NBTB-50BF8M2O ceramics under different temperature (a) 10 K, 20 K, 30 K and (b) 285 K.

The magnetic field dependence of magnetization for 50NBTB-50BF8M2O were measured by SQUID magnetometer at four temperature point of 10 K, 20 K, 30 K and 285 K, which were illustrated by Figure 6.11. The room temperature ferromagnetic nature is strongly supported by the well saturated *M-H* loops with a remnant magnetization at about 0.01 emu/g, shown by Figure 6.11 (b), where the paramagnetic contribution from substrate was subtracted. The origins of spontaneous magnetization are suspected because the 62 nm periodicity helical propagation is destroyed and the canted electron spin between Fe and Mn ions generate the net magnetic moment. The similar enhancement of magnetic properties on BFO by Mn substitution is also reported by Sunil *et al.* in 2012.[229] For the low temperature *M-H* loops, the remnant magnetization of 50NBTB-50BF8M2O increased dramatically, the remnant magnetization reaches approximately 0.23 emu/g at temperature of 10 K, as illustrated by Figure 6.11(a), where the paramagnetic contribution from substrate was also subtracted.

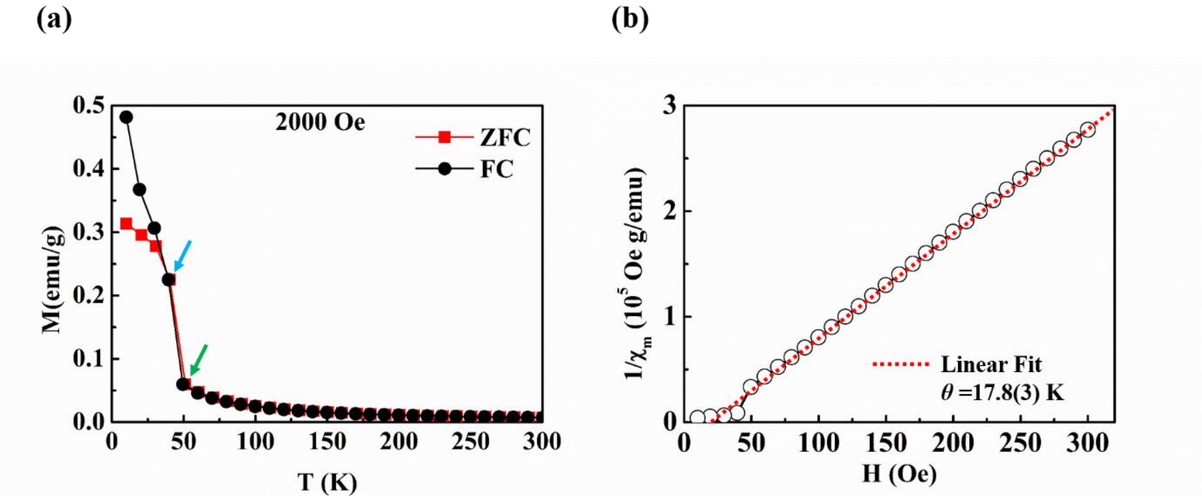

Figure 6.12 (a) Zero-field cooled (ZFC) and field cooled (FC) magnetization curves of 50NBTB-50BF8M2O ceramics. (b) The open circles represent temperature dependence of inverse magnetic susceptibility $1/\chi_m$ for 50NBTB-50BF8M2O. The red dotted line is the linear fitting part on the high temperature paramagnetic linear part of $1/\chi_m$ based on the Curie-Weiss law.

In order to study the nature magnetic order of 50NBTB-50BF8M2O. The zero-field cooled (ZFC) and field cooled (FC) magnetization curves were measured for 50NBTB-50BF8M2O from temperature 10 K to 300 K under 2000 Oe magnetic field, shown by Figure 6.12(a). When temperature below 40 K, see Figure 6.12 (a) blue arrow, there is a prominent bifurcation between ZFC and FC curves. This irreversibility in ZFC and FC is suggested for the presence of spin frustration or spin glass state at low temperatures, and the splitting temperature of 40 K, is defined as the freezing temperature for spin glass.[201,202,230] The bifurcation originates from the freezing temperature T_f under which spin glass cluster would be frozen and present the long-disorder state.[231] The ZFC measurement proceed by firstly zero magnetic field cooling down sample from 300 K to 10 K and then heat sample with magnetic field back to 300 K under 2000 Oe (the coercive magnetic field of this sample is about 1500 Oe at 10 K, see Figure 6.11), the magnetization value was collected during temperature increasing procedure. Therefore, since there is no magnetic field to align the spin-glass clusters towards specific direction during temperature decreasing procedure, the clusters would align randomly when the heating procedure start. Due to the freezing effect for spin clusters under freezing temperature (T_f),[231] the spin cluster rotation recover when temperature above T_f (~ 40 K). For the FC measurement, the sample was cooled down from 300 K to 10 K again with the same applied magnetic field of 2000 Oe and the magnetization data was collected simultaneously, therefore, the clusters align towards the magnetic field applied direction during cooling. Consequently, the magnetization bifurcation was caused by the magnetic moment difference between ZFC and FC below blocking temperature.

To further investigate the ferrimagnetic to paramagnetic phase transition temperature (T_c), the linear fitting regarding Curie Weiss law was taken on the high temperature paramagnetic part of temperature dependent inverse susceptibility ($1/\chi_m$), shown by Figure 6.12 (b) red dotted line, expressed as:[21,203]

$$\chi = \frac{C}{(T-\theta)} \tag{6.1}$$

where C is the Curie constant and θ is the paramagnetic Curie temperature, which has no actual physical meaning. The $1/\chi_m$ decrease linearly between 300 K and 50 K with temperature decrease and then suddenly drops below 50 K. This behaviour suggests the ferrimagnetic nature. The positive intercept of linear fitting function on x-axis, θ =17.8(3) K, further indicates the Curie transition at 17.8 K from ferrimagnetic to paramagnetic phase.[21,203] Combining with the ZFC-FC data and the observed well saturated M-H loops with apparent remnant magnetization under room temperature, suggesting that 50NBTB-50BF8M2O is the mixture of room-temperature ferromagnetic and low-temperature ferrimagnetic phase. The origins of ferrimagnetic nature at low temperature is suspected as the results of the net magnetic moment that created by the electrons spin magnetic moment difference between un-perfect antiparallel Mn ions and Fe ions and the destruction in the spiral spin structure.[229] The ferromagnetic nature at room temperature is suspected originates from the metallicity, the high leakage conductivity during the dielectric tests could also be ascribed to the presence of metallicity.

6.1.4 Summary

In this work, the structures, dielectricity, ferroelectricity and multiferrocity were strictly investigated for $0.5(0.94Bi_{0.5}Na_{0.5}TiO_3$-$0.06BaTiO_3)$-$0.5BiFe_{0.8}Mn_{0.2}O_3$. The XRD refinement results and SEM morphology indicate the $0.5(0.94Bi_{0.5}Na_{0.5}TiO_3$-$0.06BaTiO_3)$-$0.5BiFe_{0.8}Mn_{0.2}O_3$ is a single phase with pseudo-cubic symmetry in space group of *Pm-3m*. We successfully investigated its local *P-E* loops, electric-field and magnetic-field induced ferroelectric domain switching by using PFM. It is a solid evidence for very rare room-temperature observed ME coupling effect among multiferroicity research, to our best knowledge. Furthermore, the room-temperature ferromagnetic nature was also strongly confirmed by the apparent remnant magnetization in *M-H* loops, along with the characteristics of ZFC-FC results, which indicate that $0.5(0.94Bi_{0.5}Na_{0.5}TiO_3$-$0.06BaTiO_3)$-$0.5BiFe_{0.8}Mn_{0.2}O_3$ is the mixture of low temperature ferrimagnetic and room temperature ferromagnetic phase. The research of room-temperature multiferrocity on this single-phase ceramic reveals that the BNT-BT based multiferroic is an exploring worthy composition for the new generation of high sensitivity magnetic sensors or the low energy consumption memory devices.

6.2 The doping on $0.5(0.94Bi_{0.5}Na_{0.5}TiO_3$-$0.06BaTiO_3)$-$0.5BiFe_{0.8}Mn_{0.2}O_3$ multiferroics ceramics

6.2.1 Introduction

As the dielectric properties and polarization-current-electric field (*P-I-E*) loops shown in the chapter 6.1, the extremely high conductivity in $0.5(0.94Bi_{0.5}Na_{0.5}TiO_3$-$0.06BaTiO_3)$-$0.5BiFe_{0.8}Mn_{0.2}O_3$ (50NBTB-50BF8M2O) restricts its application on some specific conditions when high applied electric field is needed. In order to reduce the conductivity of pure 50NBTB-50BF8M2O, we tried to add two groups of additional elements (group I: 3 mol. % Nb, group II: 10 mol. % Na and 3 mol. % Bi) into $0.5(0.94Bi_{0.5}Na_{0.5}TiO_3$-$0.06BaTiO_3)$-$0.5BiFe_{0.8}Mn_{0.2}O_3$ to reduce its leakage conductivity. The 3 mol. % Nb element is to compensate the produced free electrons originate from the occurrence of Mn^{4+} that confirmed by XPS. The 10 mol. % Na and 3 mol. % Bi additions is to compensate the possible volatilization of Na and Bi ions during calcination and sintering. The A-site deficiency of Na/Bi ion would generate oxygen vacancies and increase the leakage conductivity. The determined excess amount of Na and Bi is by referring the similar excess amount in BNT system tried by Hongfen Ji in 2011.[232]

6.2.2 Characterizations

Crystal structure characterization

X-ray diffraction (XRD) patterns for the ceramics were achieved by an X-ray diffractometer (Panalytical Xpert Pro diffractometer using *CuKα* radiation).

Electrical properties characterization

The temperature (-195 ºC to 125 ºC) and frequency (100 Hz to 50 kHz) dependence of dielectric permittivity, loss was measured by using an LCR meter. The polarization-current-electric field (*P-I-E*) hysteresis loops were captured by using a hysteresis tester at frequency of 10 Hz.

6.2.3 Results and discussions

Crystal structure characterization

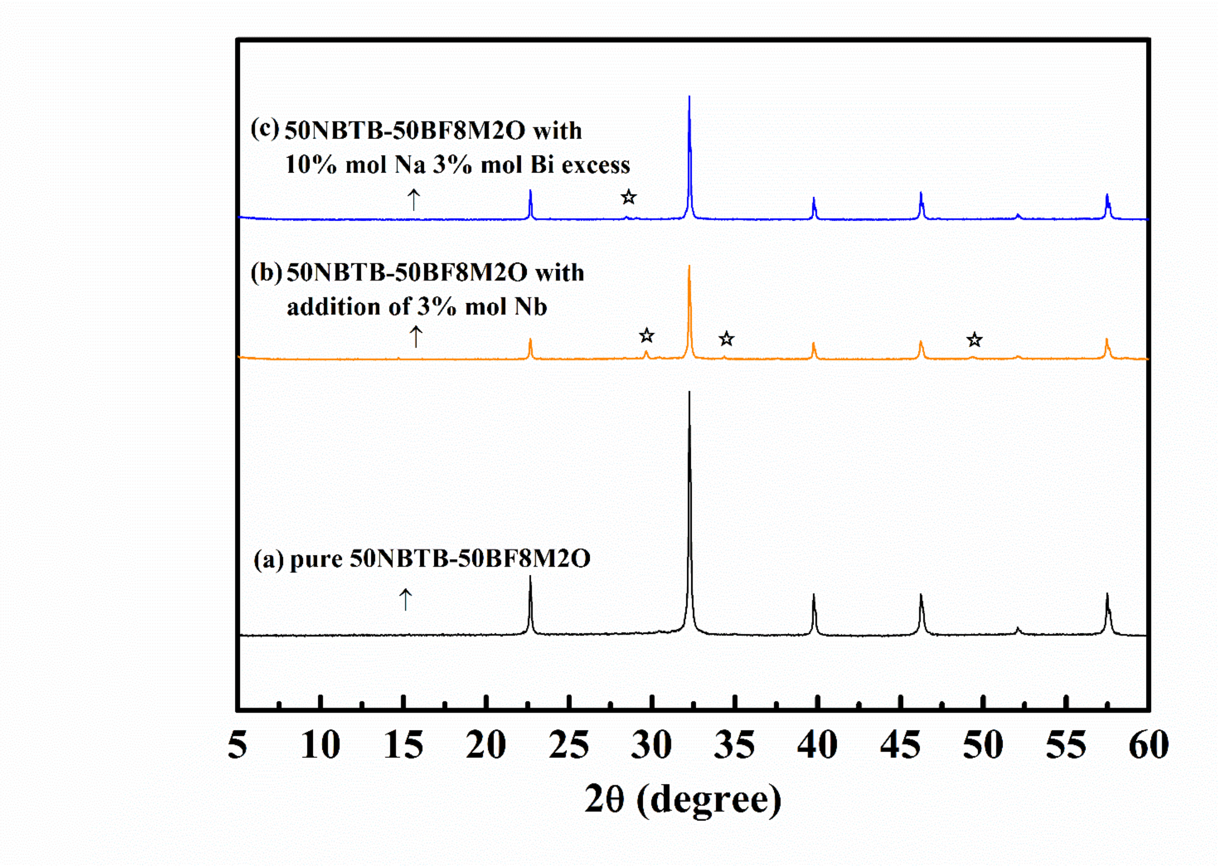

Figure 6.13 The XRD patterns for pure 50NBTB-50BF8M2O powders is represented by black curve. 50NBTB-50BF8M2O with 3 mol. % Nb excess powders is represented by orange curve. 50NBTB-50BF8M2O with 10 mol. % Na and 3 mol. % Bi excess powders is represented by blue curve. The open stars correspond to the XRD peaks of impurities.

Figure 6.13 shows the XRD results for 50NBTB-50BF8M2O, 50NBTB-50BF8M2O with 3 mol. % Nb excess, 50NBTB-50BF8M2O with 10 mol. % Na and 3 mol. % Bi excess, respectively. It is notable that the addition of Nb, Na and Bi all result in the generation of impurities.

Electrical properties characterization

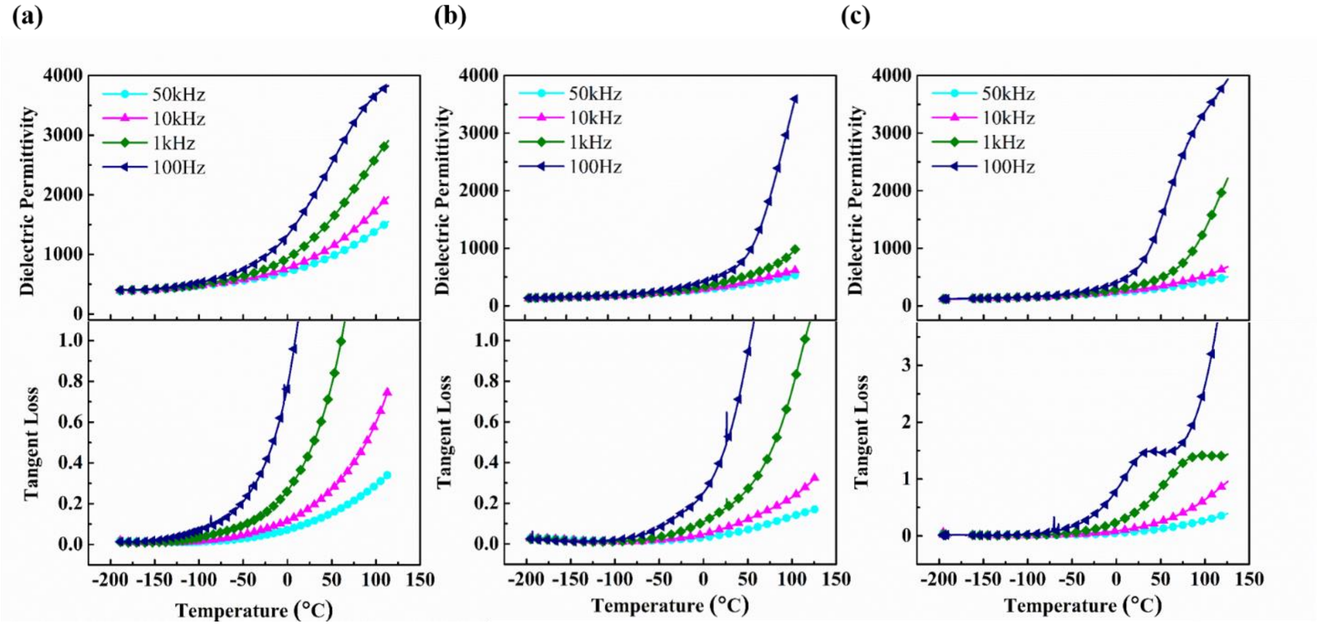

Figure 6.14 The temperature dependence of dielectric permittivity and loss tagent for (a) pure 50NBTB-50BF8M2O ceramics, (b) 50NBTB-50BF8M2O with 3 mol. % Nb excess ceramics and (c) 50NBTB-50BF8M2O with 10 mol. % Na and 3 mol. % Bi excess ceramics.

The temperature dependence (-195 ºC to 125 ºC) of dielectric permittivity and tangent loss for pure 50NBTB-50BF8M2O, 50NBTB-50BF8M2O with 3 mol. % Nb additive and 50NBTB-50BF8M2O with 10 mol. % Na and 3 mol. % Bi excess were shown by Figure 6.14(a) (b) (c), respectively. Comparing with the pure 50NBTB-50BF8M2O, the dielectric permittivity decreased in some extent and the tangent loss exhibits a slight decrease as well for the 50NBTB-50BF8M2O with 3 mol. % Nb additive composition. Even though the loss is still extremely high, however the slight reduction on tangent loss reveals that the leakage of 50NBTB-50BF8M2O is decreased by Nb additive. Figure 6.14(c) depicted the dielectric properties of BNTB-BF8M2O with 10 mol. % Na and 3 mol. % Bi excess. It is found that there are new maxima in tangent loss curves at frequencies of 100 Hz and 1 kHz, which could be suspected as impurity phase was produced after Na and Bi elements were doped into.

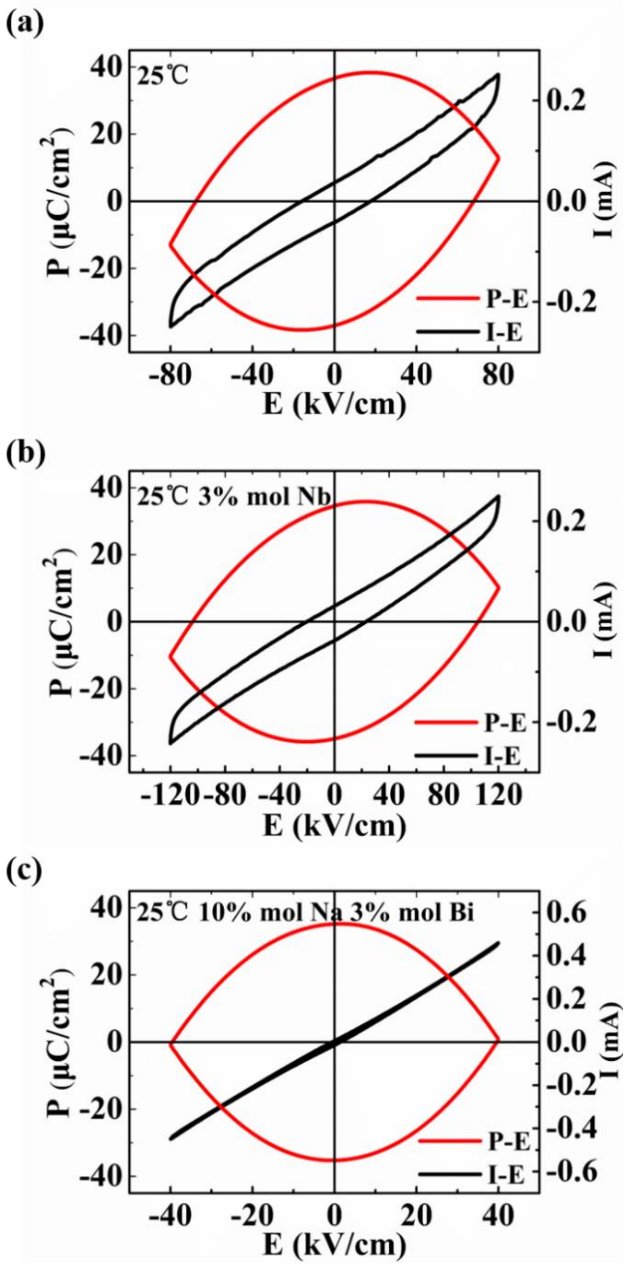

Figure 6.15 The *P-I-E* loops for (a) pure 50NBTB-50BF8M2O ceramics, (b) 50NBTB-50BF8M2O with 3 mol. % Nb excess ceramics and (c) 50NBTB-50BF8M2O with 10 mol. % Na and 3 mol. % Bi excess ceramics.

The room temperature electric field induced *P-E* and *I-E* loops of pure 50NBTB-50BF8M2O, 50NBTB-50BF8M2O with 3 mol. % Nb excess and 50NBTB-50BF8M2O with 10 mol. % Na and 3 mol. % Bi excess are shown by Figure 6.15(a) (b) (c), respectively. It is notable that the addition of Nb element raised the maximum applied electric field from 80 kV/cm to 120 kV/cm. However, the round shape *P-E* loops reveals that the high leakage still exists. For the composition with 10 mol. % Na and 3 mol. % Bi excess, it could be noted that the *I-E* loop is linear-like shape, which indicates that it is almost a conductor and the scheme of Na and Bi additive is non-effective.

As the XPS measurements shown in chapter 6.1, the Mn^{4+} is suggested as the main contribution for the high leakage conductivity. Therefore, the doping ions Nb^{5+}, could compensate the free electrons and further reduce the leakage apparently. The addition of Na and Bi is not effective reveals that the volatilization of Na and Bi element during sintering and calcination is negligible. Therefore, the over amount of Na and Bi will produce the impurities and result in the higher conductivity.

6.2.4 Summary

In this chapter, we tried to add two groups of addition elements (group I: 3 mol. % Nb, group II: 10 mol. % Na and 3 mol. % Bi) into $0.5(0.94Bi_{0.5}Na_{0.5}TiO_3\text{-}0.06BaTiO_3)\text{-}0.5BiFe_{0.8}Mn_{0.2}O_3$ to reduce its leakage conductivity. The achieved electric properties reveal that the additional Nb elements is slight effective on leakage conductivity reduction. The reason that additions of Nb could reduce the leakage conductivity apparently might owing to Nb can compensate the free electrons produced by the occurrence of Mn^{4+} ions. The addition of Na and Bi is not effective reveals that the volatilization of Na and Bi element during sintering and calcination is negligible.

6.3 The synthesis of $x(0.94Bi_{0.5}Na_{0.5}TiO_3\text{-}0.06BaTiO_3)\text{-}(1\text{-}x)BiFe_yMn_{(1\text{-}y)}O_3$ multiferroics

6.3.1 Introduction

Apart from the $0.5(0.94Bi_{0.5}Na_{0.5}TiO_3\text{-}0.06BaTiO_3)\text{-}0.5BiFe_{0.8}Mn_{0.2}O_3$ (50NBTB-50BF8M2O) that studied in chapter 6.1, we also tried to synthesis other composition with larger amount of magnetic element ratio based on $x(0.94Bi_{0.5}Na_{0.5}TiO_3\text{-}0.06BaTiO_3)\text{-}(1\text{-}x)BiFe_yM_{(1\text{-}y)}O_3$. The compositions are listed below:

(1) $0.5(0.94Bi_{0.5}Na_{0.5}TiO_3\text{-}0.06BaTiO_3)\text{-}0.5BiFe_{0.7}M_{0.3}O_3$ (50NBTB-50BF7M3O)

(2) $0.15(0.94Bi_{0.5}Na_{0.5}TiO_3\text{-}0.06BaTiO_3)\text{-}0.85BiFe_{0.8}M_{0.2}O_3$ (15NBTB-85BF8M2O)

(3) $0.15(0.94Bi_{0.5}Na_{0.5}TiO_3\text{-}0.06BaTiO_3)\text{-}0.85BiFe_{0.5}M_{0.5}O_3$ (15NBTB-85BF5M5O).

Unfortunately, no single phase can be acquired after vast number of synthesis under different ball milling and calcination conditions. In this chapter, the XRD with respect to each composition would be presented. It could be found that the impurities prone to be produced with magnetic element ratio increase.

6.3.2 Characterizations

Crystal structure characterization

X-ray diffraction (XRD) patterns for the ceramics were achieved by an X-ray diffractometer (Panalytical Xpert Pro diffractometer using *CuKα* radiation).

6.3.3 Results and discussions

Crystal structure characterization

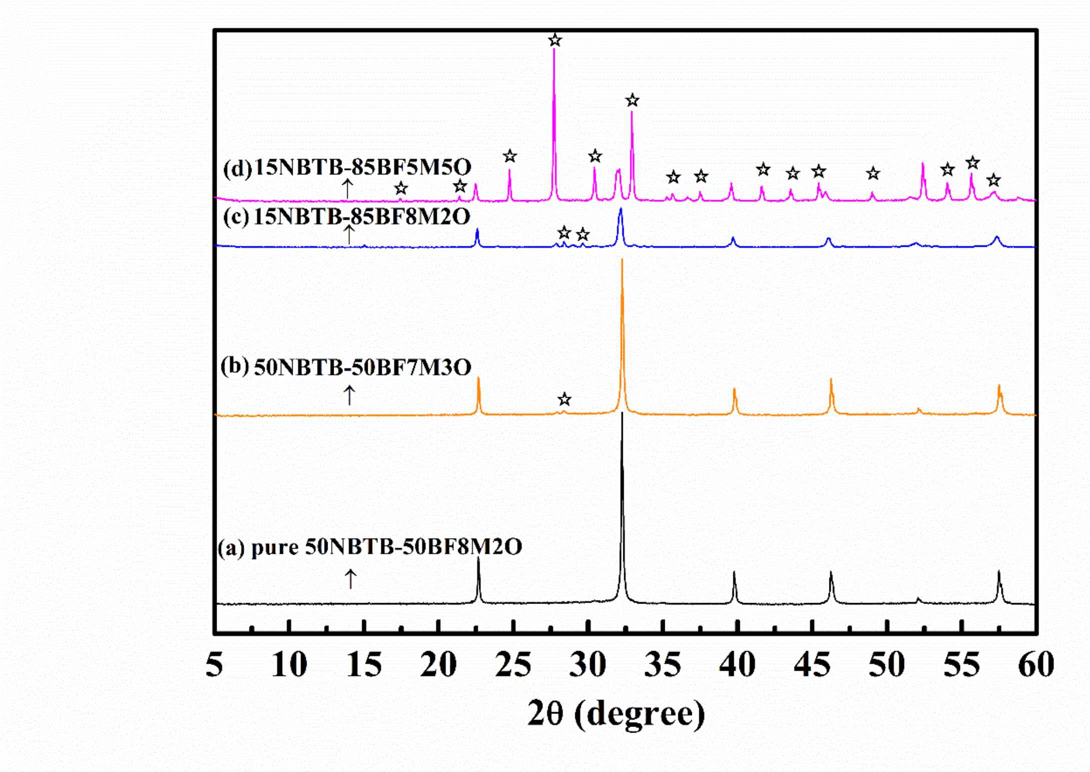

Figure 6.16 The XRD patterns for (a) pure 50NBTB-50BF8M2O powders with black curve, (b) 50NBTB-50BF7M3O powders with orange curve, (c) 15NBTB-85BF8M2O powders with blue curve and (d) 15NBTB-85BF5M5O powders with pink curve. The open stars correspond to the impurities XRD peaks.

Figure 6.16 shows the XRD results for pure 50NBTB-50BF8M2O, 50NBTB-50BF7M3O, 15NBTB-85BF8M2O, 15NBTB-85BF5M5O, and these open stars correspond to the impurities XRD peaks. It could be noted that with the amount of Mn increase, the impurities are produced more easily. We did a detailed check of the final products with each composition by Jade 6.5. And we found that the main phase of 15NBTB-85BF5M5O is $Bi_{12}MnO_{20}$ (BMO). BMO is a superparamagnetic material that possesses BCC crystal structure.[233] It is normally be synthesized under relatively low temperature (chemical route

~ 120 ºC, solid state ~ 700 ºC),[234,235] which result in the calcination temperature (725 ºC) of 15NBTB-85BF5M5O could producing BMO. The reason that the calcination temperature was kept at just 725 ºC is that with calcination temperature increased to ~ 740 ºC the products was apparently over-calcined. For the composition of 15NBTB-85BF8M2O and 50NBTB-50BF7M3O, the small amount of impurities phase is still not clear. However, it could be noted that the over-calcined temperature increase with the reduction of Mn ratio. The higher calcination temperature can thus be employed. The impurities decrease gradually. This could be ascribed to the melting point of MnO_2 is just 535 ºC, but the needed calcination temperature of BNT-based compound is above 1000 ºC, therefore, the lower Mn amount would increase the over-calcined temperature. However, the theoretical magnetic properties should also descend with the Mn amount decrease. Therefore, the research is mainly focus on the 50NBTB-50BF8M2O in Chapter 6.1.

6.3.4 Summary

The XRD results of different composition of NBTB based multiferroics indicate that the Mn content is really sensitive during synthesis in this system. It could be easily found that with Mn content increase, the impurities increase simultaneously. That's could be abscribed to the larger amount of MnO_2 further lowered the maximum calcination temperature to only 740 °C, in contrast to the NBTB-BF8M2O with less Mn content has a higher melting point and can be calcined at 1000 °C. The final product that possesses single phase structure and the largest amount of Mn simultaneously is $0.5(0.94Bi_{0.5}Na_{0.5}TiO_3\text{-}0.06BaTiO_3)\text{-}0.5BiFe_{0.8}Mn_{0.2}O_3$

Chapter VII Conclusions and future work

7.1 Conclusions

In this thesis, series of Aurivillius and perovskite structure based ferroelectric/multiferroics were successfully prepared. We carefully investigated their structures, dielectric and magnetic properties. The main discoveries are the field-induced phase transition behaviour for $Ba_2Bi_4Ti_5O_{18}$ (B2BT) ceramics, the low-temperature ferromagnetic nature for the ceramics for$Na_{0.5}Bi_{0.5}Ti_{0.8}Mn_{0.2}O_3$ with Nb doping (BNM8T2O+Nb) and the magnetic transition behavior from low temperature ferrimagnetic to room temperature ferromagnetic behavior of $0.5(0.94Bi_{0.5}Na_{0.5}TiO_3\text{-}0.06BaTiO_3)\text{-}0.5BiFe_{0.8}Mn_{0.2}O_3$ (50NBTB-50BF8M2O) ceramics.

For the exploration of ferroelectric, the main research was focused on Aurivillius structure B2BT ceramic that textured by Spark plasma sintering (SPS). We investigated its structure, dielectric and ferroelectric properties on in-plane and out of-plane directions. A diffused phase transition at around 240 °C was identified in the sample measured perpendicular [⊥] to as well as parallel [∥] to the SPS hot-pressing direction. In the *I-E* loops, four distinct current peaks were found for both the [⊥] and [∥] samples, which indicates the co-existence of weak and strong polar structures. And the transition between weak-polar structures and strong-polar structures can be proved by these two pairs of current peak with different amplitude. The observation of slim ferroelectric *P-E* hysteresis loops, the appearance of additional switching current peaks in the *I-E* loops and non-zero d_{33} piezoelectric coefficient (~ 0.4 pC/N for the B2BT [∥] ceramic) are considered as a strong evidence of the relaxor ferroelectric state in the B2BT ceramic.

In terms of the multiferroics ceramics, two types of single phase multiferroics compounds were sucessfully acquired after vast number of calcination and sintering explorations, which are $Na_{0.5}Bi_{0.5}Ti_{0.8}Mn_{0.2}O_3$ with 2 mol. % Nb additive (BNM8T2O+Nb) and $0.5(0.94Bi_{0.5}Na_{0.5}TiO_3\text{-}0.06BaTiO_3)\text{-}0.5BiFe_{0.8}Mn_{0.2}O_3$ (50NBTB-50BF8M2O).

For BNM8T2O+Nb, its structure, dielectric, ferroelectric and magnetic properties were strictly investigated. The XRD and SEM results indicate that the single phase BNM8T2O+NB ceramics possesses rhombohedral symmetry with space group of *R3c*. It suffers the relatively low ferroelectric properties due to high conductivity, which reflected by the round-shape room-temperature *P-E* loops. For the magnetic natures, the low temperature (< 30 K) remnant magnetization of the *M-H* loops and the ZFC-FC results indicate that BNM8T2O+NB presents the low temperature ferromagnetic nature ($T_c \sim 50$ K), which signifies that the magnetic elements has been successfully doped into this system. We also did the PFM observation on this composition, but no evidence of polarization switching under changing electric field or magnetic field was found.

For (50NBTB-50BF8M2O), the XRD refinement results and SEM morphology found that the (50NBTB-50BF8M2O) possesses single phase structure with pseudo-cubic symmetry in space group of *Pm-3m*. By measuring the frequencies and temperature dependence dielectric properties, we found that the curie transition point is suggested at around 440-450 °C. The macro P-E loops are similar with BNT8M2 with the round shape, which also indicate this composition suffers with the very high conductivity. However, we successfully investigated its local *P-E* loops, electric-field and magnetic-field induced ferroelectric domain switching by using PFM. And we acquired the local P-E loops under PFM. Moreover, we successfully observed the room-temperature visible ME coupling effect under PFM, the polarization switching is able be tuned by magnetic field. This is a very inspired result on multiferroics . The room-temperature ferrimagnetism was also strongly confirmed by the apparent remnant magnetization in *M-H* loops. Along with the ZFC-FC tests, these results indicate that $0.5(0.94Bi_{0.5}Na_{0.5}TiO_3\text{-}0.06BaTiO_3)\text{-}0.5BiFe_{0.8}Mn_{0.2}O_3$ possesses the temperature dependent magnetic transition from low temperature ferrimagnetic and high temperature ferromagnetic nature. This magnetic behaviour is very rare among magnetic materials, and even the first time found in multiferroics. This magnetic behaviour is very rare among magnetic materials, and even the first time found in multiferroics.

For these three different system researches, some behaviour that has never been reported was found, including the electric field induced phase transition of B2BT ceramic and the low temperature ferromagnetic nature of BNM8T2O+Nb ceramic. The most valuable behaviour is that the single phase 50NBTB-50BF8M2O ceramic possesses room-temperature multiferroicity and rare magnetic transition from low temperature ferrigmagnetic state to room temperature ferromagnetic state. This make it deserves more detailed work to further reveal its nature of intrinsic magneto-electric coupling effect and the origins of magnetic properties. These characterization on 50NBTB-50BF8M2O ceramic might point out a valuable direction for further multiferroics researches.

7.2 Future work

7.2.1 The research on the conductivity mechanism of $BiFeO_3$ (BFO)

The high conductivity is always an intractable problem for many types of multiferroics. One of the representatives is BFO. Both electron spin and metallicity could enhance the magnetic properties, but the large amount of free electron or metal may result in the huge conductivity and poor ferroelectricity. These two opposite characteristics may restrict the coexistence of ferroelectricity and magnetism. Therefore, to further study the conductivity of BFO is essentially necessary for building multiferroics with low conductivity but still possessing good magnetic properties.

7.2.2 Further exploration on $0.5(0.94Bi_{0.5}Na_{0.5}TiO_3\text{-}0.06BaTiO_3)\text{-}0.5BiFe_{0.8}Mn_{0.2}O_3$ ceramics

For the system of $0.5(0.94Bi_{0.5}Na_{0.5}TiO_3\text{-}0.06BaTiO_3)\text{-}0.5BiFe_{0.8}Mn_{0.2}O_3$, its magnetic properties are encouraged. However, lack of the Neutron diffraction characterization and first principle calculations limited the deep discussions on the magnetism origins. According to our previous results, , this composition is worthy for more detailed characterizations on how the magnetoelectric coupling effect works and why it possesses room-temperate ferrimagnetism and low-temperature ferromagnetism characteristic.

7.2.3 Creating sequence with magnetic element doping content changes

The XRD patterns in this study have already proved that the impurities are likely to be produced with magnetic doping content increase. However, the reality that single phase ceramics have been successfully synthesized open the possibility to create the more precise sequence of magnetic element content for doping to reveal the relationship between impurities phase and the content of magnetic element. This work will be helpful to reach the maximum magnetic doping content in order to achieve higher magnetic properties in the single phase multiferroics ceramics.

List of Publications

1. Cao Jun, Vladimir Koval, Hangfeng Zhang, Yunyin Lin, Jiyue Wu, Nan Meng, Yan Li, Zheng Li, Hongtao Zhang, and Haixue Yan. "Crystal structure and electrical properties of textured $Ba_2Bi_4Ti_5O_{18}$ ceramics." *Journal of the European Ceramic Society* 39, no. 4 (2019): 1042-1049. (First author)
   DOI: 10.1016/j.jeurceramsoc.2018.12.017
2. Li, Zheng, Wenzhi Qi, Jun Cao, Yan Li, Giuseppe Viola, and Haixue Yan. "Spark plasma sintering of grain-oriented $Sr_2Bi_4Ti_5O_{18}$ aurivillius phase ceramics." *Journal of Alloys and Compounds* 782 (2019): 6-9.
   DOI: 10.1016/j.jallcom.2018.12.175
3. Li, Zheng, Wenzhi Qi, Jun Cao, Yan Li, Giuseppe Viola, Chenglong Jia, and Haixue Yan. "Multiferroic properties of single phase Bi_3NbTiO_9 based textured ceramics." *Journal of Alloys and Compounds* (2019).
   DOI: 10.1016/j.jallcom.2019.02.241
4. Lin, Y., Patel, R., Cao, J., Tu, W., Zhang, H., Bilotti, E., Bastiaansen, C. W. M., Peijs, T. Glass-like transparent high strength polyethylene films by tuning drawing temperature. *Polymer* 2019.
   DOI: https://doi.org/10.1016/j.polymer.2019.03.036
5. Li Z, Tao K, Ma J, Gao Z, Koval V, Jiang C, Viola G, Zhang H, Mahajan A, Cao J, Cain M.
   $Bi_{3.25}La_{0.75}Ti_{2.5}Nb_{0.25}(Fe_{0.5}Co_{0.5})_{0.25}O_{12}$, a single phase room temperature multiferroic. *Journal of Materials Chemistry C*. 2018;6(11):2733-40.
   DOI: 10.1039/C8TC00161H

References

1 de Araujo, C. A. P., Cuchiaro, J. D., McMillan, L. D., Scott, M. C. & Scott, J. F. Fatigue-free ferroelectric capacitors with platinum electrodes. *Nature* **374**, 627, (1995).

2 Gajek, M. *et al.* Tunnel junctions with multiferroic barriers. *Nature Materials* **6**, 296, (2007).

3 Eerenstein, W., Mathur, N. D. & Scott, J. F. Multiferroic and magnetoelectric materials. *Nature* **442**, 759-765.

4 Nan, C.-W., Bichurin, M. I., Dong, S., Viehland, D. & Srinivasan, G. Multiferroic magnetoelectric composites: Historical perspective, status, and future directions. *Journal of Applied Physics* **103**, 031101, (2008).

5 Hill, N. A. Why are there so few magnetic ferroelectrics? *J. Phys. Chem. B* **104**, 6694-6709, (2000).

6 Khomskii, D. Classifying multiferroics: Mechanisms and effects. *Physics* **2**, (2009).

7 Carpenter, M. A. *et al.* Elastic and magnetoelastic relaxation behaviour of multiferroic (ferromagnetic + ferroelectric + ferroelastic) $Pb(Fe_{0.5}Nb_{0.5})O_3$ perovskite. *Journal of Physics: Condensed Matter* **27**, 285901, (2015).

8 Zhai, L.-J. & Wang, H.-Y. The magnetic and multiferroic properties in $BiMnO_3$. *Journal of Magnetism and Magnetic Materials* **426**, 188-194, (2017).

9 Muñoz, A. *et al.* The magnetic structure of $YMnO_3$ perovskite revisited. *Journal of Physics: Condensed Matter* **14**, 3285, (2002).

10 Li, Z. *et al.* $Bi_{3.25}La_{0.75}Ti_{2.5}Nb_{0.25}(Fe_{0.5}Co_{0.5})_{0.25}O_{12}$, a single phase room temperature multiferroic. *Journal of Materials Chemistry C* **6**, 2733-2740, (2018).

11 Haertling, G. H. Ferroelectric Ceramics: History and Technology. *Journal of the American Ceramic Society* **82**, 797-818, (1999).

12 Lines, M. E. & Glass, A. M. *Principles and applications of ferroelectrics and related materials*. (Oxford university press, 1977).

13 Damjanovic, D., Muralt, P. & Setter, N. Ferroelectric sensors. *IEEE sensors journal* **1**, 191-206, (2001).

14 Damjanovic, D. Ferroelectric, dielectric and piezoelectric properties of ferroelectric thin films and ceramics. *Reports on Progress in Physics* **61**, 1267, (1998).

15 Merz, W. J. Domain Formation and Domain Wall Motions in Ferroelectric $BaTiO_3$ Single Crystals. *Physical Review* **95**, 690-698, (1954).

16 Koch, E. Exchange Mechanisms. 7.15.

17 Lee, D. *et al.* Mixed Bloch-Néel-Ising character of 180° ferroelectric domain walls. *Physical Review B* **80**, 060102, (2009).

18 Fu, D. & Itoh, M. in *Ferroelectric Materials - Synthesis and Characterization* (ed Aime Pelaiz Barranco) Ch. 05 (InTech, 2015).

19 Fu, D. I., M. Role of Ca off-centering in tuning the ferroelectric phase transitions in Ba(Zr,Ti)O3 system. *arXiv preprint arXiv*.**00406**, 1503, (2015).

20 Sodipo, B. K. & Aziz, A. A. Recent advances in synthesis and surface modification of superparamagnetic iron oxide nanoparticles with silica. *Journal of Magnetism and Magnetic Materials* **416**, 275-291, (2016).

21 Petrovský, E. & Kapička, A. On determination of the Curie point from thermomagnetic curves. *Journal of Geophysical Research: Solid Earth* **111**, (2006).

22 Timm, C. Theory of magnetism. 4, (2011).

23 Bechlars, B. *et al.* High-spin ground states via electron delocalization in mixed-valence imidazolate-bridged divanadium complexes. *Nature Chemistry* **2**, 362, (2010).

24 Kittel, C. Physical Theory of Ferromagnetic Domains. *Reviews of Modern Physics* **21**, 541-583, (1949).

25 Fiebig, M., Lottermoser, T., Meier, D. & Trassin, M. The evolution of multiferroics. *Nature Reviews Materials* **1**, 16046, (2016).

26 Yoshinori, T., Shinichiro, S. & Naoto, N. Multiferroics of spin origin. *Reports on Progress in Physics* **77**, 076501, (2014).

27 Martin, L. W. *et al.* Multiferroics and magnetoelectrics: thin films and nanostructures. *Journal of Physics: Condensed Matter* **20**, 434220, (2008).

28 Van Aken, B. B., Palstra, T. T. M., Filippetti, A. & Spaldin, N. A. The origin of ferroelectricity in magnetoelectric $YMnO_3$. *Nature Materials* **3**, 164, (2004).

29 Ikeda, N. *et al.* Ferroelectricity from iron valence ordering in the charge-frustrated system $LuFe_2O_4$. *Nature* **436**, 1136, (2005).

30 Luo, Y. M., Zhou, C., Won, C. & Wu, Y. Z. Effect of Dzyaloshinskii–Moriya interaction on magnetic vortex. *AIP Advances* **4**, 047136, (2014).

31 Arima, T.-h. Ferroelectricity Induced by Proper-Screw Type Magnetic Order. *Journal of the Physical Society of Japan* **76**, 073702, (2007).

32 Bokov, A. A. & Emelyanov, S. M. Electrical properties of $Pb(Fe_{0.5}Nb_{0.5})O_3$ crystals. *physica status solidi (b)* **164**, K109-K112, (2006).

33 Raymond-Herrera, O., Font, R., S. Almodovar, N., Portelles, J. & Siqueiros, J. *Evidence of Magnetoelectric Coupling in* $Pb(Fe_{0.5}Nb_{0.5})O_3$ *Ceramics Through Impedance Spectroscopy and Electromechanical Resonance Measurements*. Vol. 1161 (2009).

34 Fraygola, B., Garcia, D. & Eiras, J. A. Anelastic Characterization of Pb(Fe2/3W1/3)O3 Multiferroic Ceramics. *Ferroelectrics* **428**, 87-93, (2012).

35 Smith, R. T., Achenbach, G. D., Gerson, R. & James, W. J. Dielectric Properties of Solid Solutions of $BiFeO_3$ with Pb(Ti, Zr)O3 at High Temperature and High Frequency. *Journal of Applied Physics* **39**, 70-74, (1968).

36 Caicedo Roque, J., Zapata, J., Gomez, M. & Prieto, P. *Magnetoelectric coefficient in $BiFeO_3$ compounds*. Vol. 103 (2008).

37 Sahu, J. R., Ghosh, A., Sundaresan, A. & Rao, C. N. R. Multiferroic properties of $ErMnO_3$. *Materials Research Bulletin* **44**, 2123-2126, (2009).

38 Fujimura, N., Takahashi, T., Yoshimura, T. & Ashida, A. Magnetic frustration behavior of ferroelectric ferromagnet $YbMnO_3$ epitaxial films. *Journal of Applied Physics* **101**, 09M107, (2007).

39 Lueken, H. *A magnetoelectric effect in $YMnO_3$ and $HoMnO_3$*. Vol. 47 (2008).

40 Staruch, M., Violette, D. & Jain, M. Structural and magnetic properties of multiferroic bulk $TbMnO_3$. *Materials Chemistry and Physics* **139**, 897-900, (2013).

41 Tong, P., Louca, D., Lee, N. & Cheong, S. W. Oxygen displacements and magnetoelectric coupling in $LuMnO_3$. *Physical Review B* **86**, 094419, (2012).

42 Fraygola, B. M., Coelho, A. d. A., Garcia, D. & Eiras, J. A. Magnetic and dielectric proprieties of multiferroic $(1\text{-}x)Pb(Fe_{2/3}W_{1/3})O_3$ $-xPbTiO_3$ Ceramics prepared via a modified two-stage solid-state reaction. *Materials Research* **14**, 434-441, (2011).

43 Khrustalyov, V. M., Savytsky, V. M. & Kharchenko, M. F. Magnetoelectric effect in antiferromagnetic $LiNiPO_4$ in pulsed magnetic fields. *Low Temperature Physics* **42**, 1126-1129, (2016).

44 Iguchi, Y. & Kohn, K. Magnetic symmetry of low-temperature phase of nickel-iodine-boracite $Ni_3B_7O_{13}I$. *Ferroelectrics* **137**, 225-233, (1992).

45 Iliev, M., G. Hadjiev, V., Mendoza, M. & Pascual, J. *Raman spectroscopy of multiferroic trigonal boracite $Co_3B_7O_{13}Cl$*. Vol. 76 (2007).

46 schmid, H. *Int. J. magnetism* **4**, 337, (1973).

47 Poole, A., Roessli, B., Zaharko, O. & Krämer, K. W. The magnetic structure of multiferroic $BaMnF_4$. *Journal of Physics: Condensed Matter* **23**, 266004, (2011).

48 Cox, D. E., Eibschütz, M., Guggenheim, H. J. & Holmes, L. Neutron Diffraction Study of the Magnetic Structure of $BaNiF_4$. *Journal of Applied Physics* **41**, 943-945, (1970).

49 EibschÜTz, M., Holmes, L., Guggenheim, H. J. & Cox, D. E. MAGNETIC BEHAVIOR OF THE TWO-DIMENSIONAL ANTIFERROMAGNET $BaFeF_4$. *J. Phys. Colloques* **32**, C1-759-C751-760, (1971).

50 Zajdel, P. *et al.* Structure and magnetism in the bond-frustrated spinel $ZnCr_2Se_4$. *Physical Review B* **95**, 134401, (2017).

51 Lunkenheimer, P., Fichtl, R., Hemberger, J., Tsurkan, V. & Loidl, A. Relaxation dynamics and colossal magnetocapacitive effect in $CdCr_2S_4$. *Physical Review B* **72**, 060103, (2005).

52 Tanaka, Y. *et al.* Incommensurate Orbital Modulation behind Ferroelectricity in $CuFeO_2$. *Physical Review Letters* **109**, 127205, (2012).

53 Frontzek, M. *et al.* Magnetic structure of $CuCrO_2$: a single crystal neutron diffraction study. *Journal of Physics: Condensed Matter* **24**, 016004, (2012).

54 Kubel, F. & Schmid, H. X-ray room temperature structure from single crystal data, powder diffraction measurements and optical studies of the aurivillius phase $Bi_5(Ti_3Fe)O_{15}$. *Ferroelectrics* **129**, 101-112, (1992).

55 Snedden, A., Hervoches, C. & Lightfoot, P. *Ferroelectric phase transitions in $SrBi_2Nb_2O_9$ and $Bi_5Ti_3FeO_{15}$: A powder neutron diffraction study*. Vol. 67 (2003).

56 Yang, J. *et al.* Magnetic and dielectric properties of Aurivillius phase $Bi_6Fe_2Ti_3O_{18}$ and the doped compounds. *Applied Physics Letters* **101**, 012402, (2012).

57 Yu. N. Venevtsev, G. Z., and S. Solov'ev. *Sov. Phys. Crystallogr* **4**, 538, (1960).

58 S. Kiselev, R. O., and G. Zhdanov. *Sov. Phys. Dokl.* **7**, 742.

59 Lebeugle, D. *et al.* Room-temperature coexistence of large electric polarization and magnetic order in $BiFeO_3$ single crystals. *Physical Review B* **76**, 024116, (2007).

60 Moreau, J. M., Michel, C., Gerson, R. & James, W. J. Ferroelectric $BiFeO_3$ X-ray and neutron diffraction study. *Journal of Physics and Chemistry of Solids* **32**, 1315-1320, (1971).

61 Belyaev, Y. Local Properties of the Sample Functions of Stationary Gaussian Processes. *Theory of Probability & Its Applications* **5**, 117-120, (1960).

62 Kubel, F. & Schmid, H. Structure of a ferroelectric and ferroelastic monodomain crystal of the perovskite $BiFeO_3$. *Acta Crystallographica Section B* **46**, 698-702, (2007).

63 Bucci, J. D., Robertson, B. K. & James, W. J. The precision determination of the lattice parameters and the coefficients of thermal expansion of $BiFeO_3$. *Journal of Applied Crystallography* **5**, 187-191, (1972).

64 Je-Geun, P., Manh Duc, L., Jaehong, J. & Sanghyun, L. Structure and spin dynamics of multiferroic $BiFeO_3$. *Journal of Physics: Condensed Matter* **26**, 433202, (2014).

65 Kubel, F. & Schmid, H. *Structure of a Ferroelectric and Ferroelastic Monodomain Crystal of the Perovskite $BiFeO_3$*. Vol. 46 (1990).

66 Ravindran, P., Vidya, R., Kjekshus, A., Fjellvåg, H. & Eriksson, O. Theoretical investigation of magnetoelectric behavior in $BiFeO_3$. *Physical Review B* **74**, 224412, (2006).

67 Palewicz, A., Przeniosło, R., Sosnowska, I. & Hewat, A. W. Atomic displacements in $BiFeO_3$ as a function of temperature: neutron diffraction study. *Acta Crystallographica Section B* **63**, 537-544, (2007).

68 Catalan, G. & Scott, J. F. Physics and Applications of Bismuth Ferrite. *Advanced Materials* **21**, 2463-2485, (2009).

69 Teague, J. R., Gerson, R. & James, W. J. Dielectric hysteresis in single crystal $BiFeO_3$. *Solid State Communications* **8**, 1073-1074, (1970).

70 Neaton, J. B., Ederer, C., Waghmare, U. V., Spaldin, N. A. & Rabe, K. M. First-principles study of spontaneous polarization in multiferroic $BiFeO_3$. *Physical Review B* **71**, 014113, (2005).

71 Ravindran, P., Vidya, R., Kjekshus, A., Fjellvåg, H. & Eriksson, O. Theoretical investigation of magnetoelectric behavior in $\mathrm{Bi}\mathrm{Fe}{\mathrm{O}}_{3}$. *Physical Review B* **74**, 224412, (2006).

72 Lebeugle, D., Colson, D., Forget, A. & Viret, M. Very large spontaneous electric polarization in $BiFeO_3$ single crystals at room temperature and its evolution under cycling fields. *Applied Physics Letters* **91**, 022907, (2007).

73 Lobo, R. P. S. M., Moreira, R. L., Lebeugle, D. & Colson, D. Infrared phonon dynamics of a multiferroic $BiFeO_3$ single crystal. *Physical Review B* **76**, 172105, (2007).

74 Cazayous, M., Malka, D., Lebeugle, D. & Colson, D. Electric field effect on $BiFeO_3$ single crystal investigated by Raman spectroscopy. *Applied Physics Letters* **91**, 071910, (2007).

75 Shvartsman, V. V., Kleemann, W., Haumont, R. & Kreisel, J. Large bulk polarization and regular domain structure in ceramic $BiFeO_3$. *Applied Physics Letters* **90**, 172115, (2007).

76 Wang, J. *et al.* Epitaxial $BiFeO_3$ Multiferroic Thin Film Heterostructures. *Science* **299**, 1719, (2003).

77 N. N. Krainik, N. P. K., V. V. Zhdanova, and V. A. Evseev. *Sov. Phys. Solid State* **8**, 654, (1966).

78 Lu, J. *et al.* On the room temperature multiferroic $BiFeO_3$: magnetic,dielectric and thermal properties. *The European Physical Journal B* **75**, 451-460, (2010).

79 Jun, L. *et al.* Magnetic susceptibility, phonons and dielectric constant of single crystalline $BiFeO_3$. *Journal of Physics: Conference Series* **200**, 012106, (2010).

80 Lee, S., Ratcliff, W., Cheong, S. W. & Kiryukhin, V. Electric field control of the magnetic state in $BiFeO_3$ single crystals. *Applied Physics Letters* **92**, 192906, (2008).

81 Sosnowska, I., Neumaier, T. P. & Steichele, E. Spiral magnetic ordering in bismuth ferrite. *Journal of Physics C: Solid State Physics* **15**, 4835, (1982).

82 Lebeugle, D. *et al.* Electric-Field-Induced Spin Flop in $BiFeO_3$ Single Crystals at Room Temperature. *Physical Review Letters* **100**, 227602, (2008).

83 Scott, J. F., Singh, M. K. & Katiyar, R. S. Critical phenomena at the 140 and 200 K magnetic phase transitions in $BiFeO_3$. *Journal of Physics: Condensed Matter* **20**, 322203, (2008).

84 Ederer, C. & Spaldin, N. A. Weak ferromagnetism and magnetoelectric coupling in bismuth ferrite. *Physical review. B, Condensed matter and materials physics* **71**.

85 Tabares-Muñoz, C., Rivera, J. P., Bezinges, A., Monnier, A. & Schmid, H. Measurement of the Quadratic Magnetoelectric Effect on Single Crystalline $BiFeO_3$. *Japanese Journal of Applied Physics* **24**, 1051, (1985).

86 Kadomtseva, A. M., Zvezdin, A. K., Popov, Y. F., Pyatakov, A. P. & Vorob'ev, G. P. Space-time parity violation and magnetoelectric interactions in antiferromagnets. *JETP letters* **79**, 571-581.

87 Singh, A., Pandey, V., Kotnala, R. K. & Pandey, D. Direct evidence for multiferroic magnetoelectric coupling in $0.9BiFeO_3$-$0.1BaTiO_3$. *Physical review letters* **101**.

88 Murashov, V. A. *et al.* Magnetoelectric (Bi, Ln)FeO_3 compounds: Crystal growth, structure and properties. *Ferroelectrics* **162**, 11-21, (1994).

89 Irie, H., Miyayama, M. & Kudo, T. Structure dependence of ferroelectric properties of bismuth layer-structured ferroelectric single crystals. *Journal of Applied Physics* **90**, 4089-4094, (2001).

90 Newnham, R. E., Wolfe, R. W. & Dorrian, J. F. Structural basis of ferroelectricity in the bismuth titanate family. *Materials Research Bulletin* **6**, 1029-1039, (1971).

91 Irie, H., Miyayama, M. & Kudo, T. Electrical properties of a bismuth layer-structured $Ba_2Bi_4Ti_5O_{18}$ single crystal. *Journal of the American Ceramic Society* **83**, 2699-2704, (2000).

92 Li, Z. *et al.* $Bi_{3.25}La_{0.75}Ti_{2.5}Nb_{0.25}(Fe_{0.5}Co_{0.5})_{0.25}O_{12}$*, a single phase room temperature multiferroic*. Vol. 6 (Journal of Materials Chemistry C, 2018).

93 Yan, H. *et al.* A lead-free high-curie-point ferroelectric ceramic, $CaBi_2Nb_2O_9$. *Advanced Materials* **17**, 1261-1265, (2005).

94 Van Den Boomgaard, J., R. Terrell, D., A. J. Born, R. & F. J. I. Giller, H. *An In-Situ Grown Eutectic Magnetoelectric Composite Material, Part 1: Composition and Unidirectional Solidification*. Vol. 9 (1974).

95 Van Den Boomgaard, J., Van Run, A. M. J. G. & Suchtelen, J. V. Magnetoelectricity in piezoelectric-magnetostrictive composites. *Ferroelectrics* **10**, 295-298, (1976).

96 van den Boomgaard, J. & Born, R. A. J. A sintered magnetoelectric composite material $BaTiO_3$-Ni(Co, Mn)Fe_2O_4. *Journal of Materials Science* **13**, 1538-1548, (1978).

97 Mahajan, R. P., Patankar, K. K., Kothale, M. B. & Patil, S. A. Conductivity, dielectric behaviour and magnetoelectric effect in copper ferrite-barium titanate composites. *Bulletin of Materials Science* **23**, 273-279, (2000).

98 Newnham, R. E., Skinner, D. P. & Cross, L. E. Connectivity and piezoelectric-pyroelectric composites. *Materials Research Bulletin* **13**, 525-536, (1978).

99 Nan, C.-W. Physics of inhomogeneous inorganic materials. *Progress in Materials Science* **37**, 1-116, (1993).

100 Manfred, F. Revival of the magnetoelectric effect. *Journal of Physics D: Applied Physics* **38**, R123, (2005).

101 Getman, I. Magnetoelectric composite materials: Theoretical approach to determine their properties. *Ferroelectrics* **162**, 45-50, (1994).

102 Van Run, A. M. J. G., Terrell, D. R. & Scholing, J. H. An in situ grown eutectic magnetoelectric composite material. *Journal of Materials Science* **9**, 1710-1714, (1974).

103 van den Boomgaard, J. & Born, R. A. J. A sintered magnetoelectric composite material BaTiO3-Ni(Co, Mn) Fe2O4. *Journal of Materials Science* **13**, 1538-1548, (1978).

104 Van Den Boomgaard, J., Terrell, D. R., Born, R. A. J. & Giller, H. F. J. I. An in situ grown eutectic magnetoelectric composite material. *Journal of Materials Science* **9**, 1705-1709, (1974).

105 Dai, Y. R. *et al.* Internal friction study on $CuFe_2O_4$-$PbZr_{0.53}Ti_{0.47}O_3$ composites. *Journal of Applied Physics* **96**, 5687-5690, (2004).

106 Liu, X.-M., Fu, S.-Y. & Huang, C.-J. Synthesis and magnetic characterization of novel $CoFe_2O_4$–$BiFeO_3$ nanocomposites. *Materials Science and Engineering: B* **121**, 255-260, (2005).

107 Mori, K. & Wuttig, M. Magnetoelectric coupling in Terfenol-D/polyvinylidenedifluoride composites. *Applied Physics Letters* **81**, 100-101, (2002).

108 Lu, M.-C. *et al.* Enhancing the magnetoelectric response of Terfenol-D/polyvinylidene fluoride/Terfenol-D laminates by exploiting the shear mode effect. *Applied Physics Letters* **106**, 112905, (2015).

109 Venkata Ramanaa, M. *et al.* Enhanced mangnetoelectric voltage in multiferroic particulate $Ni_{0.83}Co_{0.15}Cu_{0.02}Fe_{1.9}O_{4-\delta}$/$PbZr_{0.52}Ti_{0.48}O_3$ composites – dielectric, piezoelectric and magnetic properties. *Current Applied Physics* **9**, 1134-1139, (2009).

110 Sandlund, L. *et al.* Magnetostriction, elastic moduli, and coupling factors of composite Terfenol-D. *Journal of Applied Physics* **75**, 5656-5658, (1994).

111 Koon, N. C., Williams, C. M. & Das, B. N. Giant magnetostriction materials. *Journal of Magnetism and Magnetic Materials* **100**, 173-185, (1991).

112 Kyōkai, M. K. G. *Proceedings of the Tenth International Workshop on Rare-Earth Magnets and Their Applications, 16-19 May 1989, Kyoto International Conference Hall, Japan*. (Society of Non-Traditional Technology, 1989).

113 Moffett, M. B. *et al.* Characterization of Terfenol-D for magnetostrictive transducers. *The Journal of the Acoustical Society of America* **89**, 1448-1455, (1991).

114 IEEE Standard on Magnetostrictive Materials: Piezomagnetic Nomenclature. *IEEE Std 319-1990*, 1, (1991).

115 Clark, A. E., Teter, J. P. & McMasters, O. D. Magnetostriction "jumps" in twinned $Tb_{0.3}Dy_{0.7}Fe_{1.9}$. *Journal of Applied Physics* **63**, 3910-3912, (1988).

116 Clark, A., Spano, M. & Savage, H. Effect of stress on the magnetostriction and magnetization of rare earth-$Re_{1.95}$ alloys. *IEEE Transactions on Magnetics* **19**, 1964-1966, (1983).

117 Kang, G.-d. & Cao, Y.-m. Application and modification of poly(vinylidene fluoride) (PVDF) membranes – A review. *Journal of Membrane Science* **463**, 145-165, (2014).

118 Sirohi, J. & Chopra, I. *Fundamental Understanding of Piezoelectric Strain Sensors*. Vol. 11 (2000).

119 Guerra, G., Karasz, F. E. & MacKnight, W. J. On blends of poly(vinylidene fluoride) and poly(vinyl fluoride). *Macromolecules* **19**, 1935-1938, (1986).

120 Ekramul, K., Khatun, M., Nasrin, L., Mustafa, J. R. & Rahman, M. Pure β -phase formation in polyvinylidene fluoride (PVDF)-carbon nanotube composites. *Journal of Physics D: Applied Physics* **50**, 163002, (2017).

121 Zhang, D., Wang, M. & Sun, K. Low Frequency Noise Characterization and Signal-to-Noise Ratio Optimization for Silicon Hall Cross Sensors. *IEEE Journal of the Electron Devices Society* **3**, 365-370, (2015).

122 Range, S. K. d. Gravity Probe B: Exploring Einstein's Universe with Gyroscopes. *NASA* **26**, (2004).

123 Xing, Z., Li, J. & Viehland, D. Noise and scale effects on the signal-to-noise ratio in magnetoelectric laminate sensor/detection units. *Applied Physics Letters* **91**, 182902, (2007).

124 Cong, F. *et al.* Significant reduction of equivalent magnetic noise by in-plane series connection in magnetoelectric Metglas/Mn-doped $Pb(Mg_{1/3}Nb_{2/3})O_3$-$PbTiO_3$ laminate composites. *Journal of Physics D: Applied Physics* **48**, 465002, (2015).

125 Equivalent magnetic noise in magnetoelectric Metglas/$Pb(Mg_{1/3}Nb_{2/3})O_3$-$PbTiO_3$ laminate composites. *physica status solidi (RRL) – Rapid Research Letters* **5**, 232-234, (2011).

126 Paluszek, M. *et al. Magnetoelectric composites for medical application*. (2015).

127 Lenz, J. & Edelstein, S. Magnetic sensors and their applications. *IEEE Sensors Journal* **6**, 631-649, (2006).

128 Luo, L. *et al.* Effects of Mn doping on dielectric and piezoelectric properties of $0.71Pb(Mg_{1/3}Nb_{2/3})O_3$–$0.29PbTiO_3$ single crystals. *Applied Physics Letters* **90**, 102907, (2007).

129 Zuo, Z. J. *et al.* Multiplied magnetoelectric effect in multi-faceted magnetoelectric composite. *Applied Physics Letters* **104**, 032906, (2014).

130 Gun Lee, D. *et al.* Ultra-sensitive magnetoelectric microcantilever at a low frequency. *Applied Physics Letters* **101**, 182902, (2012).

131 Kaushik, A., Jayant, R. D., Sagar, V. & Nair, M. The potential of magneto-electric nanocarriers for drug delivery. *Expert opinion on drug delivery* **11**, 1635-1646, (2014).

132 Guduru, R. *et al.* Magneto-electric Nanoparticles to Enable Field-controlled High-Specificity Drug Delivery to Eradicate Ovarian Cancer Cells. *Scientific Reports* **3**, 2953, (2013).

133 Ho, S. Y. & Mittal, G. S. Electroporation of cell membranes: A Review. *Critical Reviews in Biotechnology* **16**, 349-362, (1996).

134 Nair, M. *et al.* Externally controlled on-demand release of anti-HIV drug using magneto-electric nanoparticles as carriers. *Nature Communications* **4**, 1707, (2013).

135 Liu, M. & Sun, N. X. Voltage control of magnetism in multiferroic heterostructures. *Philosophical transactions. Series A, Mathematical, physical, and engineering sciences* **372**, 20120439, (2014).

136 Vopson, M. M. Fundamentals of Multiferroic Materials and Their Possible Applications. *Critical Reviews in Solid State and Materials Sciences* **40**, 223-250, (2015).

137 Nogués, J. & Schuller, I. K. Exchange bias. *Journal of Magnetism and Magnetic Materials* **192**, 203-232, (1999).

138 Kiwi, M., Mejía-López, J., Portugal, R. D. & Ramírez, R. Positive exchange bias model: Fe/FeF_2 and Fe/MnF_2 bilayers. *Solid State Communications* **116**, 315-319, (2000).

139 Dong Sining, H. X., Li Xiaoguang. Research progress on exchange bias effect in magnetic materials. *Materials China* **30**, 46, (2011).

140 Liu, M., Lou, J., Li, S. & Sun Nian, X. E-Field Control of Exchange Bias and Deterministic Magnetization Switching in AFM/FM/FE Multiferroic Heterostructures. *Advanced Functional Materials* **21**, 2593-2598, (2011).

141 Lim, L. C., Rajan, K. K. & Jin, J. Characterization of flux-grown PZN-PT single crystals for high-performance piezo devices. *IEEE Transactions on Ultrasonics, Ferroelectrics, and Frequency Control* **54**, 2474-2478, (2007).

142 Lou, J. *et al.* Soft magnetism, magnetostriction, and microwave properties of FeGaB thin films. *Applied Physics Letters* **91**, 182504, (2007).

143 Xue, X. *et al. Electric field induced reversible 180° magnetization switching through tuning of interfacial exchange bias along magnetic easy-axis in multiferroic laminates*. Vol. 5 (2015).

144 Suryanarayana, C. Mechanical alloying and milling. *Progress in Materials Science* **46**, 1-184, (2001).

145 Kang, S. J. L. *Sintering: Densification, Grain Growth and Microstructure*. (Elsevier Science, 2004).

146 Hiroya, T., Akiyasu, Y., Jun-ichi, S., Hiraku, O. & Kohji, K. Strongly connected ex situ MgB_2 polycrystalline bulks fabricated by solid-state self-sintering. *Superconductor Science and Technology* **25**, 115022, (2012).

147 Guillon, O. *et al.* Field-Assisted Sintering Technology/Spark Plasma Sintering: Mechanisms, Materials, and Technology Developments. *Advanced Engineering Materials* **16**, 830-849, (2014).

148 Raj, R., Cologna, M. & Francis, J. S. C. Influence of Externally Imposed and Internally Generated Electrical Fields on Grain Growth, Diffusional Creep, Sintering and Related Phenomena in Ceramics. *Journal of the American Ceramic Society* **94**, 1941-1965, (2011).

149 Antolovich, S. D. & Conrad, H. The Effects of Electric Currents and Fields on Deformation in Metals, Ceramics, and Ionic Materials: An Interpretive Survey. *Materials and Manufacturing Processes* **19**, 587-610, (2004).

150 Guyot, P. *et al.* Does the Branly effect occur in spark plasma sintering? *Journal of Physics D: Applied Physics* **45**, 092001, (2012).

151 Bish, D. L. & Post, J. E. *Modern powder diffraction*, 1989.

152 Chatterjee, A. K. in *Handbook of Analytical Techniques in Concrete Science and Technology* (eds V. S. Ramachandran & James J. Beaudoin) 275-332 (William Andrew Publishing, 2001).

153 Jaklevic, R. C., Lambe, J., Silver, A. H. & Mercereau, J. E. Quantum Interference Effects in Josephson Tunneling. *Physical Review Letters* **12**, 159-160, (1964).

154 Damjanovic, D. Materials for high temperature piezoelectric transducers. *Current Opinion in Solid State and Materials Science* **3**, 469-473, (1998).

155 Turner, R. C., Fuierer, P. A., Newnham, R. E. & Shrout, T. R. Materials for high temperature acoustic and vibration sensors: A review. *Applied Acoustics* **41**, 299-324, (1994).

156 Park, B. H. *et al.* Lanthanum-substituted bismuth titanate for use in non-volatile memories. *Nature* **401**, 682, (1999).

157 Boivin, J. C. & Mairesse, G. Recent material developments in fast oxide ion conductors. *Chemistry of Materials* **10**, 2870-2888, (1998).

158 Kubacka, A., Fernández-García, M. & Colón, G. Advanced nanoarchitectures for solar photocatalytic applications. *Chemical Reviews* **112**, 1555-1614, (2012).

159 Bai, W. *et al.* Dielectric behaviors of Aurivillius $Bi_5Ti_3Fe_{0.5}Cr_{0.5}O_{15}$ multiferroic polycrystals: Determining the intrinsic magnetoelectric responses by impedance spectroscopy. *Scientific Reports* **5**, 17846, (2015).

160 Park, S.-E. E. & Hackenberger, W. High performance single crystal piezoelectrics: applications and issues. *Current Opinion in Solid State and Materials Science* **6**, 11-18, (2002).

161 Yan, H. *et al.* Orientation dependence of dielectric and relaxor behaviour in Aurivillius phase $BaBi_2Nb_2O_9$ ceramics prepared by spark plasma sintering. *Journal of Materials Science: Materials in Electronics* **17**, 657-661, (2006).

162 Khokhar, A., Goyal, P. K., Thakur, O. P., Shukla, A. K. & Sreenivas, K. Influence of lanthanum distribution on dielectric and ferroelectric properties of $BaBi_{4-x}La_xTi_4O_{15}$ ceramics. *Materials Chemistry and Physics* **152**, 13-25, (2015).

163 Shimakawa, Y. *et al.* Crystal structure and ferroelectric properties of $ABi_2Ta_2O_9$(A=Ca, Sr, and Ba). *Physical Review B* **61**, 6559-6564, (2000).

164 Tellier, J., Boullay, P., Manier, M. & Mercurio, D. A comparative study of the Aurivillius phase ferroelectrics $CaBi_4Ti_4O_{15}$ and $BaBi_4Ti_4O_{15}$. *Journal of Solid State Chemistry* **177**, 1829-1837, (2004).

165 Aurivillius, B. & Fang, H. *Ferroelectricity in the compound* $Ba_2Bi_4Ti_5O_{18}$. Vol. 126 (1962).

166 Subbarao E, C. Crystal chemistry of mixed bismuth oxides with layer-type structure. *Journal of the American Ceramic Society* **45**, 166-169, (2006).

167 Ismunandar *et al.* Structural studies of five layer Aurivillius oxides: $A_2Bi_4Ti_5O_{18}$ (A=Ca, Sr, Ba and Pb). *Journal of Solid State Chemistry* **177**, 4188-4196, (2004).

168 Lightfoot, P., Snedden, A., Blake, S. M. & Knight, K. S. Contrasting structural behavior in the Aurivillius phase ferroelectrics $Bi_4Ti_3O_{12}$, $BaBi_4Ti_4O_{15}$ and $Ba_2Bi_4Ti_5O_{18}$. *MRS Proceedings* **755**, DD4.7, (2011).

169 Fuentes, L. *et al.* Synchrotron radiation study of structural tendencies in Aurivillius Ceramics. *Ferroelectrics* **339**, 209-218, (2006).

170 Hou, R. Z. & Chen, X. M. Synthesis and dielectric properties of layer-structured compounds $A_{n-3}Bi_4Ti_nO_{3n+3}$ (A = Ba, Sr, Ca) with n>4. *Journal of Materials Research* **20**, 2354-2359, (2011).

171 Dubey, S. & Kurchania, R. Study of dielectric and ferroelectric properties of five-layer Aurivillius oxides: $A_2Bi_4Ti_5O_{18}$ (A = Ba, Pb and Sr) synthesized by solution combustion route. *Bulletin of Materials Science* **38**, 1881-1889, (2015).

172 Kimura, T. Microstructure development and texture formation in lead-free piezoelectric ceramics prepared by templated grain growth process. *Journal of the Ceramic Society of Japan* **124**, 268-282, (2016).

173 Yan, H. X., Ning, H. P., Zhang, H. T. & Reece, M. J. Textured high Curie point piezoelectric ceramics prepared by spark plasma sintering. *Advances in Applied Ceramics* **109**, 139-142, (2010).

174 Kimura, T. & Yoshida, Y. Microstructure development in textured $BaBi_4Ti_4O_{15}$ made by templated grain growth method. *Journal of Electroceramics* **21**, 110-115, (2008).

175 Karthik, C. & Varma, K. B. R. Dielectric and pyroelectric anisotropy in the melt-quenched barium bismuth niobate ceramics. *Journal of Electroceramics* **18**, 347-353, (2007).

176 Duran-Martin, P., Castro, A., Ramos, P., Millan, P. & Jimenez, B. Ferroelectric anisotropy in layered compound type of $Bi_{1.75}Te_{0.25}Sr_{0.75}Na_{0.25}Nb_2O_9$. *Boletín de la Sociedad Española de Cerámica y Vidrio (1983)* **37**, 143-147, (1998).

177 Dreele, A. C. L. a. R. B. V. General structure analysis system (GSAS). *Los Alamos National Laboratory Report LAUR 86-748*, (2004).

178 Aurivillius, B. F., P.H. Ferroelectricity in the compound $Ba_2Bi_4Ti_5O_{18}$. *Physical Review* **126**, p893-p896, (1962).

179 Tadashi, T. & Koichiro, S. Grain orientation and electrical properties of hot-forged $Bi_4Ti_3O_{12}$ ceramics. *Japanese Journal of Applied Physics* **19**, 31, (1980).

180 Mai Pham, T., Henri, H., Olivier, D. & Hichem, D. Orientation distribution and fiber texture of highly oriented piezoceramics: (1-x)$PbMg_{1/3}Nb_{2/3}O_3$ –x$PbTiO_3$ system. *Japanese Journal of Applied Physics* **43**, 8190, (2004).

181 Irie, H., Miyayama, M. & Kudo, T. Electrical Properties of a Bismuth Layer-Structured $Ba_2Bi_4Ti_5O_{18}$ Single Crystal. *Journal of the American Ceramic Society* **83**, 2699-2704, (2004).

182 Kamiyama, T., Hoshikawa, A., Zhou, Q. & J. Kennedy, B. *Structural Studies of Five Layer Aurivillius Oxides: $A_2Bi_4Ti_5O_{18}$ (A =Ca, Sr, Ba and Pb)*. Vol. 13 (2005).

183 Shimakawa, Y. *et al.* Crystal structures and ferroelectric properties of $SrBi_2Ta_2O_9$ and $Sr_{0.8}Bi_{2.2}Ta_2O_9$. *Applied Physics Letters* **74**, 1904-1906, (1999).

184 Uchino, K. & Nomura, S. Critical exponents of the dielectric constants in diffused-phase-transition crystals. *Ferroelectrics* **44**, 55-61, (1982).

185 Maiti, T., Guo, R. & Bhalla, A. S. Structure-property phase diagram of $BaZr_xTi_{1-x}O_3$ system. *Journal of the American Ceramic Society* **91**, 1769-1780, (2008).

186 Jin, L., Li, F., Zhang, S. & Green, D. J. Decoding the fingerprint of ferroelectric loops: comprehension of the material properties and structures. *Journal of the American Ceramic Society* **97**, 1-27, (2013).

187 Yan, H. *et al.* The contribution of electrical conductivity, dielectric permittivity and domain switching in ferroelectric hysteresis loops. *Journal of Advanced Dielectrics* **01**, 107-118, (2011).

188 Karthik, T., Radhakrishanan, D., Narayana, C. & Asthana, S. Nature of electric field driven ferroelectric phase transition in lead-free $Na_{1/2}Bi_{1/2}TiO_3$: In-situ temperature dependent ferroelectric hysteresis and Raman scattering studies. *Journal of Alloys and Compounds* **732**, 945-951, (2018).

189 Dinh, T. H. *et al.* Nanoscale ferroelectric/relaxor composites: Origin of large strain in lead–free Bi–based incipient piezoelectric ceramics. *Journal of the European Ceramic Society* **36**, 3401-3407, (2016).

190 Liu, L. *et al.* Large strain response based on relaxor-antiferroelectric coherence in $Bi_{0.5}Na_{0.5}TiO_3$–$SrTiO_3$–$(K_{0.5}Na_{0.5})NbO_3$ solid solutions. *Journal of Applied Physics* **116**, 184104, (2014).

191 Samara, G. A. in *Solid State Physics* Vol. 56 (eds Henry Ehrenreich & Frans Spaepen) 239-458 (Academic Press, 2001).

192 Bousquet, M. *et al.* Electrical properties of (110) epitaxial lead-free ferroelectric $Na_{0.5}Bi_{0.5}TiO_3$ thin films grown by pulsed laser deposition: Macroscopic and nanoscale data. *Journal of Applied Physics* **111**, 104106, (2012).

193 Jones, G. O. & Thomas, P. A. Investigation of the structure and phase transitions in the novel A-site substituted distorted perovskite compound $Na_{0.5}Bi_{0.5}TiO_3$. *Acta Crystallographica Section B* **58**, 168-178, (2002).

194 Smolensky GA, I. V., Agranovskaya AI, Krainik NN. New ferroelectrics of complex composition. . *Sov Phys Solid State.* **2(11)**, 2651–2654, (1961).

195 Jones, G. O. & Thomas, P. A. The tetragonal phase of $Na_{0.5}Bi_{0.5}TiO_3$ - a new variant of the perovskite structure. *Acta Crystallographica Section B* **56**, 426-430, (2000).

196 Suchanicz, J. Behaviour of $Na_{0.5}Bi_{0.5}TiO_3$ ceramics in the a.c. electric field. *Ferroelectrics* **209**, 561-568, (1998).

197 Nesbet, R. K. Heisenberg Exchange Interaction of Two Mn Atoms. *Physical Review* **135**, A460-A465, (1964).

198 Thomas Pamela, A. *et al.* in *Zeitschrift für Kristallographie - Crystalline Materials* Vol. 220 717 (2005).

199 Pattanayak, R., Kuila, S., Routray, K., Raut, S. & Panigrahi, S. *Magnetic and Magnetoimpedance Study of* $BaFe_{12}O_{19}$-$Na_{0.5}Bi_{0.5}TiO_3$ *Novel Magnetoelectric Composite Systems*. Vol. PP (2018).

200 Li, M., Li, L., Zang, J. & Sinclair, D. C. Donor-doping and reduced leakage current in Nb-doped $Na_{0.5}Bi_{0.5}TiO_3$. *Applied Physics Letters* **106**, 102904, (2015).

201 Furdyna, J. K. Diluted magnetic semiconductors. *Journal of Applied Physics* **64**, R29-R64, (1988).

202 Fukumura, T. *et al.* Magnetic properties of Mn-doped ZnO. *Applied Physics Letters* **78**, 958-960, (2001).

203 Yaakov, K. Curie point of ferromagnets. *European Journal of Physics* **18**, 448, (1997).

204 Zhao, B. C., Ma, Y. Q., Song, W. H. & Sun, Y. P. Magnetization steps in the phase separated manganite $La_{0.275}Pr_{0.35}Ca_{0.375}MnO_3$. *Physics Letters A* **354**, 472-476, (2006).

205 Sharma, V. K. & Varma, G. D. Strain induced ferromagnetism in Sb co-doped ZnMnO samples. *Journal of Physics: Condensed Matter* **21**, 296001, (2009).

206 Maxwell, J. C. VIII. A dynamical theory of the electromagnetic field. *Philosophical Transactions of the Royal Society of London* **155**, 459-512, (1865).

207 Fernández-Posada, C. M. *et al.* A novel perovskite oxide chemically designed to show multiferroic phase boundary with room-temperature magnetoelectricity. *Nature Communications* **7**, 12772, (2016).

208 Hur, N. *et al.* Electric polarization reversal and memory in a multiferroic material induced by magnetic fields. *Nature* **429**, 392, (2004).

209 Shah, J. & K. Kotnala, R. *Induced magnetism and magnetoelectric coupling in ferroelectric* $BaTiO_3$ *by Cr-doping synthesized by a facile chemical route*. Vol. 1 (2013).

210 Morgan, T. Low energy consumption spintronics using multiferroic heterostructures. *Journal of Physics: Condensed Matter* **28**, 033001, (2016).

211 Cheong, S.-W. & Mostovoy, M. Multiferroics: a magnetic twist for ferroelectricity. *Nature Materials* **6**, 13, (2007).

212 Takenaka, T., Maruyama, K. & Sakata, K. $(Bi_{0.5}Na_{0.5})TiO_3$ -$BaTiO_3$ System for Lead-Free Piezoelectric Ceramics. *Japanese Journal of Applied Physics* **30**, 2236-2239, (1991).

213 Zuo, R., Ye, C., Fang, X. & Li, J. Tantalum doped $0.94Bi_{0.5}Na_{0.5}TiO_3$–$0.06BaTiO_3$ piezoelectric ceramics. *Journal of the European Ceramic Society* **28**, 871-877, (2008).

214 Dai, Y.-J., Zhang, S., Shrout, T. R. & Zhang, X.-W. Piezoelectric and Ferroelectric Properties of Li-Doped $(Bi_{0.5}Na_{0.5})TiO_3$–$(Bi_{0.5}K_{0.5})TiO_3$–$BaTiO_3$ Lead-Free Piezoelectric Ceramics. *Journal of the American Ceramic Society* **93**, 1108-1113, (2010).

215 Cernea, M., Andronescu, E., Radu, R., Fochi, F. & Galassi, C. Sol–gel synthesis and characterization of $BaTiO_3$-doped $(Bi_{0.5}Na_{0.5})TiO_3$ piezoelectric ceramics. *Journal of Alloys and Compounds* **490**, 690-694, (2010).

216 Mahajan, A. *et al.* Effect of Phase Transitions on Thermal Depoling in Lead-Free $0.94(Bi_{0.5}Na_{0.5}TiO_3)$–$0.06(BaTiO_3)$ Based Piezoelectrics. *The Journal of Physical Chemistry C* **121**, 5709-5718, (2017).

217 Kwi Young, Y., Dan, R., Takeshi, K., Minoru, N. & Masanori, O. Giant Ferroelectric Polarization Beyond 150 $\mu C/cm^2$ in $BiFeO_3$ Thin Film. *Japanese Journal of Applied Physics* **43**, L647, (2004).

218 Sushil, K. S. & Hiroshi, I. Reduced Leakage Current in $BiFeO_3$ Thin Films on Si Substrates Formed by a Chemical Solution Method. *Japanese Journal of Applied Physics* **44**, L734, (2005).

219 Je-Geun, P., Manh Duc, L., Jaehong, J. & Sanghyun, L. Structure and spin dynamics of multiferroic BiFeO 3. *Journal of Physics: Condensed Matter* **26**, 433202, (2014).

220 Lebeugle, D. *et al.* Electric-Field-Induced Spin Flop in ${\mathrm{BiFeO}}_{3}$ Single Crystals at Room Temperature. *Physical Review Letters* **100**, 227602, (2008).

221 Yu, Z., Krstic, V. D. & Mukherjee, B. K. Microstructure and properties of lead-free $(Bi_{1/2}Na_{1/2})TiO_3$ based piezoelectric ceramics doped with different cations. *Journal of Materials Science* **42**, 3544-3551, (2007).

222 Toby, B. *R Factors in Rietveld Analysis: How Good is Good Enough*. Vol. 21 (2006).

223 Jia, W., Hou, Y., Zheng, M. & Zhu, M. High-temperature dielectrics based on (1-x)(0.94Bi0.5Na0.5TiO3-0.06BaTiO3)-xNaNbO3 system. *Journal of Alloys and Compounds* **724**, 306-315, (2017).

224 Michel, C., Moreau, J.-M., Achenbach, G. D., Gerson, R. & James, W. J. The atomic structure of BiFeO3. *Solid State Communications* **7**, 701-704, (1969).

225 Xu, Q. *et al.* Enhanced energy storage properties of NaNbO3 modified Bi0.5Na0.5TiO3 based ceramics. *Journal of the European Ceramic Society* **35**, 545-553, (2015).

226 Sung, Y. S. *et al.* Effects of Na nonstoichiometry in (Bi0.5Na0.5+x)TiO3 ceramics. *Applied Physics Letters* **96**, 022901, (2010).

227 Wei, L., Li, Z. & Zhang, W. F. Influence of Co doping content on its valence state in $Zn_{1-x}Co_xO$ $(0\leq x\leq 0.15)$ thin films. *Applied Surface Science* **255**, 4992-4995, (2009).

228 Bi, L. *et al.* Structural, magnetic, and optical properties of $BiFeO_3$ and Bi_2FeMnO_6 epitaxial thin films: An experimental and first-principles study. *Physical Review B* **78**, 104106, (2008).

229 Chauhan, S. *et al.* Multiferroic, magnetoelectric and optical properties of Mn doped $BiFeO_3$ nanoparticles. *Solid State Communications* **152**, 525-529, (2012).

230 Pezhumkattil Palakkal, J., Lekshmi, N., Thomas, S., Suresh, K. & Raama Varma, M. *Observation of high-temperature magnetic transition and existence of ferromagnetic short-range correlations above transition in double perovskite La_2FeMnO_6*. Vol. 5 (2015).

231 Kawamura, H. & Taniguchi, T. in *Handbook of Magnetic Materials* Vol. 24 (ed K. H. J. Buschow) 1-137 (Elsevier, 2015).

232 Ji, H. *et al.* Structure and Electrical Properties of $Na_{0.5}Bi_{0.5}TiO_3$ Ferroelectric Thick Films Derived From a Polymer Modified Sol-Gel Method. *IEEE transactions on ultrasonics, ferroelectrics, and frequency control* **58**, 2042-2049, (2011).

233 de Oliveira, L. A. S., Pentón-Madrigal, A., Guimarães, A. P. & Sinnecker, J. P. Thermally activated processes and superparamagnetism in $Bi_{12}MnO_{20}$ nanoparticles: A comparative study. *Journal of Magnetism and Magnetic Materials* **401**, 890-896, (2016).

234 de Oliveira, L. A. S., Sinnecker, J. P., Vieira, M. D. & Pentón-Madrigal, A. Low temperature synthesis, structural, and magnetic characterization of manganese sillenite $Bi_{12}MnO_{20}$. *Journal of Applied Physics* **107**, 09D907, (2010).

235 Delicat, U. *et al.* Tetrahedral Coordination of Mn(IV) by Oxygen in Manganese Sillenite $Bi_{12}MnO_{20}$. *Journal of Solid State Chemistry* **110**, 66-69, (1994).